Higgs “Photo-Production” and Related Experimental Issues in the Forward Direction of the ATLAS Detector

by

Nooshin Dehghanian

A thesis submitted in partial fulfillment of the requirements for the degree of

Doctor of Philosophy

Department of Physics
University of Alberta

Abstract

This thesis is devoted to the study of aspects of the forward physics and forward detector system of the ATLAS detector. The first topic involves LUCID, the official luminosity monitor of ATLAS during Run-2. Here we concentrate on the simulation, calibration system and performance of the LUCID-2 detector. The second topic covers the ATLAS Forward Proton (AFP) detector. In this case, the testing and performance studies of the readout electronics for the precision AFP ToF detector - required to reduce pile-up background - are the key issues. The main topic is devoted to the study of Higgs production in Central Exclusive Diffractive (CED) processes with the ATLAS detector at the LHC. A detailed calculation of diffractive ultra-peripheral CED "photoproduction" of the Higgs boson, in proton-proton and heavy-ion - proton interactions at the LHC, is presented for the first time. CED Higgs production via Double Pomeron Exchange is also studied using the same calculation techniques and compared with other well reported results in this area. This was done as a test of the techniques used and in order to assess the error on the cross-section for Higgs "photoproduction" reported here.

Dedicated to my lovely parents and my dear brother

Acknowledgements

Firstly, I would like to express my sincere gratitude to my advisor Prof. James Pinfold for the continuous support of my Ph.D. study and related research, for his patience, motivation, and immense knowledge. His guidance helped me in all the time of research and writing of this thesis. Besides my advisor, I would like to thank the rest of my thesis committee especially Prof. Axsel Hallin and Prof. Marc de Montigny for their insightful comments and encouragement. My sincere thanks also go to the LUCID team in ATLAS especially Prof. Vincent Hedberg, Prof. Benedetto Giacobbe, and Dr. Antonio Sbrizzi.

I also would like to thank Paul Davis for his support and guidance in the electronics lab.

Last but not least, I would like to thank my family: my parents and my brother for supporting me spiritually throughout writing this thesis and my life in general.

Table of Contents

List of Tables

List of Figures

Acronyms

AFP	ATLAS Forward Proton tagging detector
ALFA	Absolute Luminosity For ATLAS
ALICE	A large ion collider experiment
ATLAS	A toroidal LHC apparatus
BCISs	Bunch Crossing IDs
BCM	The Beam Condition Monitor
CFD	Constant Fraction Discriminator
CED	Central Exclusive Diffractive
CEDP	Central Exclusive Diffractive "Photo-production"
CEP	Central Exclusive Higgs Production
CMS	Compact Muon Solenoid
CS	Central Solenoid
CSCs	Cathode Strip Chambers

CTP	Central Trigger Processor
DAQ	Trigger and Data Acquisition
DD	Double Diffraction
DGLAP	Dokshitzer-Gribov-Lipatov-Altarelli-Parisi
DIS	Deep Inelastic Scattering
DLL	Delay Locked Loop
DVCS	Deeply Virtual Compton Scattering
EF	Event Filter
EM Calorimeters	Electromagnetic Calorimeters
EW	ElectroWeak (model)
FPGA	Field Programmable Gate Arrays
GEANT	GEometry ANd Tracking
GPDs	Generalized Parton Distribution Functions
GUI	Graphical User Interface
HAD	Hadronic
HEC	Hadronic End-cap Calorimeter
HLT	Higher Level Trigger
HPTDC	High precision Time to Digital Convertor

HSIO	High Speed Input-Output
IBL	Insertable B-layer
ID	Inner Detector
INL	Integral Nonlinearity
L1	Level-1
L1A	Level-1 Acceptance
L1Calo	The dedicated trigger hardware in the calorimeter
LAr	Liquid Argon
LB	Luminosity Block
LEIR	Low Energy Ion Ring
LHC	Large Hadron Collider
LHCb	LHC beauty experiment
LHCf	LHC forward experiment
LINAC	Linear Accelerator
LO	Leading Order
LSB	Least Significant Bit
LTB	Local Trigger Board
LUCID	Luminosity measurements Using Cherenkov Integrating Detector

LUCROD	LUCID Read-out Board
MCP-PMTs	Micro-Channel-Plate Photomultipliers
MDTs	Monitored Drift Tubes
MoEDAL	Monopole and Exotics Detectors at the LHC
MS	Muon Spectrometer
MT	Toroidal Magnetic system
NNLO	Next-to-Next-to-Leading Order
NLO	Next-to-Leading Order
PDF	Parton Distribution Function
PLL	Phase Locked Loop
PSB	Proton Synchrotron Booster
PS	Proton Synchrotron
QCD	Quantum Chromodynamics
QED	Quantum Electrodynamics
QFT	Quantum Field Theory
RC	Resistor Capacitor
RCE	Reconfigurable Cluster Element
RDOs	Raw Data Objects

RGSP	Rapidity Gap Survival Probability
ROI	Region of Interest
RP	Roman Pot
RPCs	Resistive Plate Chambers
SCT	Semi-Conductor Tracking detector
SD	Single Diffraction
SiPMT	Silicon Photomultipliers
SM	The Standard Model
SPS	Super Proton Synchrotron
TDC	Time to Digitize Converter
TGCs	Thin Gap Chambers
ToF	Time of Flight
TOTEM	Total elastic and diffractive cross-section measurement
TRACK	Inner detector track counting
TRT	Transition Radiation Tracker
TTC	Timing, Trigger, and Control
TTS	Transit Time Spread
UP	Ultra-Peripheral

UV	Ultraviolet
VdM	Van der Meer
ZDCs	Zero Degree Calorimeters

Chapter 1

The ATLAS experiment at the LHC

1.1 The Large Hadron Collider (LHC)

The Large Hadron Collider(LHC) at CERN operates at unprecedented energy. The collision of proton beams at a centre of mass energy of up to 14 TeV with luminosity of 10^{34} cm^{-2} s^{-1}, allows the detailed exploration of the uncharted territory at the TeV scale. The LHC is also capable of accelerating heavy ions to exploit lead-lead and proton-lead collisions at the centre of mass energy of 8.8 and 5.5 TeV, with the luminosity of the order of 10^{29} cm^{-2} s^{-1} and 10^{27} cm^{-2} s^{-1} respectively.[1]

The discovery of what was ostensibly the Standard Model Higgs boson was announced in 2012 [50], providing the last piece of the Standard Model.

[1]In Run-2, LHC reached the centre of mass energy of 8.16 TeV for p-lead collision with an instantaneous luminosity between 0.5 to 1×10^{29} cm^{-2}s^{-1}.and the centre of mass energy of 5.02 TeV for lead-lead collision with an instantaneous luminosity of 2.7×10^{27} cm^{-2}s^{-1} [3, 6].

However, precision measurement of SM parameters like the mass of Higgs boson will still continue to be a primary purpose of the LHC.

The protons in the beam originate from a bottle of hydrogen gas. The electrons are stripped from the hydrogen atoms and then injected to the linear accelerator in the chain, LINAC 2, which accelerates the protons to the energy of 50 MeV. The beam is then injected into the Proton Synchrotron Booster (PSB), which accelerates protons to 1.4 GeV, followed by the Proton Synchrotron (PS), which increases the beam energy up to 25 GeV. Protons are then sent to the Super Proton Synchrotron (SPS) where they are accelerated to 450 GeV, before finally reaching the LHC ring, as shown in figure 1.1. The LHC is installed in circular tunnel with 27 km circumference in a depth of about 100 m underground. Two counter rotating beams of protons, in the blue and red loops of the LHC shown in figure 1.2, to maximum beam energy. The two beam collide at the centre of mass energy of 14 TeV at four interaction points located around the circumference of the LHC.

For heavy ion collisions, the lead sample is first heated to about 500^0 C to vaporize a number of atoms. Initially a few electrons are stripped from the atoms and the newly created ions are accelerated in LINAC3 to 4.5 MeV, where the remaining electrons are stripped from the ions. Next, the ions are accumulated and accelerated to 72 MeV per nucleon in the Low Energy Ion Ring (LEIR), the heavy-ions are then accelerated to full energy in a similar way to protons.

There are maximum of 3564 bunches, each containing $\sim 10^{11}$ protons, in both proton beams. Each bunch crossing is labelled with a Bunch Crossing ID number (BCID). Two neighbour BCIDs are separated in time by 25 ns.

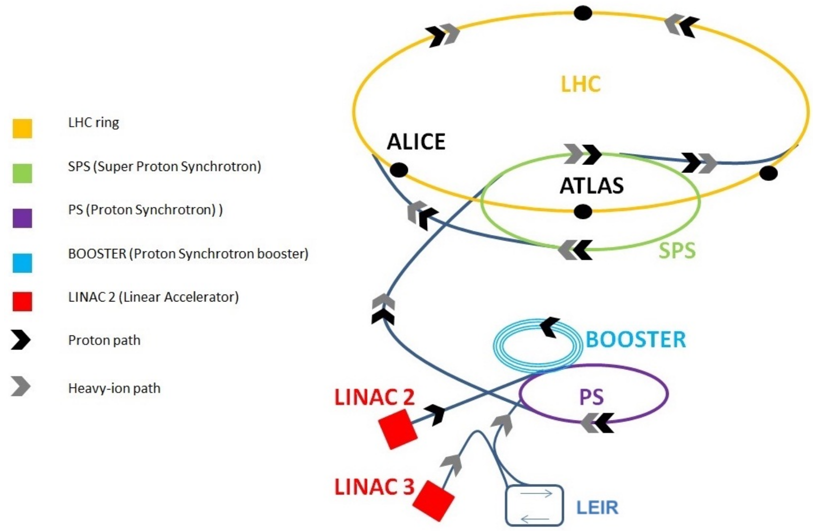

Figure 1.1: The schematic view of the LHC injection chain.

A typical beam structure alternates between regions with many filled BCIDs (called bunch trains) and regions with many empty BCIDs. Most physics runs in 2015 used 25 ns bunch spacing within a train that had up to 2808 filled bunches.

The counter rotating beams collide at one of the four interaction points located around the circumference of the LHC, corresponding to the positions of four particle detectors: ATLAS, CMS, ALICE and LHCb, shown in figure 1.2.

The four main LHC experiments are:

- **ATLAS**(A toroidal LHC apparatus) is a general purpose detector for studying proton-proton and heavy ion collisions [7].

- **CMS** (Compact muon solenoid) is a general purpose detector for studying proton-proton and heavy ion collisions with the same physics program as ATLAS detector [8].

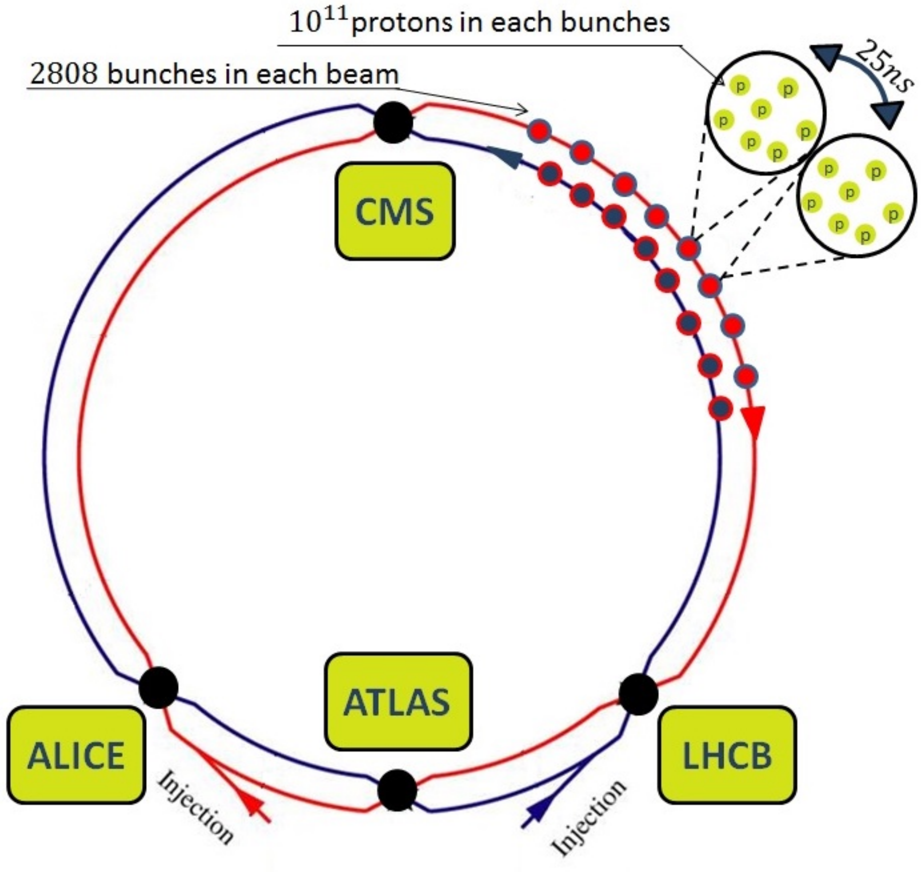

Figure 1.2: A schematic layout of the LHC ring.

- **ALICE** (A large ion collider experiment) is dedicated to heavy ion physics and the study of the physics of strongly interacting matter and the quark-gluon plasma [9].

- **LHCb** (LHC beauty experiment) is dedicated to precision measurements of CP violation and rare decays of B hadrons [10].

  There are also the following three smaller LHC experiments.

- **LHCf** (LHC forward experiment) is dedicated to the measurement of neutral particles emitted in the very forward region of the LHC collisions, in order to calibrate and interpret cosmic ray experiments [11].

- **MoEDAL** (Monopole and exotics detectors at the LHC) The prime motivation of MoEDAL is to search directly for anomalously ionizing avatars of new physics such as the magnetic monopole [12].

- **TOTEM** (Total elastic and diffractive cross-section measurement) is designed to measure the total proton-proton cross-section with the luminosity independent method and study the elastic and diffractive scattering at the LHC [13].

1.2 LHC performance during Run 1 and 2 and long term plan

Run number		Run 1			Run 2			Run 3
Parameter	Design	2010	2011	2012	2015	2016	2017	2020-22
Beam energy [TeV]	7.0	3.5	3.5	4	6.5	6.5	6.5	7
Protons per bunch [$\times 10^{11}$]	1.15	1.0	1.3	1.5	1.1	1.1	-	-
Bunches per beam	2808	368	1380	1380	2244	2076	-	-
Bunch spacing [ns]	25	150	75/50	50	50/25	25	25	-
Delivered integrated luminosity [fb^{-1}]	-	0.045	5.1	21.3	3.9	36.0	50.4	300
Peak instantaneous Luminosity [$\times 10^{34} cm^{-2} s^{-1}$]	1	0.021	0.36	0.77	0.51	1.37	2.06	2
Mean number of interactions per bunch crossing	-	4.0	9.1	20.7	13.7	24.2	-	-

Table 1.1: The LHC parameters during Run 1, Run 2, Run 3, and their nominal values for proton-proton collisions [4, 5, 6]

From the beginning of Run 1 in 2010, the beam parameters slowly evolved until the end of 2012. The beam energy in 2010 and 2011 was 3.5 TeV, while in 2012 it increased to 4 TeV. From the beginning of Run 1 until the long shutdown in 2012, the number of bunches per beam increased from 368 to 1318, while the bunch spacing decreased from 150 ns to 50 ns and the peak instantaneous luminosity reached 77% nominal from just 2%. The total amount of luminosity that was gathered during Run 1 in 2010, 2011, and 2012 at the LHC is $0.045 fb^{-1}$, $5.1 fb^{-1}$, and $21.3 fb^{-1}$, respectively.

After the two year long shutdown, Run 2 started in June 2015 with the beam energy of 6.5 TeV. At the beginning of Run 2 the bunch spacing was 50 ns which subsequently decreased to 25 ns later in the year. Much more data was collected in Run 2 than Run 1. For example, the data recorded in 2016 and 2017 was 36.0 fb^{-1} and 50.4 fb^{-1}, respectively. Run 2 will end in 2018. After Run 2 there will be a 2 year shutdown at which time the machine will be upgraded to run at a beam energy of 7 TeV, the original design luminosity.

Run 3 is expected to start in 2020 and continue until 2022 and collect approximately 300 fb^{-1} of data by the end of the run. In 2025, High-Luminosity Large Hadron Collider (HL-LHC) project will be implemented. The objective is to increase luminosity by a factor of 10 beyond the LHC design value. With this increased luminosity it is feasible to study rare processes which are below the sensitivity of the LHC experiments operating at the nominal design luminosity. More details on LHC run parameters are shown in table 1.1.

1.3 The ATLAS Experiment

The complete ATLAS detector is split into a barrel part, where detector layers are positioned on cylindrical surfaces around the beam axis, and two end-cap

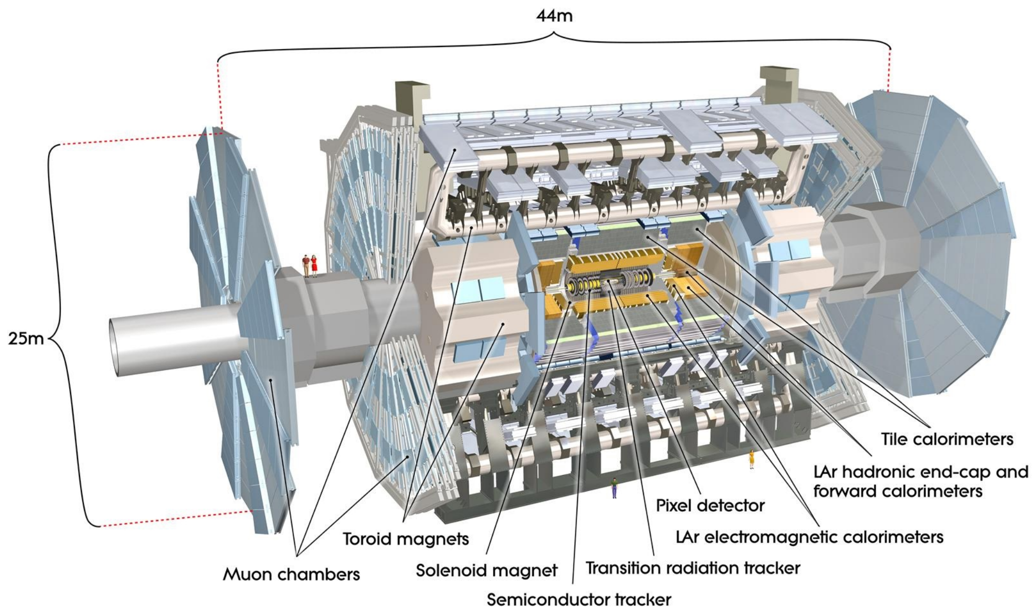

Figure 1.3: Overview of the full ATLAS detector showing the magnet systems and the four major sub-detectors.

parts, where detector layers are positioned in planes of constant z perpendicular to the beam-pipe and a backward part, extending up to a pseudo-rapidity of $\eta = 4.9$. In the barrel region the ATLAS detector is deployed in four layers. The first layer of the ATLAS detector is the inner detector (ID) which track charged particles. The inner detector is immersed in a 2 T solenoidal magnetic field enabling the momentum of the tracked particles to be determined. The next two layers contain the calorimetry the function of which is to determine the electromagnetic (second layer) and hadronic energy (third layer) energy of each event. The fourth and outer layer is the muon spectrometer (MS) for high-precision tracking of muons in an approximately 4 T toroidal magnetic field. The preceding structure is repeated in the end-cap regions of ATLAS except that in this region the tracking layer is absent.The design performance requirements for the ATLAS detector and coverage of its sub-detectors are summarized in table 1.2.

sub-detector	Resolution	Coverage
Inner Detector	$\frac{\sigma(P_T)}{P_T} = \frac{0.05\%}{\sqrt{P_T}} \oplus 1\%$	$\lvert\eta\rvert < 2.5$
Electromagnetic calorimeter	$\frac{\sigma(E)}{E} = \frac{10\%}{\sqrt{E}} \oplus 0.7\%$	$\lvert\eta\rvert < 3.3$
Hadronic calorimeter (barrel and end-cap)	$\frac{\sigma(E)}{E} = \frac{50\%}{\sqrt{E}} \oplus 0.3\%$	$\lvert\eta\rvert < 3.3$
Forward calorimeters	$\frac{\sigma(E)}{E} = \frac{100\%}{\sqrt{E}} \oplus 10\%$	$3.1 < \lvert\eta\rvert < 4.9$
The Muon Spectrometer	$\frac{\sigma(P_T)}{P_T} = 10\%$ at $P_T = 1$ TeV	$\lvert\eta\rvert < 2.7$

Table 1.2: The performance of the ATLAS detector and the coverage of its sub-detectors [5]

1.4 ATLAS Coordinate System

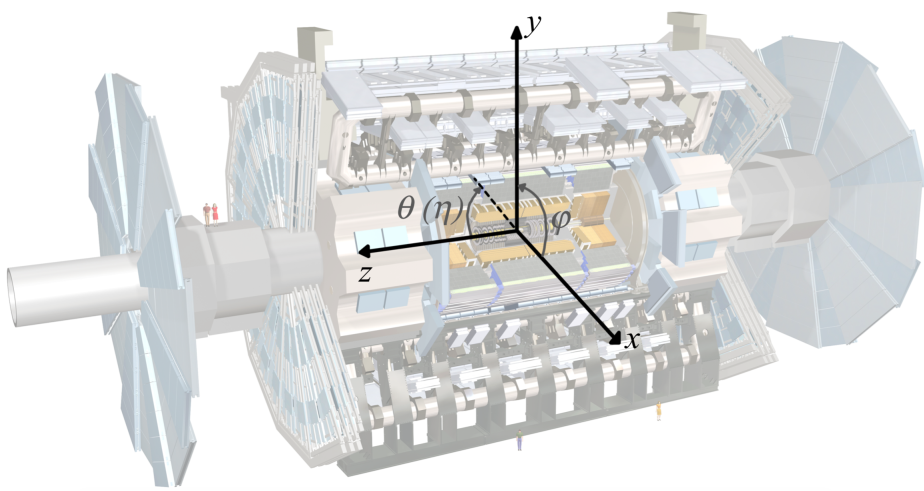

Figure 1.4: ATLAS coordinate system

The coordinate system used in ATLAS is a right-handed Cartesian coordinate system with the nominal interaction point in the centre of the detector defined as its origin, shown in figure 1.4. The x-y plane is transverse to the beam direction, with the positive x-axis pointing to the centre of the LHC ring and the positive y-axis pointing upwards and the z-axis is along the beam line. The half of the detector at positive z-values is referred to as the "A" side, the other half the "C" side.The polar coordinates are defined with: the radial distance r is the distance from the beam line; the azimuthal angle ϕ measured around the beam axis, ranging between $-\pi$ to π with respect to the x axis; and, the polar angle θ is measured from the positive z axis and varies from 0 to π.

Rapidity, y, is a Lorentz invariant parameter and a convenient way to display the p_z dependence of the data, where:

$$y = ln(\frac{E + p_z}{E - p_z}) \tag{1.1}$$

p_z is the component of momentum along the beam axis and E is the energy of the particle.

However, measuring rapidity can be problematic as it can be difficult to get the total momentum vector of a particle especially at high values of the rapidity where the z component of the momentum is large, and not determined precisely. This leads to the concept of pseudo-rapidity η which is defined as:

$$\eta = -ln[tan(\frac{\theta}{2})] \tag{1.2}$$

where θ is the angle made by the particle trajectory with the beam axis. In hadron collider physics, the rapidity (or pseudo-rapidity) is preferred over the polar angle because, loosely speaking, particle production is constant as a function of rapidity.

1.5 The ATLAS Sub-detectors Overview

1.5.1 Magnet System

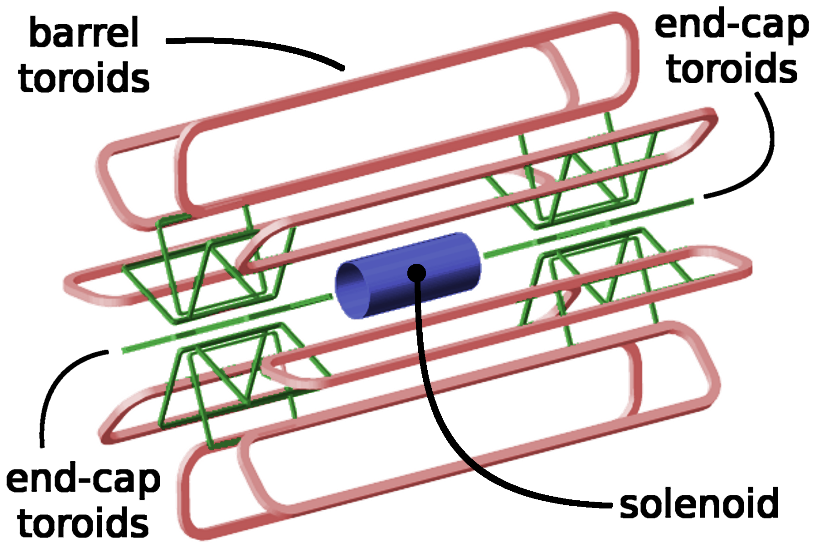

Figure 1.5: Overview of the ATLAS magnet systems.

The ATLAS Magnet System provides a magnetic field to bend tracks of charged particles, allowing the determination of the momentum of the particles from the curvature of the track measured in the tracking detectors. The ability to accurately determine the track momentum using tracking depends on the curvature of the track.

ATLAS has two superconducting magnetic systems. The first system is the Central Solenoid (CS) [14] that produces a uniform 2 T solenoidal magnetic field parallel with the beam axis allowing the accurate determination of the momentum of even very high momentum particles. The CS has a length of 5.8 m, a diameter of 2.56 m and a thickness of a only 5 cm. Keeping the thickness at a minimum was a one of its main design goals. This is because some particles have to pass through the solenoid before reaching the calorimeter.

Secondly, we have the toroidal magnetic system (MT) [15, 16] for the muon spectrometer (MS). The MT system, like the MS, is divided into a barrel region and two end-cap regions. The barrel toroid consists of 8 coils assembled symmetrically around the beam axis. The coils have a length of 25.3 m, an inner diameter of 9.4 m and an outer diameter of 20.1 m. The toroidal magnet system is part of the muon barrel spectrometer. The end-cap toroids also consist of 8 coils each. They are part of the muon end-cap spectrometers, located 10 m away from the interaction point with an outer diameter of 10.7 m.

The MT for the Barrel Toroid region of the MS provides a magnetic field ranging from 0.15 T to 3.5 T. The End-Cap Toroids provide a magnetic field with strength ranging from 0.2 T to 3.5 T in the MS end-cap regions. The overall configuration of the MT system is shown in figure 1.5.

1.5.2 Inner Detectors

The purpose of the Inner Detector (ID) is to: reconstruct the tracks and vertices in the event with high efficiency; contributing, together with the calorimeter and muon systems, to the electron, photon and muon recognition; and, supplying the important extra signature for short-lived particle decay vertices. The ID is located inside the solenoid magnet, and is composed of three layers of sub-detectors: 1) A pixel tracker [19], 2) Semi-Conductor Tracking detector (SCT) [22, 23]; and, 3) a straw tube, Transition Radiation Tracker (TRT) [24, 25, 26]. All the three detectors are designed to track the 3-D trajectories

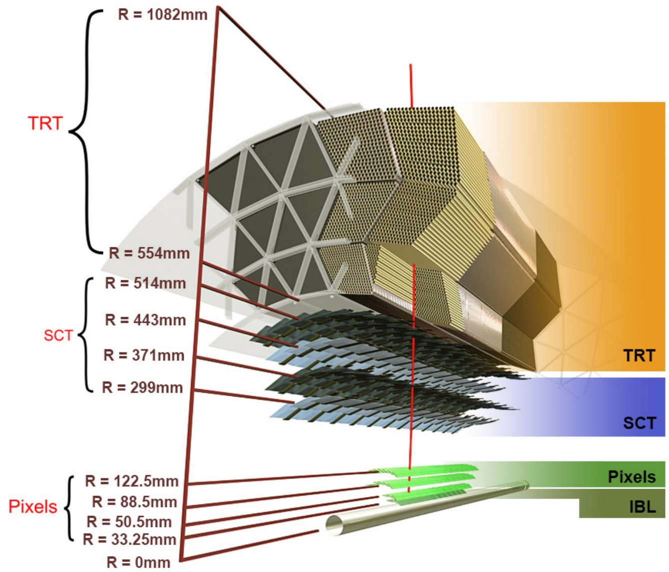

Figure 1.6: Schematic view of the Inner Detector (ID), including the new Insertable B-Layer, the Pixel barrel and end-cap, SCT barrel and end-cap and TRT barrel.

of charged particles with high resolution and minimum multiple scattering. A schematic over view of three detectors is shown in figure 1.6.

In the following sub-section, the details of these three detectors will be discussed.

Pixel Detector

The pixel detector [19] is designed to provide a very high-granularity, high-precision set of measurements as close to the interaction point as possible. The system provides three of the precision measurements over the full acceptance, and determines the impact parameter resolution and the ability of the Inner Detector to find short-lived particles such as b-quarks and τ-leptons

The pixel detector's high granularity is achieved with 1744 pixel modules each with 47232 pixels of size 50×400 μm^2 and thickness 250 microns. The sensors are made of radiation hard p-n type silicon wafers. A charged particle traversing the pixel sensor creates electron-hole pairs which are separated by the electric field and collected at each pixel. The pixel detector has been designed to provide high track resolution of about 12 μm in the transverse plane and 66 μm and 77 μm in the z direction for the barrel and end-cap region, respectively.

The Insertable B-layer (IBL) [20], the fourth-pixel layer, was added inside the existing ATLAS pixel detector during the long LHC shutdown of 2013 and 2014. The new fourth layer pixel system is the closest layer of the detector to the beam line and it plays a crucial role in the reconstruction of secondary vertices for the b-jet tagging where the B meson decays away from the interaction point.

Semi-Conductor Tracker

The second layer of the Inner Detector, the Semi-Conductor Tracker (SCT) [21, 22], occupies the region from 299 mm to 514 mm radially from the interaction point. The SCT consists of silicon strip modules very similar to pixel modules, arranged into 4 barrel layers and two end-caps each of 9 disks.

There are 4088 modules in the SCT, each of these modules has 1536 silicon strips that are 2.6 cm long and with 80 micron pitch. The silicon strips are actually two pairs of silicon micro-strip planes glued together back-to-back. In general, this double layer configuration allows for reduction of the number of readout channels. Compared to the pixel detector, the SCT has coarser granularity. The spatial resolution of the SCT detector modules is 17 μm in the transverse direction and 580 μm in the longitudinal direction.

Transition Radiation Tracker

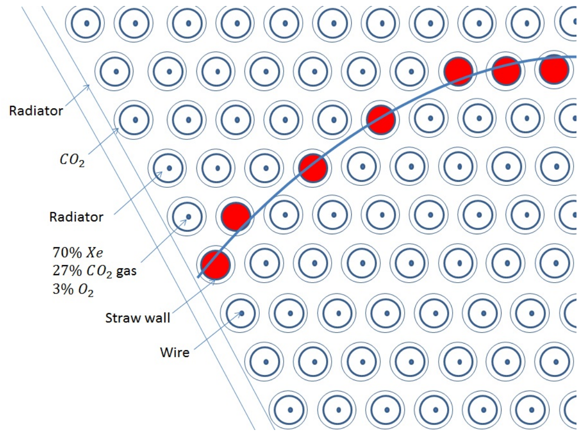

Figure 1.7: Schematic diagram of portion of the TRT detector with an indication of a track of charged particle which is slightly curved due to the magnetic field of solenoid.

The outmost layer of the inner detector is the Transition Radiation Tracker (TRT) [24, 25, 26] extending in radius from 554 mm to 1028 mm. Along with continuous tracking, the TRT provides electron identification capability through the detection of transition radiation X-ray photons. The TRT detector is composed of around 300,000 thin walled proportional mode drift-chamber "straws" embedded in a fibre radiator matrix, as illustrated in figure 1.7. Each straw is a tube of 4 mm diameter with high-voltage tungsten wire running along its axis as the anode. The cathode is formed from a conductive layer on the inside surface of the Kapton straw. Each straw is filled with Xe and CO_2 (70% /30%). When a charged particle travels through the detector, it ionizes the gas and produces a signal in each straw it passed through. From the timing of each pulse, the positions of the particles can be determined with a precision of about 137 μm. Also, highly relativistic charged particles (eg electrons and positrons) that travel through the fibre matrix radiator, emit transition radiation X-ray photons. These photons ionize the Xe gas. This enables the TRT to distinguish between electrons from slower, heavier charged particles like pions.

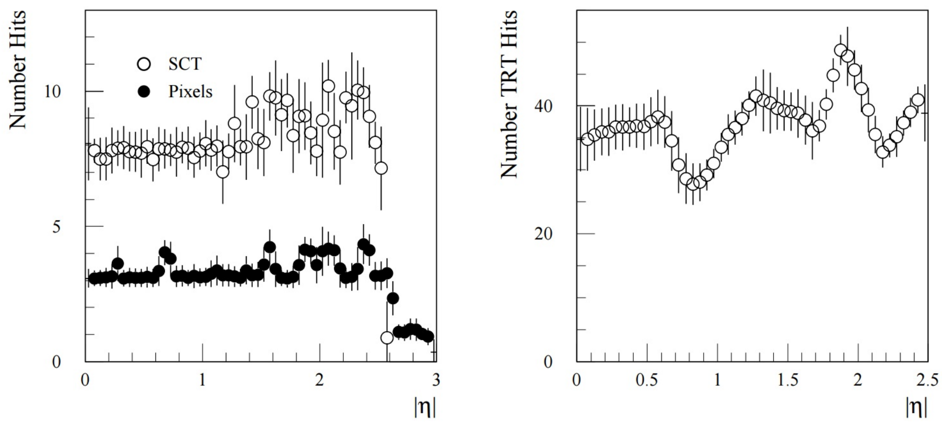

Figure 1.8: Number of Hits per track in the precision detectors and TRT.

The TRT has lower granularity and lower precision per space point, or hit, measurement, compared to the silicon detector. However, on average 36 space point measurements on a track are made in the TRT, compared with an average of seven hits in the silicon detectors. figure1.8 shows the number of Hits in the precision detectors (pixel and SCT) and TRT versus η.

1.5.3 Calorimeters

After traversing the inner detector, interaction products from the intersection point enter the ATLAS calorimetry [27]. The calorimeter system is designed to stop entirely or "absorb" most of the particles coming from a collision, forcing them to deposit all of their energy within the detector. Calorimeters typically consist of layers of "passive" or "absorbing" high-density material

- for example, lead - interleaved with layers of an "active" medium such as liquid argon (LAr). Most particles, except muons and neutrinos, lose all their energy before leaving the ATLAS calorimeter system allowing a measurement of energy and position measurement of electrons, photons, hadrons, taus, and jets as well as providing information for particle identification.

The ATLAS calorimeter system includes Electromagnetic (EM) Calorimeters [28] and Hadronic (HAD) Calorimeters [29].

The EM calorimetry surrounds the inner detector. It is primarily designed to measure the energy of electrons and photons. Also, by utilizing both ID and EM, it is possible to reconstruct electrons and photons that are produced in primary and secondary interactions, originated from p-p collisions at the ATLAS interaction point [39].

The EM calorimetry is divided into a barrel part and two end-caps. The end-cap calorimeter modules placed one at each end of ATLAS consists of an Inner Wheel, the closest part to the interaction point, and the Outer Wheel, the part furthest from the interaction point.

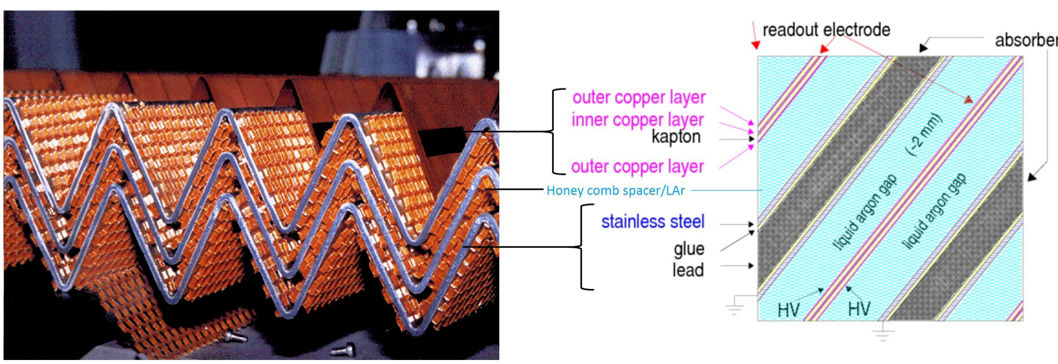

Figure 1.9: Schematic diagram of Electromagnetic barrel accordion calorimeter and a cut away view of inside the accordion geometry.

Figure 1.9 shows a cutaway view of EM barrel calorimeter. A total of

1024 1.8 mm thick lead absorber sheets are folded in accordion shape and stacked in leaving a gap of 3.6 mm between two successive sheets. Although, this configuration leads to longer response time, it allows uniform performance through the detector, low electronic noise and high radiation resistance, and more importantly a good energy and spatial resolution.

A honeycomb layer is used to space the absorber plate layers. The honeycomb structure allows LAr to fill the space between the absorber plates. LAr was chosen as an active material because of its linear response and radiation hardness. The readout electrodes are located between the layer of absorbers and build out of copper plated Kapton sheet (A layer of Kapton sandwiched between copper plates) held in place by the honeycomb structure.

When an incoming particle passes through the absorber, it initiates an electromagnetic shower that ionizes the active layers of the calorimetry the shower traverses, producing charge. The two outer conductive layers of electrode distribute the high voltage over the electrode outer surfaces, when the middle layer collects the charge. The collected charge is proportional to the energy deposited by the EM shower. However, in some cases not all of the energy is deposited in the calorimeter. Sometimes the EM shower can start in the material preceding the EM calorimetry. To correct for any energy lost within the inactive material upstream of the EM calorimeter, a liquid argon pre sampler layer around 11 mm thick is placed in front of the EM inner surface.

The EM end cap calorimetry is comprised of two coaxial wheels. They are built similarly to the EM barrel out of accordion shaped absorbers, electrodes and LAr active material. However, the LAr gap thickness is constant in the Barrel but changing with the radius in the end-Cap. In the inner wheel, the granularity is coarser and there are only two samplings.

At the LHC the particle densities and energies are largest at high $|\eta|$, i.e. in the forward and backward directions. Calorimetry is the only useful detector technology capable of surviving in this harsh environment. The high particles flux causes enormous ionization rate in the LAr and the slowly-drifting ions build up in a large liquid argon gap. In order to avoid ion build-up problems and at the same time to provide the highest possible density of materials to stop particles, a differently structured detector with the smaller LAr gap is needed. The Forward calorimetry is integrated into the end cap calorimetry covering the region $3.1 < |\eta| < 4.9$. In order to have some measurement of longitudinal shower development, the FCal is divided into three sections. All three modules use a novel electrode structure. This consists of copper tubes parallel to the beam axis, which contain electrode rods. In the FCal 1 the electrode rods and the calorimeter matrix are copper. This serves to ensure a good thermal conductivity and avoids local heating of the liquid argon. In order to have an extremely dense detector, the FCal 2 and FCal 3 modules have tungsten electrode rods, and the matrix consists of small sintered tungsten slugs. In all three modules, the LAr gap between the electrode rods, and the copper electrodes tubes is maintained by a spiral of radiation hard PEEK plastic. A cutaway view of FCal is shown in figure 1.10(c)

In the range $|\eta| < 1.6$ the ATLAS hadronic calorimeter is an iron-scintillating tiles calorimeter. In the end cap regions, for $|\eta| > 1.6$, the hadronic calorimeter is an LAr calorimeter, mainly because of the intrinsic radiation hardness of this technology.

The TileCal has a fixed central barrel (LB), and two moveable extended

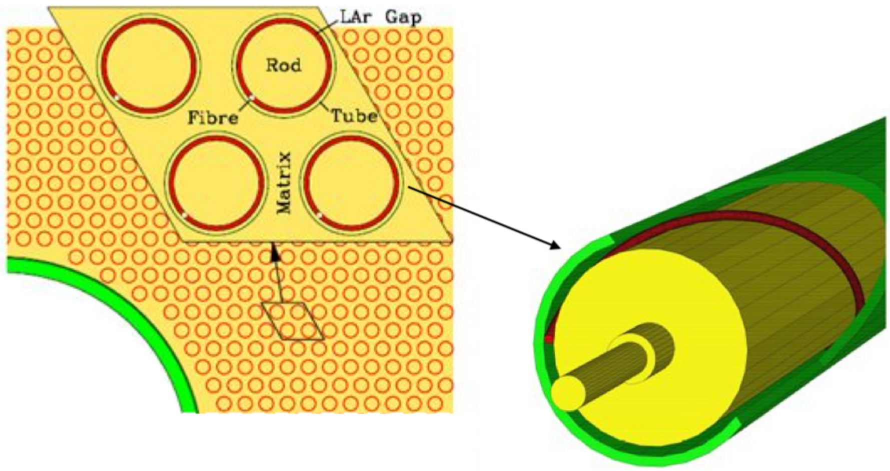

Figure 1.10: Schematic diagram of the FCAL tube.

barrels (EB). The tile calorimeter uses steel as the absorber and plastic scintillator as the active medium which are assembled with alternating layers of steel and scintillating tile, positioned radially to the beam line. A schematic view of the mechanical assembly and the optical readout of a sector of the tile Calorimeter is shown in figure 1.11(b). When a high energy hadron (hadron, jet, and tau) passes through the TileCal, it produces a hadronic shower with an electromagnetic component. The shower is initiated in the steel tiles and propagates through the detector. Gammas and charged particles, generated in the shower, traverse the scintillator material and produce a light signal (the signal is proportional to the energy deposited in the detector).

The Hadronic End-Cap calorimeter (HEC) is an LAr sampling calorimeter which provides hadronic coverage for $1.6 < |\eta| < 3.2$. Each end cap consists of parallel Cu plate absorbers orthogonal to the beam axis and consists of two consecutive wheels with absorber thickness of 25 and 50 mm, respectively. The readout cells are fully pointing in ϕ but only pseudo-pointing in η. The thickness of the active part of the calorimeter is about 12 interaction lengths.

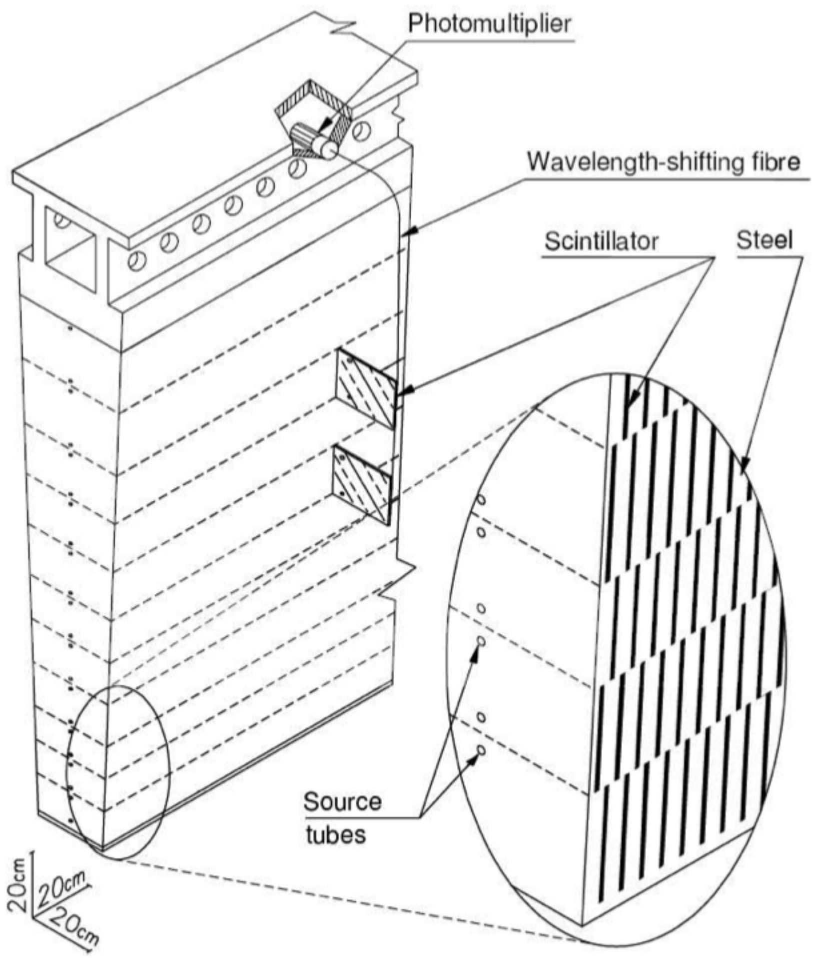

Figure 1.11: Schematic diagram of Tile calorimeter.

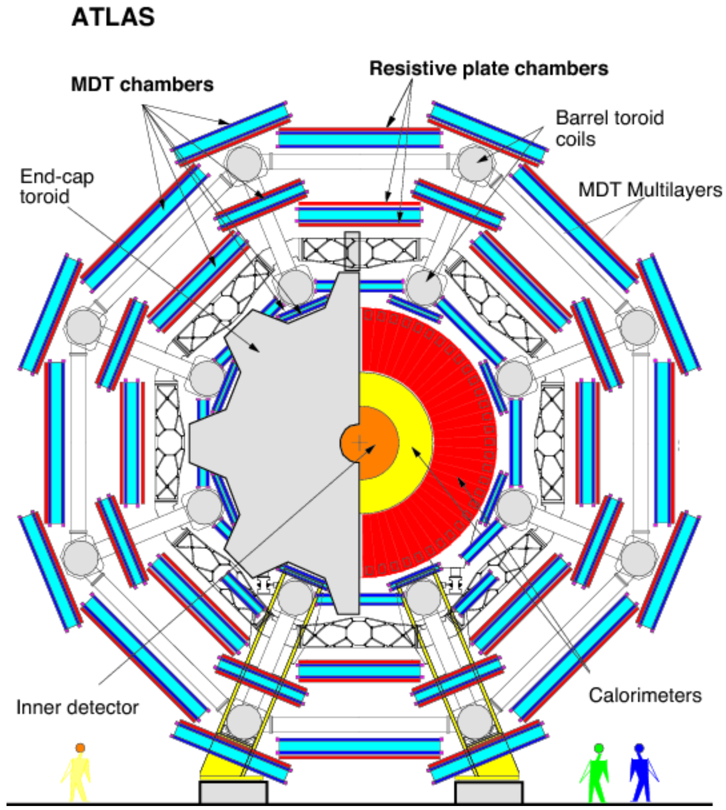

Figure 1.12: Schematic view of a cross-section of the Muon Spectrometer.

1.5.4 Muon Spectrometer (MS)

The muon spectrometer (MS) [30] is the outermost detector of ATLAS. It is designed to measure high-p_T muons with a high precision, independent of the inner detector. The MS also provides an independent muon trigger. The MS integrates four different detector technologies and the barrel and end cap toroid magnets. Most parts of the MS are located within a roughly $4T$ magnetic field that is produced by a large superconducting toroidal magnet in the barrel region and smaller toroidal magnets in the end-cap region. Figure 1.12 shows the schematic view of the MS.

The MS is built out of different types of muon chambers that are designed either for precise tracking or that can be used in triggering. Monitored Drift Tubes (MDTs) [31] and Cathode Strip Chambers (CSCs) [32] provide precise spatial measurements for muon tracking, of the order of 20 microns, in the bend plane. The muon trigger systems utilizes Resistive Plate Chambers (RPCs) [33] and Thin Gap Chambers (TGCs) [34], which also provide spatial tracking with precision of few millimetres in the η and ϕ plane.

The barrel region of the MS consists of three concentric cylindrical regions comprised of MDT and RPC chambers, as shown in figure 1.12. A MDT tube is an aluminium gas filled (Ar:CO_2 = 93:7) tube with a diameter of 30 mm. An anode wire is positioned along the central axis of the tube and the tube wall functions as the cathode.

An MDT chamber consists of two multilayers, which in turn consist of three or four layers of tubes each. In the barrel region ($|\eta| < 1.3$; the MDTs are positioned in three concentric layers around the beam axis, at an approximate radius of 5 m, 8 m, and 10 m. There is a 16-fold segmentation in ϕ, which are called sectors. The innermost layer of chambers has four layers of tubes.

The end cap ($1.3 < |\eta| < 2.4$) MDT chambers are assembled onto three wheels, positioned at z = 7.5 m, 14 m, and 22.5 m. These chambers have a trapezoidal shape.

The MDT chambers are installed with a precision of about 5 mm and 2 mrad with respect to their nominal position. To achieve the required momentum resolution, the positions of the chambers need to be known to a precision smaller than 30 μm. Optical alignment sensors along with though going muon tracks are used to maintain the alignment of the MDTs over time.

The RPC is a gaseous detector with 2 mm gas-gaps in between two parallel resistive plates. The gas-gaps are filled with ($C_2H_2F_4$:C_4H_{10}:SF_6 = 94.7:5:0.3). Metallic strips are mounted onto these plates with a pitch between separate ϕ (η) strips of 23 (35) mm. The plates are operated at a voltage difference of 9.84 kV, as a result of which a charged particle crossing the gas-gap will create an avalanche of electrons drifting towards the anode. Each chamber consists of two units, placed next to each other with a small overlap. Each unit has two gas-gaps, one for ϕ and one for η.

The fast response and precise timing characteristics allow the RPC detector to make a rapid measurement of the muon momentum, which is then used to make a trigger decision. Moreover, RPC precise time resolution of approximately 1.5 ns gives it the ability to distinguish individual bunch crossings.

In the end-cap of muon spectrometer, the MDT chambers are complemented by the Cathode Strip Chambers (CSC). CSC chambers are used in the innermost tracking layer due to their ability to withstand higher rates and beam related backgrounds. Triggering in the end-cap regions is performed using TGCs. The CSC is an argon filled multi-wire proportional chambers, composed of closely spaced arrays of anode wires oriented in the radial direction and crossed with panels of copper strips as the cathodes. The perpendicular strip and wire structure allow both coordinates to be measured for each passing particle. The resolutions are roughly 40 μm and about 5 mm [2] in the bending plane and in the non-bend plane, respectively.

The muon track in the MS is reconstructed in two steps. In the first step the muons are triggered in the RPC and TGC and then local track segments are defined in each layer of chambers. In the next step, the local track segments

[2]It is enough for the momentum direction measurement

from different layers are combined to form a full MS track. To reduce the probability of background tracks being reconstructed in the calorimeter, the tracks of the muon candidates are required to point towards the interaction point.

1.5.5 Forward Detectors

In addition to the central ATLAS detector systems, four smaller sets of detectors AFP, ALFA, LUCID and ZDC [65, 38, 60, 37] have been built in the forward region. The LUCID and ZDC detectors are situated on both sides of the interaction point; mainly to detect forward neutrons and to measure the luminosity of the LHC and ATLAS respectively. The main purpose of the ALFA detector is to measure elastic proton scattering. The AFP detector was relatively recently installed in the forward region of ATLAS aiming to detect deflected protons from exclusive interactions. These forward detectors will be discussed in more detail directly below. In addition, my contributions to the development of the LUCID and AFP detectors will be described in Chapters 3 and 4.

AFP(ATLAS Forward Proton):

AFP is a proton tagging detector which consists of $2 + 2$ stations installed at ± 205 and ± 217 m from the interaction point on each side of the ATLAS intersection point. Each station includes silicon-based trackers and Cherenkov based time of flight detectors. The main purpose of AFP is to identify events in which one or two protons emerge intact from the proton-proton collisions.

ALFA (Absolute Luminosity For ATLAS):

ALFA is designed to determine the total p-p cross-section as well as the luminosity by measuring elastic proton scattering at very small angles. It is made of four Roman Pot stations, located in the LHC tunnel in a distance of about ± 240 m from the interaction point. Each station is equipped with tracking detectors, inserted in Roman Pots which approach the LHC beams vertically. The tracking detectors, which measure the positions of protons in the transverse plane to the LHC beam, are made of scintillating square fibres and read out by MultiAnode PMTs (MAPMTs), with custom made electronics.

LUCID (Luminosity measurements Using Cherenkov Integrating Detector):

The LUCID detector is the only detector of ATLAS that is dedicated solely for luminosity monitoring and determination, when calibrated using the Van de Meer (VDM) process.The LUCID-2 detector was commissioned in 2015, replacing LUCID-1 which was installed in 2008. The detector is deployed at ± 17 m for the ATLAS Intersection Point. Each detector consists of 16 10 mm diameter photomultipliers (PMTs) arranged in 4 groups around the beam-pipe and with 4 quartz fibre bundles is readout by PMTs situated 1.5 m away from the detector inside the muon shielding. LUCID uses small amounts of radioactive ^{207}Bi sources deposited on to these windows to monitor the gain stability of the photomultipliers. The result is a fast and accurate luminosity determination that can be kept stable during many months of data taking.

ZDC (The Zero Degree Calorimeters):

ZDCs are compact calorimeters which are placed symmetrically at about ±140 m from the interaction point, where the straight section of single beam-pipe divides into two independent beam-pipes. The primary purpose of the ATLAS Zero-Degree Calorimeters (ZDC) is to detect forward neutrons and photons with $|\eta| > 8.3$, in both proton-proton and heavy-ion collisions. For heavy Ion collisions the ZDC's play a key role in determining the centrality of such collisions, which is strongly correlated to the number of very forward (spectator) neutrons. For p-p collisions with luminosities well below 10^{33} $cm^{-2}s^{-1}$, the ZDC will enhance the acceptance of ATLAS central and forward detectors for diffractive processes and provide an additional minimum-bias trigger for ATLAS. Significant backgrounds in hadron-collider experiments are created by beam-gas and beam-halo effects. These can be greatly reduced by requiring a tight coincidence from the two arms of the ZDC's, located symmetrically with respect to the interaction point.

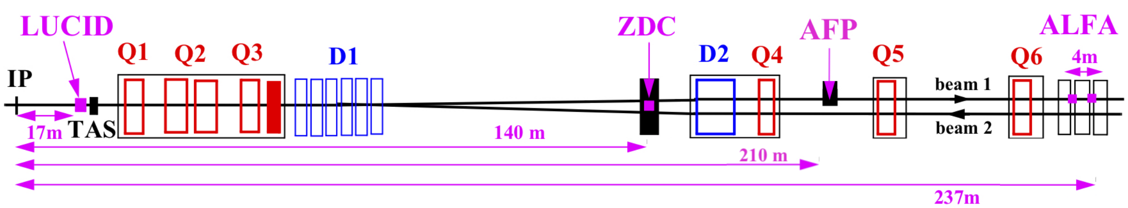

Figure 1.13: A sketch of the ATLAS Forward map, not to scale, showing the positions of ATLAS detectors in the forward region on one side of the interaction point of ATLAS.

1.5.6 Trigger and Data Acquisition Systems (DAQ)

When the LHC is operating at full design luminosity each proton beam will be comprised of 2808 filled bunches, separated by 25 ns, corresponding to a bunch collision rate of 40 MHz. ATLAS is designed to observe up to one billion p-p collisions per second, with a combined data volume of more than 60 million megabytes per second. However, only a small subset of these events will yield interesting - as defined by the ATLAS Physics Program - high transverse momentum events. Also, it is only practically feasible to readout a small fraction of the available data. To reduce the flow of data to manageable levels, ATLAS uses a specialized multi-level trigger system. ATLAS has adopted two-stage trigger system [35, 36], Level1(L1) and Event Filter(EF), to reduce the incoming bunch crossing rate from 40 MHz to a few hundred kHz in L1 stage and then to a few kHz in the EF stage.

The L1 trigger is a hardware-based. A high-speed pipeline is used to process a huge amount of data from trigger chambers of the MS, as well as reduced-granularity information from all calorimeters. In order to be able to select a few hundred interesting events per second from millions of events generated per second, for permanent storage and subsequent analysis, the L1 trigger selects events with isolated high transverse-energy electrons, gammas, muons, jets, and taus as well as missing transverse energy.

The L1 trigger gathers and analyses data from the MS and calorimetry to make its decision. The Central Trigger Processor (CTP) is fed by signals coming primarily from the dedicated trigger hardware in the calorimeter (L1Calo) and muon (L1Muon) detector systems. The L1Calo uses calorimeter energy deposits to identify various types of high transverse energy particles as well as energy sums of interest. The L1Muon trigger input uses the track information from muon chambers to identify high transverse momentum muon candidates. The CTP implements a trigger menu based on a logical combination of results from both L1Calo and L1Muon. From this information, L1 trigger identifies a region of interest (ROI) which contains the information about the coordinates of the particles as well as their thresholds transverse energy which is used to seed the selection process in the higher level trigger (HLT).

In Run 1, HLT used a two-level software trigger consisting of the L2 trigger and Event Filter stages (EF). The L2 trigger is a software based trigger formed in large PC farms. It is seeded by the RoI to reconstruct the events in greater detail using information from the inner detector track reconstruction and more precise energy deposition from calorimeter. This additional information is used to limit the amount of data to about few kHz. The EF works in a similar way to Level 2, but with a longer latency. At this level, the offline reconstruction algorithms were used and the events are formed for the first time to reduce the final trigger rate to few kHz.

The trigger/DAQ was upgraded for Run 2. The upgrades include a faster Readout System (ROS) leading to higher data readout rates. Also, the level-1 trigger uses data from other detectors, in addition to the MS and calorimeters. However, the main update was made to the higher level triggers. The L2 and EF stage were merged and run together with the event building within the same processing unit. In addition, a new network design was implemented in order to merge the two existing networks, L2 and EF, into one calls the “HLT” network. Ultimately, the high capacity memory transfer between the two levels allows tighter coupling of the algorithms and reduces CPU and network usage. Moreover, a flexible event-building system allows network traffic to be optimized. Figure 1.14 shows the new design of trigger/DAQ architecture design and the design values of latencies and sustained rates [35, 36].

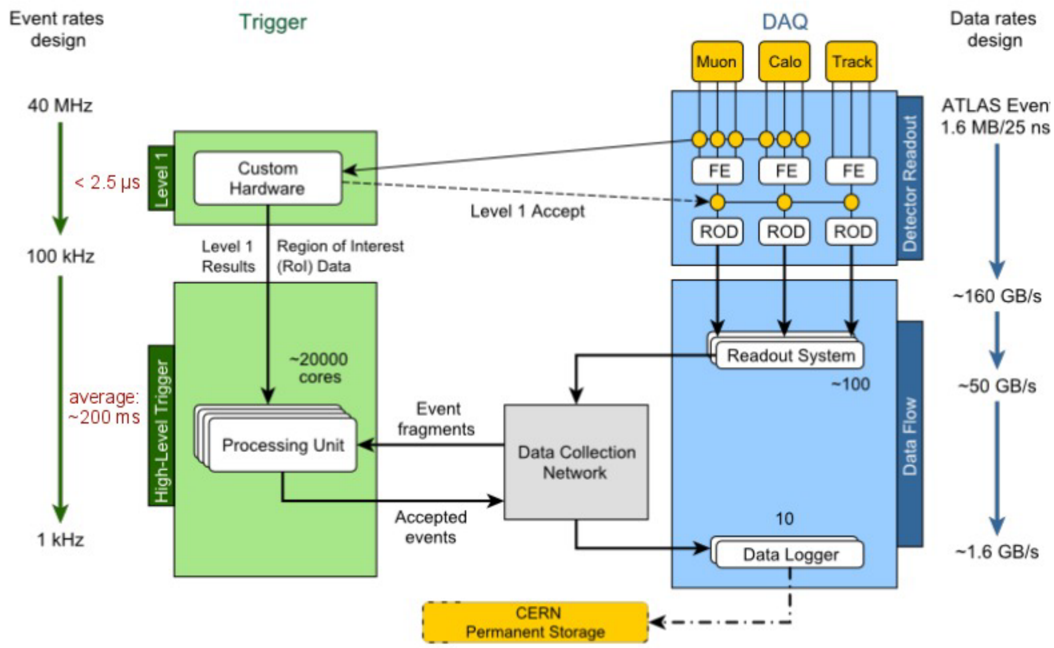

Figure 1.14: Overview of the ATLAS TDAQ system during Run 2.

Chapter 2

Standard Model And The Higgs Boson

2.1 Standard Model

The Standard Model (SM) [40] is a relativistic Quantum Field Theory (QFT) that provides a mathematical framework to describe the interactions of all the known fundamental particles. There are two classes of fundamental particles: the spin-half particles called fermions which are further sub-divided into leptons (e, μ, τ and their neutrinos) and quarks (u, d, c, s, t, b), leptons with integer and quarks with third-numbered electric charges. They interact through the second type of particles, spin-1 force carriers or gauge bosons, which are particles that mediate the fundamental forces of the Standard Model. Three out of the four forces of nature, electromagnetic, weak, and strong forces are included in the standard model. However, the last force, gravity, is not part of the Standard Model. Luckily, in particle physics, when it comes to the minuscule scale of fundamental particles, the effect of gravity is weak enough to be negligible. It has strength of 6×10^{-39} relative the strength of the strong force. The electromagnetic and weak force, respectively, have the strength of $\frac{1}{137}$ and 10^{-5} in comparison to the strong force.

Electromagnetic Force

The electromagnetic force, classically described by the Maxwell equations, is carried by the spin-1 massless photon. Every particle that has non-zero charge, couples to the photon and is therefore sensitive to the electromagnetic force. This includes all fermions except neutrinos and the charged W-bosons of the weak force.

Weak Force

The weak force is carried by three bosons: two charged W-bosons with the mass of 80.379 GeV and the neutral Z with the mass of 91.1876 GeV. The $W^{\pm}$ and Z couple to the third component of the weak isospin, I_3. It is defined as $I_3 = Y - Q$, where Y stands for the weak hypercharge accounting for quark mixing and Q is the electrical charge. The weak force bosons couple to left-handed quarks and leptons and to themselves, neutrinos only interact weakly. The charged W bosons also couple to the photon. In the Standard Model the electromagnetic and weak force are combined into a single electroweak force [41, 42].

Strong Force

The particles carrying the strong force are called gluons, there are eight of them. The gluons couple to colour-charged particles, including quarks and gluon itself. A gluon consists of two colour-charges. Quarks, in contrast to gluons, carry only one colour-charge and are combined into colourless hadrons, which may be a meson ($q\bar{q}$) or a baryon (qqq or $\bar{q}\bar{q}\bar{q}$). The quarks are confined within hadrons [45].

The Higgs Boson

The Standard Model (SM) predicts the existence of a scalar boson (spin=0), called the Higgs boson, the fundamental quantum of the Higgs field. The Higgs mechanism is responsible for the masses of the W and Z bosons. The rest masses of the charged fermion arise from Yukawa-type interactions with the Higgs field. What appears to be the Standard Model Higgs boson, with measured mass of around 125 GeV, was discovered in 2012 by the ATLAS and CMS experiments at the LHC [50].

In the SM, all types of interactions between particles are described by a local gauge symmetry based on the group structure, $SU(3)_C \times SU(2)_L \times U(1)_Y$[3]. The $SU(3)_C$ group describes the symmetry of strong interaction in theory of Quantum Chromodynamics (QCD), and $SU(2)_L \times U(1)_Y$ describes the electroweak interaction. The spontaneous breaking of this symmetry triggers the Higgs mechanism which introduces masses for the particles by coupling them to the Higgs field.

All the elementary particles of the Standard Model and their names,

[3] C stands for colour, Y is the weak hypercharge and L the left handedness

masses, spins, charges, chirality, and interactions with the strong, weak and electromagnetic forces are shown in figure 2.1.

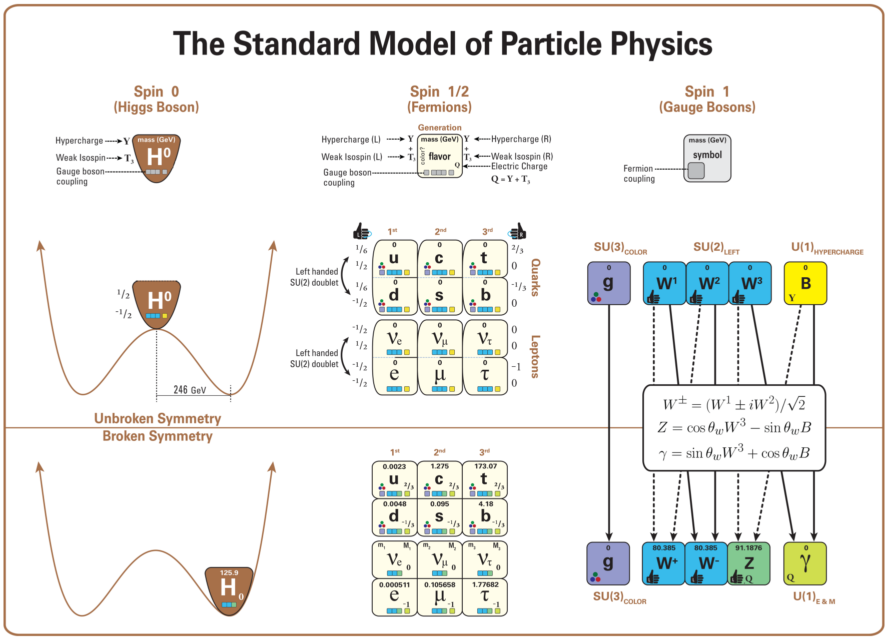

Figure 2.1: The diagram shows the elementary particles of the Standard Model, the Higgs boson, the three generations of quarks and leptons, and the gauge bosons, including their name, mass, spin, charge, chirality, and interactions with the strong, weak and electromagnetic forces. It also shows how the properties of the various particles differ in the symmetric phase and broken-symmetry phase

2.1.1 Quantum Electrodynamics (QED)

In QFT, a fermion with mass m is described by the Dirac equation for a free fermion field $\Psi(x)$ and a spin zero boson with mass m is described by Klein-Gordon equation for a complex scalar field $\phi(x)$ as follows:

$$\text{Klein-Gordon equation: } (\partial_\mu \partial^\mu + m^2)\phi(x) = 0 \tag{2.1}$$

$$\text{Dirac equation: } (i\gamma^\mu \partial_\mu - m)\Psi(x) = 0 \tag{2.2}$$

The Lagrangian densities, $\mathcal{L}$, extracted from Klein-Gordon equation and Dirac equation are:

$$\mathcal{L}_{KG} = \frac{1}{2}(\partial^{\mu}\phi^{*}\partial_{\mu}\phi - m^{2}\phi^{*}\phi) \tag{2.3}$$

$$\mathcal{L}_{Dirac} = \bar{\Psi}(i\gamma^{\mu}\partial_{\mu} - m)\Psi \tag{2.4}$$

In the above equation the symbols γ^{μ} represent Dirac matrices, and $\bar{\Psi} = \Psi^{\dagger}\gamma^{0}$, where $\Psi^{\dagger}$ is the hermitian conjugate of the field.

Quantum electrodynamics (QED) introduces the photon in the Lagrangian of a (fermionic) Dirac field and describes the electromagnetic interactions between them. QED is an Abelian gauge theory based on $U(1)$ symmetry group. The local gauge transformation of the U(1) group is defined as:

$$\Psi(x) \to \Psi'(x) = \Psi(x)e^{-iq\alpha(x)} \tag{2.5}$$

In order for Lagrangian density to be gauge invariant under this transformation, a covariant derivative must be introduced and defined as:

$$\partial_{\mu} \to D_{\mu} = \partial_{\mu} - iA_{\mu}(x) \tag{2.6}$$

where A_{μ} is the so-called gauge transformation of the photon field. To make the Lagrangian of Dirac field invariant under $U(1)$ transformation the gauge field transformations must be:

$$A_{\mu}(x) \to A'_{\mu}(x) = A_{\mu}(x) + \partial_{\mu}\alpha(x) \tag{2.7}$$

where $\alpha(x)$ is a real arbitrary function. Therefore, the Lagrangian of Dirac field becomes:

$$\mathcal{L} = \mathcal{L}_{fermion} + \mathcal{L}_{interaction} = \bar{\Psi}(i\gamma^{\mu}\partial_{\mu} - m)\Psi - q\bar{\Psi}\gamma^{\mu}\Psi A_{\mu} \tag{2.8}$$

where the first part in the equation describes the kinetic energy of the free fermion field, the second (includes the mass of fermion) corresponds to the self interaction and the third term describes the electromagnetic interaction between the fermion and photon fields. In the above equation q is the electric charge of the fermion. The QED Lagrangian would not be complete without a term describing free photons, $F_{\mu,\nu}F^{\mu,\nu}$. Therefore, the complete QED Lagrangian is described by:

$$\begin{aligned}\mathcal{L}_{QED} &= \mathcal{L}_{fermion} + \mathcal{L}_{interaction} + \mathcal{L}_{photon} \\ &= \bar{\Psi}(i\gamma^{\mu}\partial_{\mu} - m)\Psi - q\bar{\Psi}\gamma^{\mu}\Psi A_{\mu} - \frac{1}{4}F_{\mu,\nu}F^{\mu,\nu}\end{aligned} \tag{2.9}$$

where $F_{\mu,\nu} = \partial_{\mu}F^{\nu} - \partial_{\nu}F^{\mu}$. If one naively try to add a mass term for the photon, $\frac{1}{2}m_{\gamma}A_{\mu,\nu}A^{\mu,\nu}$, to the Lagrangian, the Lagrangian breaks the local phase invariance which requires the gauge boson of QED to be massless.

2.1.2 Weak Interaction

The gauge invariance principle utilized in QED can extend to model the weak interactions. However, the weak interaction is unique in a number of respects: QED is fully described by taking a Lagrangian that is invariant under the $U(1)$ symmetry; likewise the weak interaction is described along the same line by taking $SU(2)$ symmetry. The different gauge group in each symmetry gives back the number of different force carriers in each case: for instance photon is the force carrier in the electromagnetic field and $W^{\pm}$ and Z bosons are gauge bosons for the weak interaction. Also, similarly to the electric charge, there is an associated conserved quantity under the action $SU(2)$ which is referred to as isospin.

Unlike the electromagnetic interaction, which obeys the parity and charge (CP) symmetry, the weak interaction violates CP symmetry. In parity-symmetric theories such as QED, the left-handed (L) and right-handed (R) particles are indistinguishable. On the other hand, if the weak interaction violates parity-symmetry right- and left-handed particles will interact differently. All fermions interact via the weak interaction.The left-handed and right-handed fermion fields are defined by acting the projection operator, $P_{\pm} = -\frac{1 \pm \gamma^5}{2}$, on fermion fields as follows:

$$\begin{aligned} \Psi_L &= P_- \Psi \\ \Psi_R &= P_+ \Psi \end{aligned} \tag{2.10}$$

Therefore, fermions appear as families with left-handed doublets of quarks and leptons ($I_3 = \pm\frac{1}{2}$) and right-handed singlets of quarks and leptons ($I_3 = 0$).

$$
\begin{pmatrix} e \\ \nu_e \end{pmatrix}_L, e_R \qquad \begin{pmatrix} \mu \\ \nu_\mu \end{pmatrix}_L, \mu_R \qquad \begin{pmatrix} \tau \\ \nu_\tau \end{pmatrix}_L, \tau_R
$$
$$
\begin{pmatrix} u \\ d \end{pmatrix}_L, u_R, d_R \qquad \begin{pmatrix} c \\ s \end{pmatrix}_L, c_R, s_R \qquad \begin{pmatrix} t \\ b \end{pmatrix}_L, t_R, b_R \tag{2.11}
$$

2.1.3 The Electroweak Model

The electroweak model (EW) developed in the 1960s by Glashow, Weinberg, and Salam unifies electromagnetic and weak interactions under $SU(2) \times U(1)$ symmetry group [41, 42, 43]. The gauge group of $SU(2) \times U(1)$ is described by four vector fields, three of which are associated with the $SU(2)$ group that will be called W_μ^a, where a = 1, 2 or 3 and an A_μ associated with the $U(1)$ group. The structure of the gauge theory is determined by the form of the covariant derivative, $D_\mu = \partial_\mu + igW_\mu^a T_a + ig' B_\mu Y$ which acts on left-handed field, ψ_L, and $D_\mu = \partial_\mu + ig' B_\mu Y$ which acts on right-handed field, ψ_R, where hypercharge and Pauli matrices are shown with Y and T_a (a = 1, 2 or 3), respectively and they are the generators of $SU(2)_L \times U(1)_Y$. B_μ and W_μ^a are the electroweak gauge boson transforming as follows:

$$
\begin{aligned}
B_\mu(x) \to B'_\mu(x) &= B_\mu(x) - \frac{1}{g}\partial_\mu \alpha(x) \\
W_\mu^i(x) \to W_\mu^{\prime i}(x) &= W_\mu^i(x) - \frac{1}{g'}\partial_\mu \beta^i(x) - \epsilon_{ijk}\beta^j W_\mu^k
\end{aligned} \tag{2.12}
$$

where ϵ_{ijk} are the $SU(2)_L$ structure constants, g and g' are coupling constants of the weak and electromagnetic interactions, respectively. The gauge transformations are:

$$\begin{aligned}
\psi_L &\rightarrow \psi'_L = e^{iY_L\alpha(x)}e^{iT^i\beta_i(x)}\psi_L \\
\psi_R &\rightarrow \psi'_R = e^{iY_R\alpha(x)}\psi_R
\end{aligned} \tag{2.13}$$

The EW Lagrangian that describes fermions and gauge bosons as massless particles can be expressed as:

$$\begin{aligned}
\mathcal{L}_{EW} &= \mathcal{L}_{fermion} + \mathcal{L}_{gauges} \\
&= \sum i\bar{\Psi}\gamma^\mu D_\mu \Psi - \frac{1}{4}B_{\mu\nu}B^{\mu\nu} - \frac{1}{4}W_{\mu\nu}W^{\mu\nu}
\end{aligned} \tag{2.14}$$

where

$$\begin{aligned}
W_{\mu,\nu} &= \partial_\mu W^\nu - \partial_\nu W^\mu - ig'[W_\mu, W_\nu] \\
B_{\mu,\nu} &= \partial_\mu B^\nu - \partial_\nu B^\mu
\end{aligned} \tag{2.15}$$

The EW Lagrangian density describes fermions and gauge bosons as massless particles since just like gauge bosons W's and B, it is not possible to simply add a mass term for fermions to the Lagrangian. Such a Dirac mass term,

$$m\bar{\Psi}\Psi = m\overline{(\Psi_L + \Psi_R)}(\Psi_L + \Psi_R) = m(\bar{\Psi}_L\Psi_R + \bar{\Psi}_R\Psi_L) \tag{2.16}$$

contains couplings of left- and right-handed fields, which have different transformation properties, spoiling the gauge symmetry.

In the following subsection we will discuss the mass generation both for the electroweak gauge bosons and for the fermions through the elaborate mechanism of spontaneous symmetry breaking.

2.2 Higgs Mechanism

2.2.1 Spontaneous Symmetry Breaking

We could easily make a massless theory for fermions and gauge bosons. But, from experiment we know that weak gauge bosons and fermions are all massive particles. Adding a mass term to the Lagrangian makes the theory non-invariant under the $SU(2) \times U(1)$ gauge transformation. The Higgs mechanism is a theoretical framework which explains how the masses of $W^{\pm}$ and Z bosons arise through the spontaneous breaking of Electroweak symmetry, $SU(2) \times U(1)$.

In order to spontaneously break local $SU(2) \times U(1)$ gauge symmetry a complex scalar $SU(2)$ doublet field is introduced as:

$$\phi = \frac{1}{\sqrt{2}} \begin{pmatrix} \phi_1 + i\phi_2 \\ \phi_3 + i\phi_4 \end{pmatrix} \tag{2.17}$$

The Lagrangian extracted from Klein-Gordon equation for a complex scalar field $\phi^+ = \phi_1 + i\phi_2$ and $\phi^0 = \phi_3 + i\phi_4$, is given by:

$$L(\phi) = (D^\mu \phi)^+ D_\mu \phi - V(\phi) \tag{2.18}$$

The simplest possible potential that will respect SM symmetry is $V(\phi) = \mu^2 \phi^\dagger \phi + \lambda(\phi^\dagger \phi)^2$. μ is associated with the mass of the scalar field and λ term

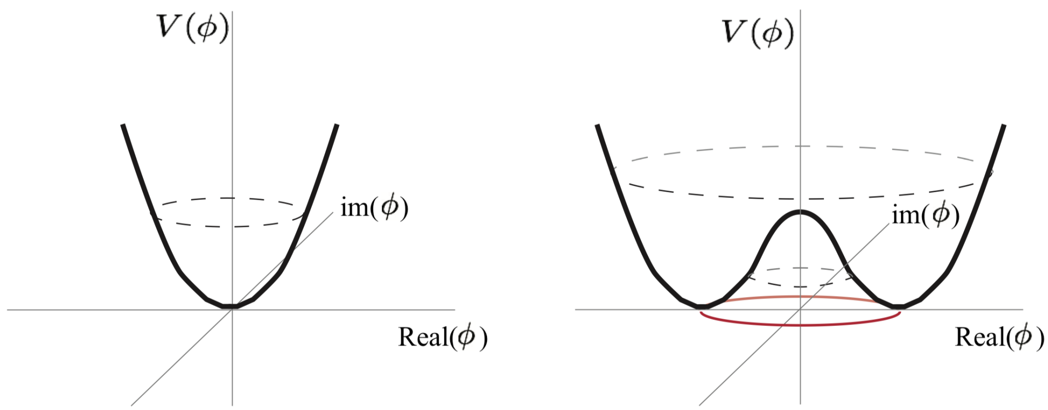

Figure 2.2: (Left) For $\mu^2 > 0$ there is a unique ground state at $\phi = 0$. (Right) For $\mu^2 < 0$ the ground state is degenerate.

describes quartic self-interactions among the scalar fields. Vacuum stability demands λ to be greater than zero. Therefore, there are two possibilities for the sign of μ^2. For the positive μ^2, the field ϕ has an absolute minimum at zero and the minimum energy of the field is unique and can't break the symmetry. However, in the case that μ^2 takes a negative sign, the potential has a Mexican hat shape and the minimum is no longer set at zero, but there is a set of minima at $\phi^2 = \frac{\mu^2}{\lambda} = \nu^2$. This is shown in figure 2.2. In order to expand $\phi(x)$ around its minimum in perturbation theory, a particular value is chosen for the minimum which breaks the symmetry. Therefore, the chosen field is:

$$\phi_0 = \begin{pmatrix} 0 \\ \nu \end{pmatrix} \tag{2.19}$$

To see what particles are present in this model, the behaviour of the Lagrangian is studied under small perturbation around the vacuum. Therefore, perturbations around the vacuum are described by:

$$\phi(x) = \begin{pmatrix} 0 \\ \nu + h(x) \end{pmatrix} \tag{2.20}$$

where $h(x)$ is the scalar Higgs field representing a perturbation around the vacuum. Substituting the vacuum expectation value of the scalar field into the Lagrangian of EW, the relevant mass term is:

$$\begin{aligned}
\Big|(\frac{ig'Y}{2}A_\mu + ig\tau_a)\phi\Big|^2 =& \frac{1}{8}\left|\begin{bmatrix} gW_\mu^3 + g'A_\mu & g(W_\mu^1 - iW_\mu^2) \\ g(W_\mu^1 - iW_\mu^2) & -gW_\mu^3 + g'A_\mu \end{bmatrix}\begin{bmatrix} 0 \\ \nu \end{bmatrix}\right|^2 \\
=& (\frac{\nu g}{2})^2 W_\mu^+ W^{+\mu} + \frac{\nu^2}{8}\begin{bmatrix} W^{3\mu} & A^\mu \end{bmatrix}\begin{bmatrix} g^2 & -gg' \\ -gg' & -g^2 \end{bmatrix}\begin{bmatrix} W^{3\mu} \\ A^\mu \end{bmatrix}
\end{aligned} \tag{2.21}$$

The physical charged weak boson is defined as $W^\pm = \frac{W_1 \mp W_2}{\sqrt{2}}$. So the first term shows the mass of charged boson which is $(\frac{1}{2}\nu g)^2$. The two remaining neutral gauge bosons Z_μ and A_μ are defined as:

$$Z_\mu = \frac{(gW_\mu^3 - g'B_\mu)^2}{g^2 + g'^2} \tag{2.22}$$

with the mass $M_z = \left(\frac{\nu g}{2}\right)^2$ and,

$$A_\mu = \frac{(g'W^3_\mu - gB_\mu)^2}{g^2 + g'^2} \tag{2.23}$$

with the mass, $m_A = 0$. The mass of the Higgs boson is $m_H = \sqrt{2\lambda\nu}$ and from the experimentally measured gauge boson masses and weak coupling the vacuum expectation value of Higgs field is $\nu = 246$ GeV.

Here the point is that a Lagrangian with a complex scalar doublet and four massless vector bosons has twelve degrees of freedom: four from the scalars and eight from the vector bosons. Through the Higgs mechanism, the Lagrangian is transformed into one real massive scalar, three massive vector bosons, and one massless vector boson. The massless vector boson is, of course, to be identified as the photon and the single remaining scalar as the Higgs boson. Counting degrees of freedom again: one from the Higgs, two from the photon and nine from the massive vector bosons, again adds up to twelve.

In the next section, it will be shown that the same scalar Higgs doublet generates the mass for fermions.

2.2.2 Fermion Mass

As we mentioned in the previous section the mass term for fermion $m\bar{\Psi}\Psi = m\bar{\Psi}_L\Psi_R + m\bar{\Psi}_R\Psi_L$ is not invariant under the $SU(2)_L \times U(1)_Y$ gauge symmetry. However, fermions can be given mass via the Yukawa mechanism. That is, when we add terms to the Lagrangian where the complex Higgs doublet ϕ couples to the doublet of left-handed $\bar{\Psi}_L = \begin{pmatrix} e \\ \nu_e \end{pmatrix}$ fermions and to the one right-handed fermion $\bar{\Psi}_R = e_R$ as shown in the following equation.

$$L_{Yukawa} = -G_e \bar{\Psi}_L \phi \Psi_R - G_e \bar{\Psi}_R \phi \Psi_L \tag{2.24}$$

The above equation not only describe an interaction between the Higgs field and fermion, but also how the fermions acquire a finite mass if the complex Higgs doublet ϕ has a non zero expectation value such as $\phi_0 = \begin{pmatrix} 0 \\ V + h \end{pmatrix}$.

Therefore, mass of the Higgs boson can be determined by substituting $\phi_0(x)$ in equation 2.24.

$$\begin{aligned} L_e &= -G_e \begin{pmatrix} \bar{\nu}_e, \bar{e} \end{pmatrix} \phi e_R - G_e \bar{e}_R \phi \begin{pmatrix} e \\ \nu_e \end{pmatrix} \\ &= \frac{G_e V}{\sqrt{2}} e\bar{e} + \frac{G_e}{\sqrt{2}} h e \bar{e} \end{aligned} \tag{2.25}$$

The first term shows the electron mass term and the second term represent the electron-Higgs interaction. The mass of electron is then $m_e = \frac{VG_e}{\sqrt{2}}$. However, the Higgs mechanism does not say anything about the value of the electron mass since G_e is a free parameter.

Because neutrinos are described by a chiral left-handed flavour neutrino field, they can't interact with Higgs boson and they are left massless in the SM. However, experimental evidences show flavour neutrino oscillation which mixes neutrino flavour states with neutrino mass states, requires neutrinos to have nonzero masses.[48, 49]. Neutrinos do not seem to get their masses the way other particles do, through the interaction with Higgs boson. The ways that the Standard Model can be extended to include finite neutrino masses are described in details elsewhere [51, 52].

2.3 The Higgs Boson Production and Decay at Hadron Colliders

In the previous chapters we mentioned that the SM Higgs boson is a CP-even spin zero neutral particle. Its mass is given by $m_H = \sqrt{2\lambda\nu}$, where λ characterizes the Higgs self-coupling. However, because λ is a free parameter, the Higgs boson mass is not predicted by SM. However, the Mass of Higgs boson can be measured experimentally.

The SM Higgs boson is produced at the LHC mainly via four main processes: gluon fusion production $gg \to H$; vector boson fusion production $q'q \to q'qH$; associated production with a W boson or a Z boson; Higgs-Strahlung process $q'q \to WH, ZH$ and a small contribution from $gg \to ZH$, associated production with a pair of bottom quarks $qq'/gg \to b\bar{b}H$ or top quarks $qq'/gg \to ttH$, and associated production with a single top quark through t-channel $qg \to tHq'b$ processes and in association with a W boson $gb \to tHW$. Leading order diagrams for these Higgs boson production mechanisms at the LHC are shown in figure 2.3.

Production cross-sections for the various Higgs boson processes at 8 TeV centre of mass energy are predicted in [44] are shown in figure 2.4.

For a Higgs boson with a mass of about 125 GeV the SM predicts a mean life time of about 1.6×10^{-22} s and after that it will decay to gauge boson, quarks, gammas and muons. Figure 2.5 shows the Standard Model prediction

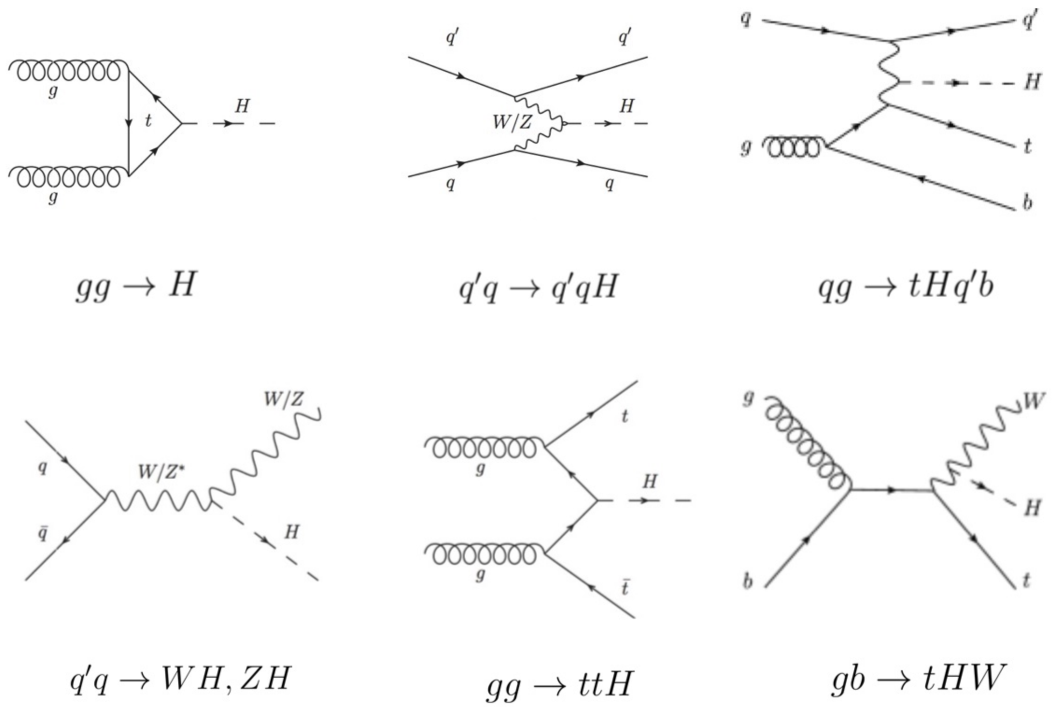

Figure 2.3: Leading order diagrams for Higgs boson production mechanisms at the LHC.

for the branching ratios of the different decay modes of the Higgs particle depends on the value of its mass.

In 2012, both ATLAS and CMS announced the discovery of a new boson consistent with the Standard Model Higgs boson by examining the results of Higgs searches in a number of decay channels $H \to WW, ZZ, b\bar{b}$, and $\tau^+\tau^-$ in the 2011 dataset at a centre of mass energy of 7 TeV with integrated luminosity of $4.6-4.8 fb^{-1}$ and also part of the 2012 dataset from decay channels $H \to \gamma\gamma$, $H \to ZZ^* \to 4l$ and $H \to WW^* \to e\nu\mu\nu$ at a centre of mass energy of 8 TeV and integrated luminosity of $5.8 - 5.9 fb^{-1}$ in p-p collisions. The SM Higgs boson production processes considered for this analysis were the dominant

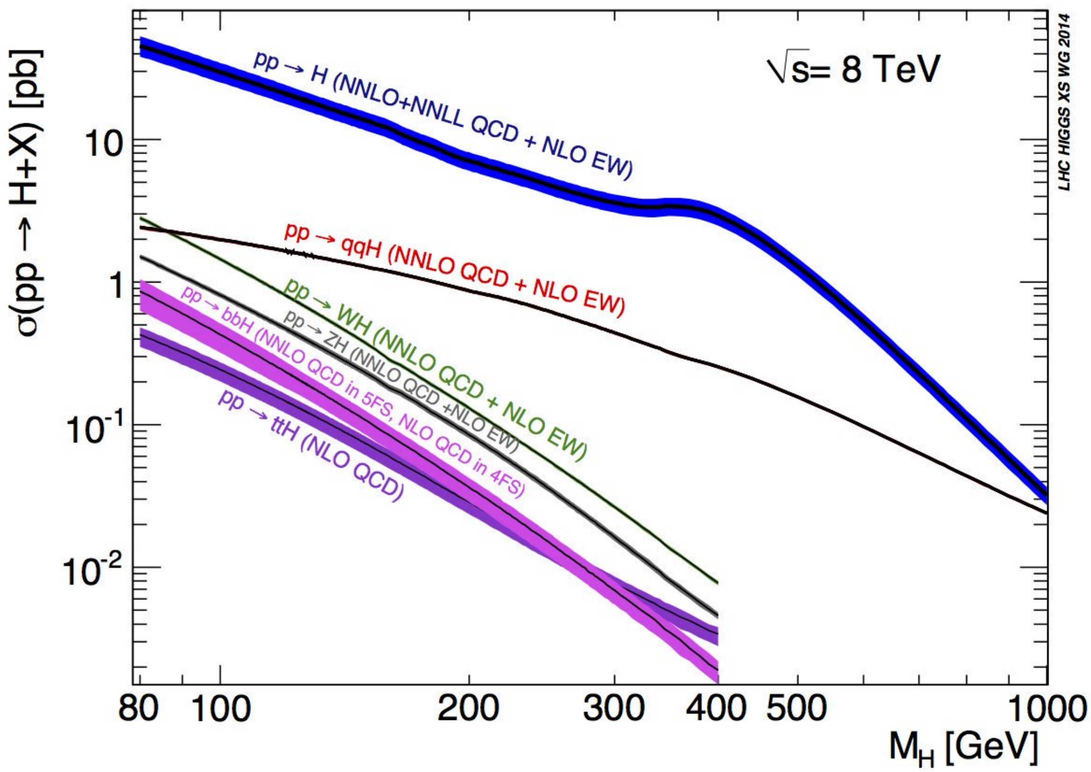

Figure 2.4: Predictions for the probabilities of various decays of the Standard Model Higgs, as a function of the Higgs mass.

gluon fusion $gg \to H$, vector boson fusion $q'q \to q'qH$, and Higgs-Strahlung $q'q \to WH, ZH$. Also a small contribution from $q'q/gg \to t\bar{t}H$ to the $H \to \gamma\gamma$ process was taken into account [46].

The mass of the observed new particle is estimated using the profile likelihood ratio λ for the two channels with the highest mass resolution, $H \to \gamma\gamma$ and$H \to ZZ^* \to 4l$. The resulting estimate for the mass of the observed particle is $M_H = 126.0 \pm 0.4$ (stat) ± 0.4 (sys) GeV with a 5.9σ excess in the confidence level. [4]

By 2013 and 2014, both experiments updated their results for the full 2011

[4]The leading sources of systematic uncertainty come from the electron and photon energy scales and resolutions.

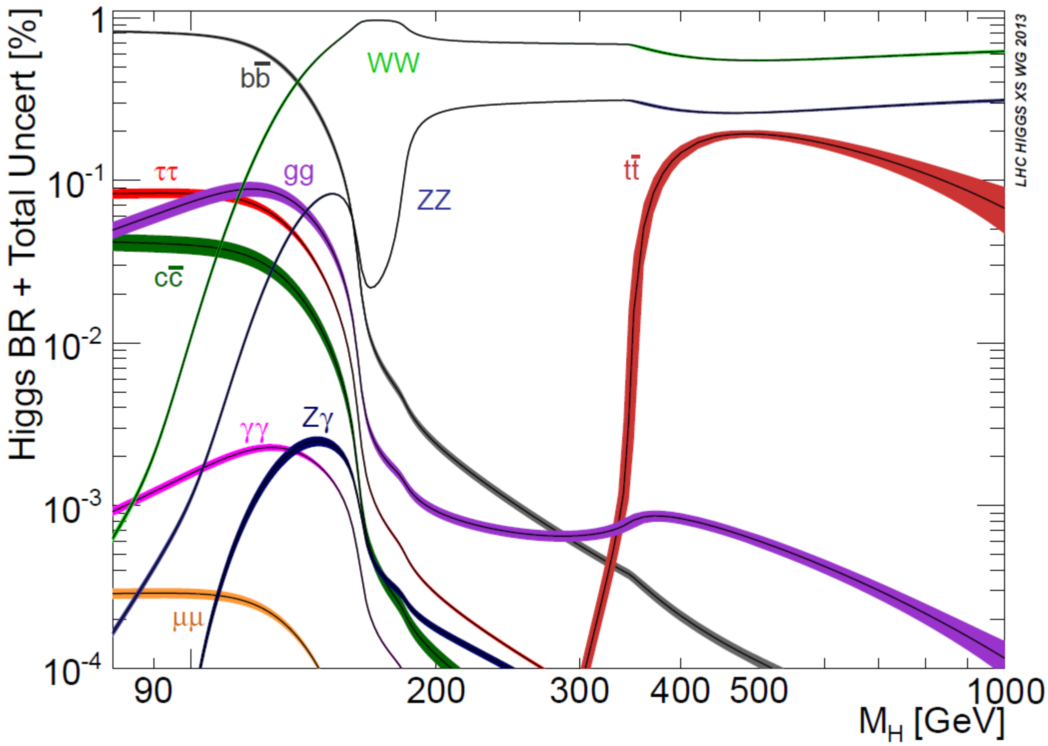

Figure 2.5: Predictions for the probabilities of various decays of the Standard Model Higgs, as a function of the Higgs mass.

and 2012 LHC runs with an integrated luminosity of $4.8 fb^{-1}$ and $20.7 fb^{-1}$ at a centre of mass energy of 7 TeV and 8 TeV, respectively. Unlike previous analyses that found no excess in $H \to \tau^+\tau^-$ and $H \to b\bar{b}$, in the new analysis, the Higgs searches were performed using the five decay channels $H \to \gamma\gamma$, WW, ZZ, $b\bar{b}$, and $\tau^+\tau^-$. The combined mass is measured by the ATLAS and CMS experiments is $M_H = 125.7 \pm 0.3$ (stat) ± 0.3 (sys) GeV [47].

Chapter 3

LUCID and Luminosity Measurement

3.1 Luminosity Overview

In a beam colliding experiment, the instantaneous luminosity, $\mathcal{L}$, is defined as the ratio between the interaction rate of any process, $\frac{dN_{proc}}{dt}$, and its cross-section σ, the probability for a particular process to occur is given as:

$$\mathcal{L} = \frac{\frac{dN_{proc}}{dt}}{\sigma} \tag{3.1}$$

where N_{proc} is the number of events of a given process that took place during the run, during time dt.

An accurate estimation of the luminosity is particularly important for any physics analysis in which a cross-section is measured and it is a key parameter in most physics analyses. The higher the luminosity, the more data the experiments can gather to allow them to observe and study rare processes.

3.1.1 Luminosity Measurements

The absolute luminosity can be obtained from the geometrical and kinematic characteristics of the beams such as the frequency of the beam, the number of particles in the beam, and the overlap integral of the beam. In the case of two Gaussian ideal head-on collisions, if two bunches are containing n_1 and n_2 particles, circulating with a frequency of f_r and the cross-section area is $A = 4\pi\sigma_x\sigma_y$, then the expression for the luminosity is:

$$\mathcal{L} = \frac{n_b n_1 n_2 f_r}{4\pi\sigma_x\sigma_y} \tag{3.2}$$

where σ_x and σ_y are the standard deviation of Gaussian functions describing the beam profile in the horizontal and vertical directions and n_b is the number of colliding bunches at the LHC.

During the experimental run time, it is difficult to use this method or any other method that needs to measure beams properties, as direct measurement of the beam profiles without disturbing the beams is not possible.

In practice, the methods used in ATLAS to monitor the luminosity are sampling the rate of inelastic interactions. The fast detectors, such as LUCID, are able to measure an event rate for each beam crossing; the detectors have to be read every 25 ns which is the temporal bunch spacing at the LHC since 2015. In the case of the LUCID luminometer a dedicated electronics readout board (LUMAT) is used to process the measurements taken during run time and provides integrated as well as bunch-by-bunch luminosity information.

The total luminosity, $\mathcal{L}$, is then obtained by summing over the luminosity of each bunch, $\mathcal{L}_b$.

The number of inelastic p-p interactions that take place when two bunches collide follows Poisson statistics with a mean of μ, which denotes the average number of inelastic interactions per bunch crossing. A particular detector will measure a visible number of interactions, $\mu_{vis} = \epsilon\mu$, that depends on the efficiency and acceptance of the detector to detect a single interaction, ϵ. Therefore, the luminosity as a function of μ and inelastic cross-section, σ_{inel}, can be expressed as:

$$\mathcal{L}_b = \frac{\mu f_r}{\sigma_{inel}} = \frac{\mu_{vis} f_r}{\sigma_{vis}} \tag{3.3}$$

where $\sigma_{vis} = \epsilon\sigma_{inel}$ is the visible cross-section.

Measuring μ_{vis} allows us to monitor the luminosity, since μ_{vis} is an experimentally observable quantity that is proportional to the luminosity. The LUCID luminosity monitor is calibrated by performing an absolute luminosity measurement and a measurement of μ_{vis}, at the same time. ATLAS uses the VDM method [55, 56] to determine the absolute luminosity. In this method, the beams are separated in the horizontal (x) and vertical direction (y) while the interaction rate is measured with a particular algorithm. The basic idea is that the luminosity can be obtained from the width of the two scan curves (Σ_x and Σ_y) if the number of colliding protons in the bunches are also measured. One can show that the maximum luminosity for a colliding bunch pair L_{peak} can be calculated as:

$$\mathcal{L}_{Peak} = \frac{n_b N_1 N_2 f_r}{2\pi\Sigma_x\Sigma_y} \tag{3.4}$$

Here Σ_x and Σ_y are the standard deviation of Gaussian function in the horizontal and vertical directions and n_b is the number of bunches at the LHC.

A luminosity monitor is calibrated by equating equation 3.4 to equation 3.3. This yields:

$$\sigma_{vis} = \mu_{vis}^{MAX} \frac{2\pi\Sigma_x\Sigma_y}{N_1 N_2 f_r} \tag{3.5}$$

where μ_{vis}^{MAX} is the visible interaction rate observed at the peak of the scan curve by the luminosity monitor in question.

Therefore, the efficiency of the luminosity algorithm can be expressed as

$$\epsilon = \frac{\sigma_{vis}}{\sigma_{inel}} \tag{3.6}$$

For instance, during Run-2, the LUCID-2 detector measured the efficiency of LUCID "OR" algorithm, ϵ^{OR} to be 24%. ϵ^{OR} represents the probability of a single p-p interaction to result in a hit in at least one of the LUCID's PMTs on either side. While σ_{vis} for "OR" algorithm is measured to be 32.4 mb and μ_{vis}^{MAX} to be 24.

3.1.2 Luminosity Block (LB)

All the runs in the LHC are segmented into equal time intervals called Lumi Blocks (LBs). This keeps the loss of data to a minimum possible. If the machine, detector or DAQ system fails, the LBs in which failures occur will be excluded from the analysis LBs (good LB).

The minimum value of LB size is chosen such that the statistical uncertainty is less than the systematic error and the upper limit depends on how much data is lost due to the failure in the system is tolerable. Typically, a LB size is in the order of 1 minute.

The LUCID detector provides bunch by bunch, raw luminosity information for each LB, as well as the luminosity over all colliding bunches. Therefore, the average luminosity can be expressed as:

$$\mathcal{L} = \sum_{i=BCID} \mu^i_{vis} \frac{f_r}{\sigma_{vis}} \tag{3.7}$$

where the sum is performed over the colliding BCIDs. Therefore the problem of measuring luminosity can now be factorized into determining σ_{vis} and measuring μ_{vis}.

The value of μ_{vis} is obtained from the raw number of counts and the number of bunch crossings, under the assumptions that all p-p interactions in a bunch crossing are independent.

Event "OR" Algorithm

The Poisson probability for observing zero events in a bunch crossing can be expressed as:

$$P_0(\mu_{vis}) = e^{-\mu_{vis}} = e^{-\mu\epsilon^{OR}} \tag{3.8}$$

where the probability for a single p-p interaction to result in a hit in at least one of the LUCID tubes is denoted by ϵ^{OR}, shows the efficiencies of the "OR" condition. Similarly, Let ϵ^A, ϵ^C, ϵ^{AND} denote the efficiencies of the "ORA", "ORC" and "AND" conditions[5], respectively. Then, the probability of observ-

[5] All conditions are defined in table 3.2

ing at least one event is:

$$P_1^{OR}(\mu_{vis}) = \frac{N^{OR}}{N^{BC}} = 1 - P_0(\mu_{vis}) = 1 - e^{-\mu_{vis}} \tag{3.9}$$

The raw event count N^{OR} is the number of bunch crossing, during a given time which satisfy the event selection criteria of the Event OR algorithm, and N^{BC} is the total number of bunch crossings during the same interval. Then, μ_{vis}^{OR}, in terms of event counting rate yields:

$$\mu_{vis} = -ln(1 - \frac{N^{OR}}{N^{BC}}) \tag{3.10}$$

Similar equations for ORA and ORC events can be expressed as:

$$\begin{aligned} \mu_{vis}^{ORA} &= -ln(1 - \frac{N^{ORA}}{N^{BC}}) \\ \mu_{vis}^{ORC} &= -ln(1 - \frac{N^{ORc}}{N^{BC}}) \end{aligned} \tag{3.11}$$

Event “AND” Algorithm

For the AND condition, the formula is more complicated as the probability depends on three parameters: ϵ^A, ϵ^C, and ϵ^{AND}. These efficiencies are related to the Event OR efficiency by $\epsilon^{OR} = \epsilon^A + \epsilon^C - \epsilon^{AND}$. The probability of having at least one hit on both sides $P^{AND}(\mu)$ is:

$$P^{AND}(\mu) = 1 - P_0^{Zero-OR} \tag{3.12}$$

where $P_0^{Zero-OR}$ is the probability of having no hit at least on one side which can be expressed as :

$$P_0^{Zero-OR} = P_0^A + P_0^C - P_0 \tag{3.13}$$

where $P_0^A = e^{-\mu\epsilon^A}$ is the probability that there be no hit at least on side A, $P_0^C = e^{-\mu\epsilon^C}$ is the probability that there be no hit at least on side C, and $P_0 = e^{-\mu\epsilon^{OR}}$ is the probability that there be no hit on either side. Therefore, the probability of having at least one hit on both side can be determined as follows:

$$\begin{aligned} P^{AND} &= \frac{N^{AND}}{N^{BC}} \\ &= 1 - (e^{-\mu\epsilon^A} + e^{-\mu\epsilon^C} - e^{-\mu\epsilon^{OR}}) \\ &= 1 - (e^{-\mu\epsilon^A} + e^{-\mu\epsilon^C} - e^{-\mu(\epsilon^A + \epsilon^C - \epsilon^{AND})}) \end{aligned} \tag{3.14}$$

The efficiencies ϵ^{AND} and ϵ^{OR} are defined as $\epsilon^{AND} = \sigma_{vis}^{AND}/\sigma_{inel}$ and $\epsilon^{OR} = \sigma_{vis}^{OR}/\sigma_{inel}$. The average number of visible inelastic interactions per BC is computed as $\mu_{vis} = \mu\epsilon^{AND}$. Therefore equation 3.14 becomes:

$$\frac{N^{AND}}{N^{BC}} = 1 - 2e^{-(1+\sigma_{vis}^{OR}/\sigma_{vis}^{AND})\frac{\mu_{vis}}{2}} + e^{-(\sigma_{vis}^{OR}/\sigma_{vis}^{AND})\mu_{vis}} \tag{3.15}$$

There is no analytical solution for μ in the above equation and thus, it can only be solved numerically.

Saturation of the Luminosity Algorithm

Saturation of a luminosity algorithm occurs when almost all bunch crossings give a signal in the detector. Considering equation 3.16:

$$P = 1 - e^{-\mu\epsilon^{OR}} \tag{3.16}$$

when P is the probability to observe bunch crossings with at least one hit in the LUCID detector, μ is the average number of p-p-interactions per bunch crossing and ϵ is the overall efficiency of the detector. P is estimated by counting the fraction of bunch crossings with at least one hit in an LB period.

If the measured fraction is 1 or close to 1 then every bunch crossing has a hit, therefore, it cannot be used to estimate μ. Lowering the overall efficiency of the detector can avoid this saturation problem.

In the next section, the Simulation of the LUCID detector and its efficiency will be presented.

3.1.3 The LUCID Detector

LUCID detects charged particles by means of the Cherenkov light emitted in the quartz window of LUCID's PMTs. Cherenkov light is emitted when a charged particle traverses a material with a velocity larger than the speed of light in the medium ($v > c/n$), where n is the refractive index of the radiator.

LUCID is a dedicated luminosity monitoring detector. The LUCID apparatus consists of two modules installed in the forward region at about ± 17 m from the interaction point of ATLAS. The LUCID detector works based on prompt Cherenkov light, allowing measurements to be made within the bunch spacing of the LHC (25 ns). This allows the LUCID detector to perform precise luminosity measurements bunch by bunch. The LUCID detector design evolved to keep pace with the increasing luminosity of the LHC. So far two versions of the LUCID detector have been designed and installed. We shall only consider the LUCID-2 detector that was installed in 2014.

3.1.4 The LUCID-2 Detector

During the long LHC shutdown between 2013 and 2015, the ATLAS beam-pipe in the LUCID region was upgraded, necessitating the removal of the LUCID-1 detector. At this stage an upgraded LUCID-2 detector was installed. The new beam-pipe was made of aluminum instead of stainless steel and simulations showed that the number of particles hitting the LUCID-2 detector would increase fourfold. Also during Run 2, the LHC machine was expected to provide twice the previous peak instantaneous luminosity. Also, the bunch spacing in the LHC was decreased from 50 ns to 25 ns. The original LUCID design could not cope with the new running conditions, which would lead to saturation of photomultipliers and the luminosity algorithms, as well as problems with the lifetime of the old PMTs. As the acceptance of the photomultiplier was increasing, there would be hits in the detector in almost every bunch crossing. The large acceptance also meant that the PMTs were drawing large currents that would limit their lifetime. Therefore, a new design for the LUCID detector was needed to meet the challenges in 2015 and beyond. The solution to these problems was to build a detector without Cherenkov tubes and a gas radiator and with smaller PMTs with smaller acceptance. This device relied solely on the Cherenkov light generated in the PMT windows, for the detection of charged particles.

In the LUCID-2 design, each module consists of 16 photomultipliers with an additional 4 quartz fibre bundles, effectively forming four small "spaghetti calorimeters". The more compact design with 16 + 16 new smaller 10 mm diameter photomultipliers in 4 groups around the beam-pipe and with 4 bundles of quartz fibres readout by PMTs that were 2 m away from the LUCID-2 detector, inside the muon shielding. To increase the detector lifetime, only a subset of the PMTs is used at a given time, the unused tubes being turned off and available as spares. In addition, the LUCID detector uses 4 PMTs with the reduced window opening to decrease their acceptance and thus avoid saturation of some luminosity algorithms.The 20 R760 Hamamatsu PMTs are grouped in 5 different families shown in table 3.1.

Name	Method/Use	Diameter	Type	# of PMTs
Fiber PMT	Cherenkov light is produced and delivered by quartz fibers bundles.	10 mm	R760 Hamamatsu	4
Bi PMT	Equipped with a ^{207}Bi radioactive	10 mm	R760 Hamamatsu	4
VdM PMTs	Equipped with LED light and used during the VdM scan to determine the absolute luminosity	10 mm	R760 Hamamatsu	4
SPARE PMTs	Turned on if the VdM PMTs have aged too much	10 mm	R760 Hamamatsu	4
MOD PMTs	Equipped with a ^{207}Bi radioactive and a thin ring-shaped layer of aluminium deposited between the quartz window and the photocathode to reduce the acceptance.	7 mm	R760 Hamamatsu	4

Table 3.1: 5 different types of PMTs that are used in the LUCID-2 during 2015 data taking.

We performed Monte Carlo simulations to estimate the acceptance of the new LUCID detector. The LUCID simulation is divided into two steps. The first step is the description of the geometry of the detector in a stand-alone GEANT4 (GEometry ANd Tracking) [57] simulation in ATHENA. The second step is the study of the detector response to particles of a given energy, position and direction. This process is generally divided into three steps itself: 1) event generation; 2) physics and detector response; 3) digitization of physics quantities and producing the final output. The digitization scheme for the LUCID detector is divided into five steps: 1. Unpacking of the simulated hits to a format which can be used in the digitization; 2. Simulation of the PMT response; 3. Formation of detector response digits; 4. Level 1-trigger simulation; 5. Conversion of digits to byte stream format. Finally, the estimation of efficiency and acceptance of the LUCID detector in different algorithms.

3.1.5 Cherenkov Light Emission in LUCID

In LUCID, the minimal velocity at which the emission takes place, c/n, corresponds to a particle energy threshold E_{trsh}:

$$E_{trsh} = \gamma m_0 c^2 = \frac{m_0 c^2}{\sqrt{1 - \frac{1}{n^2}}} \tag{3.17}$$

where m_0 is the rest mass of the particle. In the quartz window of the PMTs, for a pion $E_{trsh} = 190$ MeV and for an electron $E_{trsh} = 0.7$ MeV. The Cherenkov light threshold is emitted along the path of the particle. Figure 3.1 shows the digitized pulse shape of a signal from one of the PMTs of the LUCID detector when a particle enters a tube. The charge carried by a particular signal is measured by integrating over the pulse shape.

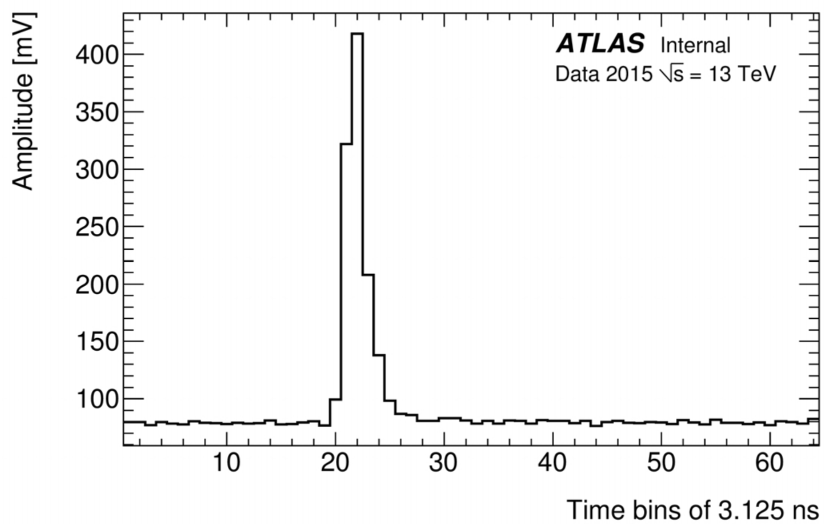

Figure 3.1: Digitized pulse shape of a signal from one of the PMTs in A-arm of the LUCID detector during a 50 ns run in June 2015 at CM energy of 13 TeV. Each time bin represent 3.125 ns long which means the duration of the pulse is less than 25 ns.

Geometry of The LUCID-2 detector

In the first step of the simulation, the main detector elements were described in a stand-alone GEANT4 [57] simulation which is a platform for the simulation of the passage of particles through matter, using Monte Carlo methods. The general layout of the LUCID detector in the simulation is similar to the real detector and all the major parts of the detector are included in the simulation. As this simulation is mostly done for the purpose of finding the acceptance of the LUCID detector, the main elements in the geometry of the LUCID detector are the elements that particles pass through before they reach the PMTs and the surface of the PMTs themselves.

The second step in the simulation chain is to simulate the passage of the generated particles through the different detector elements and their response. Such a description includes a description of both the active material of the detector as well as the passive parts such as support structure and shielding. In this sub-section the, design of the LUCID detector will be discussed and issues in which detector description differs from the simulation design will be addressed here.

In constructing the detector components in GEANT 4, the different geometrical forms and methods are defined in order to produce the solids that will be needed to build a computer model of the detector. The volumes are hierarchical; a volume is placed in its mother volume. The first step in the simulation is to define air volume as the boundary for all the component of the detector in order to separate different detectors. The volume is defined in such a way that it contains only the LUCID detector and does not clash with the neighbour ATLAS detector subsystems once included in the simulation.

The beam-pipe in the region where the LUCID detector is situated is supported by a long cone called VJ cone which is attached at the back to an aluminium plate which attached to a solid shielding cylinder made of cast iron. The VJ cone supporting LUCID-1, was made of aluminium. For LUCID-2 it was decided to change the composition of the cone material to carbon fibres to further reduce background and activation. The VJ cone consists of two 42.5 cm and 22.5 cm long cylinders which are attached by a 4.4 m conical shaped section. The front of the VJ cone is located at 13.4 m from the interaction point. The frontal cylinder has a 5 mm thick wall and an outer diameter of 115 mm. The back cylinder has an outer diameter of 610 mm. On both ends

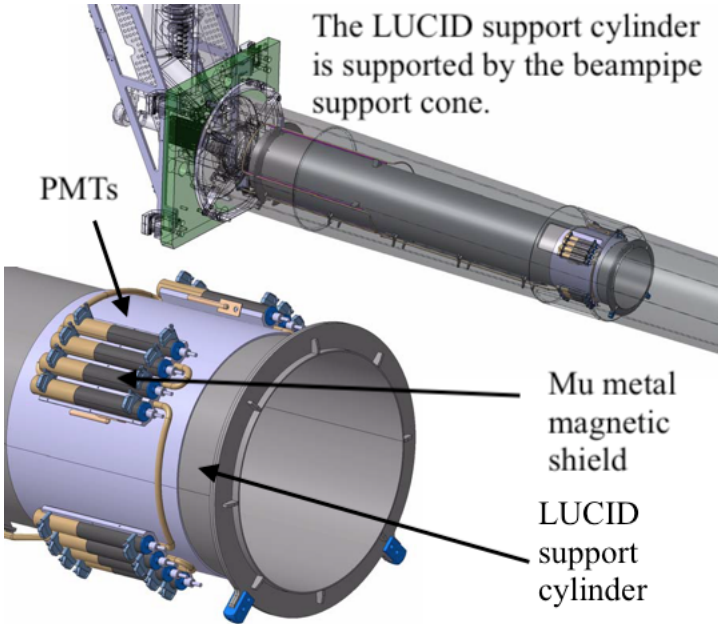

Figure 3.2: Schematic view of LUCID-2 detector.

of the VJ cone, the two aluminum rings that are part of the the support for the beam-pipe are placed at 13352 mm and 18152 mm from the the IP, respectively. Figure 3.4 shows the schematic description of the VJ cone and figure 3.2 shows the real design of the VJ cone.

Inside the VJ cone, there is a 1550 mm long LUCID support cylinder that is made of carbon fibre. The cylinder has a 1.5 mm thick wall and an outer diameter of 223 mm. The LUCID support cylinder is attached to the beam-pipe support cone. In the LUCID design, at the back of the support cylinder, four bundles of optical quartz fibres, housed in aluminium tubes, are attached to copper tubes that carry water to cool the fibres as well as the LUCID PMTs mounted on the PMT support cylinder. This cooling is needed during beam-pipe bake-out. Figure 3.3 shows a full shape and cut-away visualization of the different pieces of the detector description as it is implemented in the

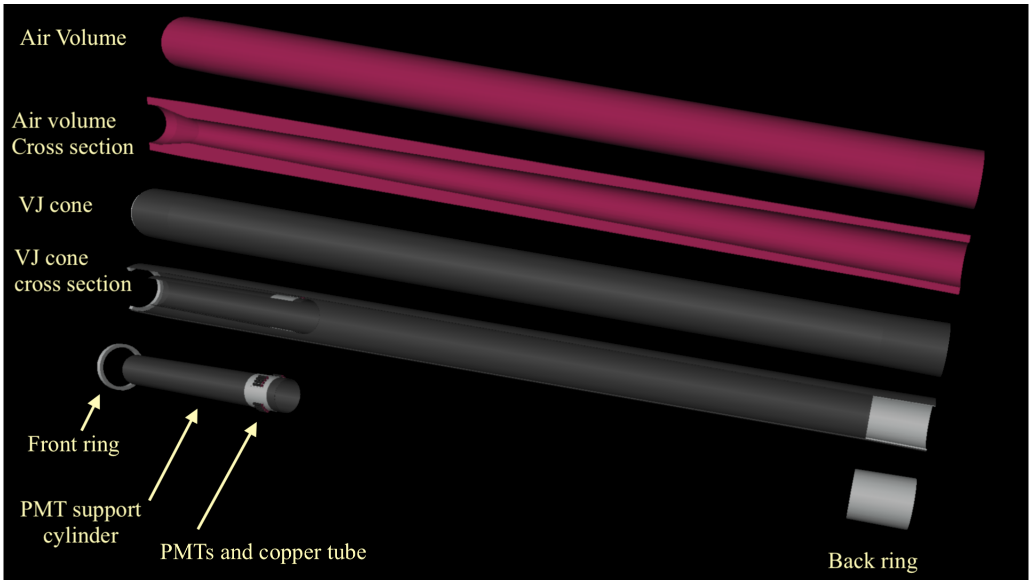

Figure 3.3: Visualization of the layers of the simulated LUCID-2 detector

simulation/GeoModel. The LUCID and ATLAS upgraded geometries that are tagged in this study are LUCID_GeoModel-00-02-01 [53] and ATLAS-R2-2015-02-02-00 [54].

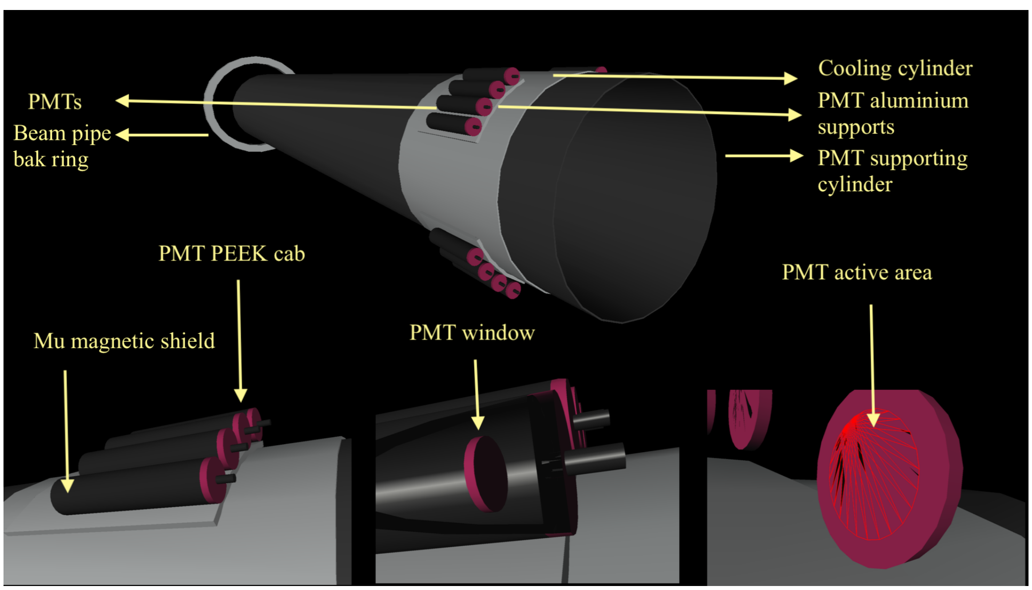

Figure 3.4: Visualization of the PMTs in the simulated LUCID-2 detector

The LUCID-2 luminosity monitor is comprised of 16 PMTs that are attached to four aluminium supports sitting around a 1.5 mm thick cooling cylinder. Figure 3.4 shows the simulation of the PMTs arranged on the PMT supporting cylinder.

The PMT window acts as a Cherenkov radiator. When charged particles cross the window, they produce light which is converted into an electrical signal that is fed into a read-out board (LUCROD) for the measurement of the charge and the digitization of the signal. The PMTs are simulated with a thin quartz disc matching the transverse dimensions of the tubes. The simulation of the PMT window is crucial since it acts as a photon emitter (Cherenkov radiator). The photocathode is simulated by applying the wavelength dependent PMT quantum efficiency of the Hamamatsu R760 [58] to the detection of photons produced when a particle coming from a p-p collision enters a LUCID PMT.

Each PMT is placed inside a mu metal cylinder. This mu metal cylinder has a wall thickness of 0.85 mm and it protects the PMTs from stray magnetic fields. At the front of the PMT and its mu-metal cylinder, a cap made of PEEK is attached which holds a connector for optical quartz fibres in order that the LED light or laser light can be transmitted to the front of the PMT window for calibration purposes. The centre of the PMTs sits at a distance of 125.5 mm from the beam line and 16.97 m away from the interaction point.

Figure 3.5 shows the parameters used to describe the detector geometry of the VJ cone, the two back and front aluminum rings, PMTs and the PEEK caps.

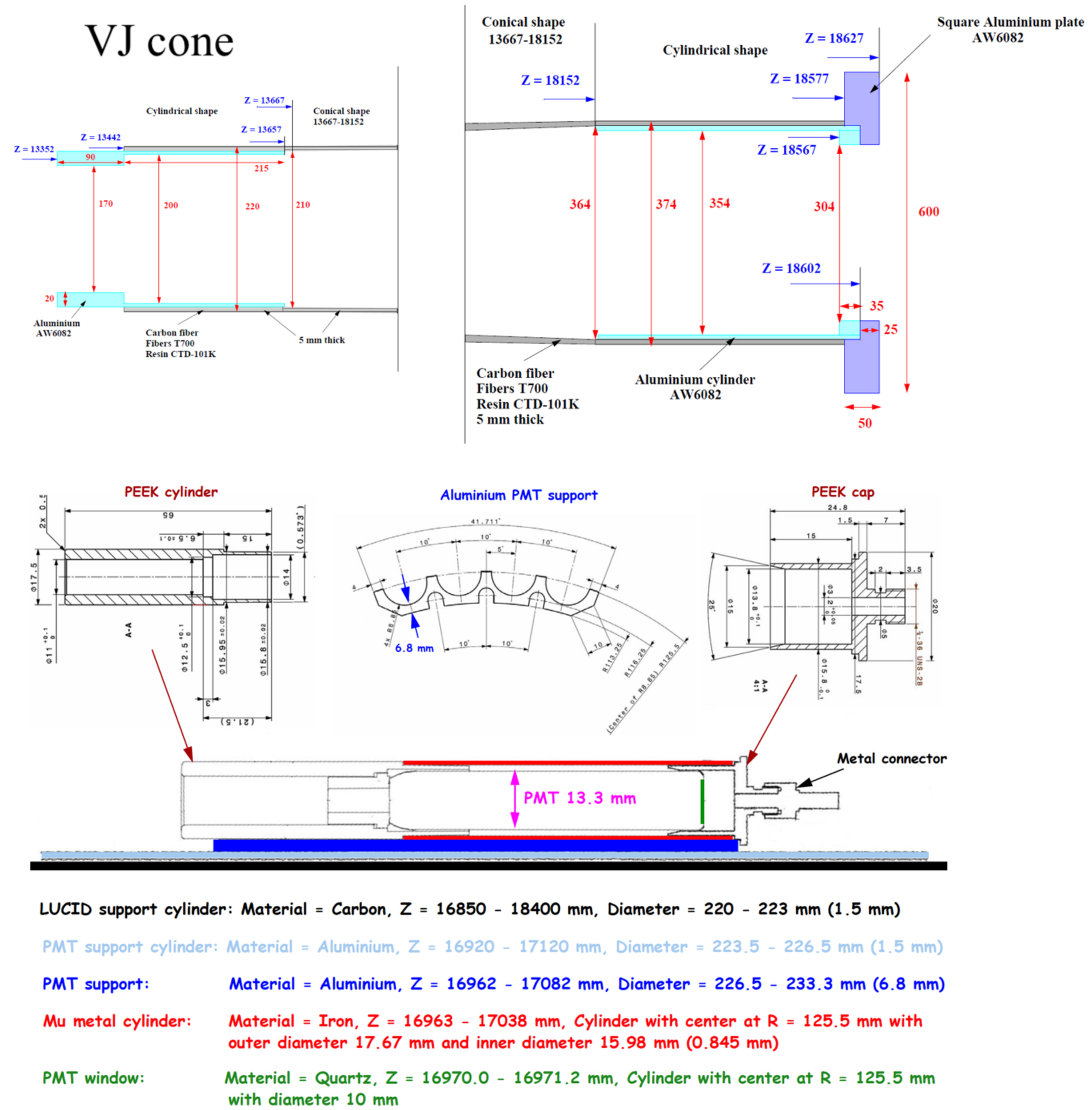

Figure 3.5: Schematic description of the VJ cone, PMT support, muon shield and PEEK cap in the LUCID-2 design

Event Generators

A Monte Carlo event generator program is used to generate simulated high-energy physics events. For inelastic minimum bias events, the most widely used event generator is PYTHIA8 [59]. Inelastic, non-diffractive events are also called "minimum bias" events. In the study presented in the following section, inelastic p-p collisions at the centre of mass energy of 13 and 14 TeV are generated to simulate the production and decay of particles according to our current knowledge of cross-sections and branching ratios. Each event contains particles from a single interaction with vertex at (0,0,0) for single p-p interactions generated with PYTHIA8.

Digitization

After the event generation step, all the final state particles are fed to a GEANT4 simulation of the full ATLAS detector. In order to make the simulation as realistic as possible, all detector modules are included in the simulation. This is especially important for the simulation of signal formation in the LUCID detector since the signal here is dominated by secondaries created in the forward part of the ATLAS detector, close to the beam-pipe and inside the forward muon shielding. In fact, primary particles produced by inelastic p-p collisions, and beam related backgrounds, can interact with the material of the experiments and its surroundings producing secondary particles that may reach the LUCID detector from any direction. In general, the detector simulation step computes particle trajectories, particle-matter interactions and particle decays within the ATLAS detector volume.

The output of simulation is a "Hits" file which stores information about the energy deposits in the detector. The number of photo-electrons generated by Cherenkov photons traversing the sensitive detector is used to characterize the PMT response. The total number of photo-electrons is obtained on a tube-by-tube basis.

Simulation of the front-end electronics is called Digitization. The task of the digitization software is to generate digits for each tube based on the information available from the GEANT4 simulation.The digitization software then converts the energy deposits into detector responses, “digits”, typically voltages or times. The digitization process runs after the GEANT4 simulation and is constructed in such a way that full sets of simulated hits are first to be read in, on an event per event basis. In the LUCID simulation, the sensitive detector is defined as the PMT window.

During the simulation, a hit threshold must be imposed to trigger the readout electronics in order to record the event. The hit threshold is used to trigger the LUCID readout electronics when a single interaction occurs. It must be chosen at a high enough value to filter out beam background events while still low enough to keep the statistics in the calibration runs high. In the LUCID-1 configuration, the hit threshold was set to 15 photo-electron. A similar value has been adopted in the simulation of LUCID-2.

Algorithm	Side A	Side C	Condition	Counting
EventOR	$N_{hits} \geqslant 1$ $N_{hits} = 0$ $N_{hits} \geqslant 1$	$N_{hits} \geqslant 1$ $N_{hits} \geqslant 1$ $N_{hits} = 0$	OR condition	Incremented by one
EventORA	$N_{hits} \geqslant 1$ $N_{hits} \geqslant 1$	$N_{hits} \geqslant 1$ $N_{hits} \geqslant 0$	ORA condition	Incremented by one
EventORC	$N_{hits} \geqslant 1$ $N_{hits} = 0$	$N_{hits} \geqslant 1$ $N_{hits} \geqslant 1$	ORC condition	Incremented by one
EventAnd	$N_{hits} \geqslant 1$	$N_{hits} \geqslant 1$	AND condition	Incremented by one
HitOr	$N_{hits} \geqslant 1$ $N_{hits} = 0$ $N_{hits} \geqslant 1$	$N_{hits} \geqslant 1$ $N_{hits} \geqslant 1$ $N_{hits} = 0$	OR condition	Incremented by the total number of hits
HitAND	$N_{hits} \geqslant 1$	$N_{hits} \geqslant 1$	AND condition	Incremented by the total number of hits

Table 3.2: The six counting algorithms used in LUMAT.

Then the simulated hits, converted into simulated "Raw Data Objects" (RDOs) for input to the reconstruction, are converted into byte-stream data. The byte-stream format for LUCID consists of 2 data words which contain the hit information on a tube-by-tube basis for A and C sides separately. The layout of the byte-stream is the same for simulated data and for real data. This is done to mimic the output from the real detector as closely as possible by letting the same reconstruction algorithm run on both types of data in the same manner. The LUMAT (Luminosity And Trigger) board in the LUCID detector provides the CTP with a trigger based on the hit multiplicity in the LUCID detector. It sends the hit pattern to the ATLAS data flow whenever there is a Level 1 trigger accept, and uses the hit pattern to derive information about the luminosity. The LUMAT board receives one hit pattern per bunch crossing. It scans the part of the hit pattern that corresponds to the standard tubes and checks if any of the four conditions shown in table 3.2 are fulfilled. Bunch crossings that fulfill at least one condition ("ORA", "ORC", "OR", "AND") are called events. Depending on which conditions were fulfilled, LUMAT increments a collection of internal scalers. There are six sets of scalers representing six different counting algorithms. Each set contains one scaler per BCID for a total of 3564 scalers per set. The number stored by the scaler contains information about the luminosity of that BCID. The six algorithms work as shown in table 3.2. In the next section the relation between the numbers stored by the scalers and the luminosity of the LHC will be explained. But for now, we use these numbers to define the efficiency of each of these algorithms.

Let ϵ^{A}, ϵ^{A}, ϵ^{OR} and ϵ^{AND} denote the efficiencies of the ORA, ORC, OR and AND conditions, respectively. In table 3.3, the definition of Hits, Events and efficiencies for all algorithms are shown.

Type of events	
ORA events	events with at least a hit in side A of the LUCID
ORC events	events with at least a hit in side C of the LUCID
OR events	events with at least a hit in side A or side C of the LUCID
AND events	events with at least a hit in side A and side C of the LUCID

Efficiency	
ϵ^{A}	$\frac{\text{Number of ORA events}}{\text{Total number of events}}$
ϵ^{C}	$\frac{\text{Number of ORC events}}{\text{Total number of events}}$
ϵ^{OR}	$\frac{\text{Number of OR events}}{\text{Total number of events}}$
ϵ^{AND}	$\frac{\text{Number of AND events}}{\text{Total number of events}}$

Number of Hits	
$Hits^{A}$	$\frac{\text{Number of hits in ORA events}}{\text{Total number of events}}$
$Hits^{C}$	$\frac{\text{Number of hits in ORC events}}{\text{Total number of events}}$
$Hits^{OR}$	$\frac{\text{Number of hits in OR events}}{\text{Total number of events}}$
$Hits^{AND}$	$\frac{\text{Number of hits in AND events}}{\text{Total number of events}}$

Table 3.3: Definition of Event, Efficiency and Hit for LUCID's different hit algorithms.

In the next step, a simple script is used to translate the byte-stream data in order to calculate the efficiencies. Table 3.4 shows the calculated efficiencies for each algorithm.

The upgraded beam-pipe and the increase in the centre of mass energy of the colliding particles at the LHC resulted in a significant increase of the

	ϵ^A	ϵ^A	ϵ^{OR}	ϵ^{AND}
1	0.387 ± 0.007	0.388 ± 0.007	0.590 ± 0.007	0.185 ± 0.005
2	0.351 ± 0.007	0.347 ± 0.007	0.548 ± 0.007	0.150 ± 0.005
3	0.489 ± 0.007	0.489 ± 0.007	0.693 ± 0.007	0.285 ± 0.005
4	0.3911 ± 0.002	0.389 ± 0.002	0.596 ± 0.002	0.184 ± 0.002

	CM Energy (TeV)	PMT's Diameter (mm)	Active PMTs	Front Ring	Geometry	Beam-pipe	LUCID Geometry Tag	ATLAS Geometry Tag
1	13	10	16×2	✓	New	New	LUCID-GeoModel-00-02-01	ATLAS-R2-2015-02-02-00
2	13	10	16×2	×	New	New	LUCID-GeoModel-00-02-01	ATLAS-R2-2015-02-02-00
3	13	10	16×2	✓	Old	New	LUCID-GeoModel-00-01-20	ATLAS-R2-2015-02-01-00
4	8	14	16×2	✓	Old	Old	LUCID-GeoModel-00-01-19	ATLAS-GEO-16-01-00

Table 3.4: Efficiency of the old and new LUCID detector for 16 active PMTs on each side for different algorithm

LUCID acceptance and efficiency in Run-2. However, the reduced size of the PMT window in the new LUCID design and the new LUCID geometry compensate for this increase.

Another way to reduce the acceptance is to reduce the number of tubes actively measuring the luminosity. Table 3.5 shows the values of the LUCID-2 acceptance for different numbers of tubes.

The table shows that the LUCID acceptance was expected to increase from 60% to 70% from the combined effect of a larger centre of mass energy and an aluminum beam-pipe. However, the new Geometry compensated for that increase. By reducing the number of active PMTs from 16 to 4 on each side of

Threshold	15 photoelectrons
CM Energy	13 TeV
Number of Events	5k
Lucid Geometry Description	New Lucid Geometry LUCID-GeoModel-00-02-01
Beam-pipe	New aluminum beam-pipe with the front ring ATLAS-R2-2015-02-02-00

Number of Active PMTs	ϵ^A	ϵ^A	ϵ^{OR}	ϵ^{AND}
16	0.387 ± 0.007	0.388 ± 0.007	0.590 ± 0.007	0.185 ± 0.005
4	0.158 ± 0.005	0.165 ± 0.005	0.287 ± 0.005	0.037 ± 0.006
1	0.047 ± 0.003	0.046 ± 0.003	0.090 ± 0.004	0.0032 ± 0.0008

Table 3.5: Efficiency of the LUCID-2 in the new ATLAS geometry for different numbers of active PMTs

the LUCID detector, the efficiency will drop by about a factor of 2. Another obvious way to reduce the geometrical acceptance of the detector is to use smaller PMT windows, as was done with the PMT windows already reduced from 14 mm to 10 mm.

As we mentioned previously, LUCID-2 uses the commercial Hamamatsu model R760 with 10 mm diameter. Besides the commercial model, another type of modified PMTs (MOD PMTs) has been produced by Hamamatsu compony which consists of a commercial R760 PMT with one part of the active window aluminized in order to further reduce the effective active area to a diameter of 7 mm. It was decided that 8 out of the 40 PMT's of LUCID-2 should be of this type, in order to fully characterize the performance of these modified (MOD) PMTs during the Run-2 data taking. More details about the choice of PMTs in the design of LUCID-2 detector can be found in [60, 61].

In the table 3.6, it can be seen that with a 10 mm window the acceptance is the same order as LUCID-1, while it becomes smaller by further reducing the size of the PMT window to 7 mm. However, reducing the window size to 7 mm as shown in table 3.6.

Threshold	15 photoelectrons
CM Energy	13 TeV
Number of Events	5k
Lucid Geometry Description	New Lucid Geometry LUCID-GeoModel-00-02-01
Beam-pipe	New aluminum beam-pipe with the front ring ATLAS-R2-2015-02-02-00
Number of Active PMTs	4 on each side

PMT Window Diameter	ϵ^{A}	ϵ^{A}	ϵ^{OR}	ϵ^{AND}
10 cm	0.158 ± 0.005	0.165 ± 0.005	0.287 ± 0.005	0.037 ± 0.006
7 cm	0.122 ± 0.005	0.120 ± 0.005	0.220 ± 0.006	0.022 ± 0.002

Table 3.6: Efficiency of the new LUCID with regular and modified PMTs

Studies of LUCID-1 detector showed for μ values of about 50, the statistical error of the luminosity becomes too large if the efficiency is higher than 20% [61] due to the migration effect. The Monte Carlo simulation in this section indicates that for the LUCID-2 detector, reducing the diameter of the PMTS and lowering the number of active PMTs on each side gives efficiencies below 22%.

3.1.6 Study of main systematic effects on LUCID's luminosity determination in the 2015 Runs

PMT Gain

The measured luminosity depends on the PMT gain but the exact relationship between the luminosity and the gain is not obvious. Because the gain of the PMTs in the LUCID detector decreases during the data taking periods, frequent calibration runs using LED signals are carried out using optical fibres and radioactive ^{207}Bi sources at least once between LHC fills in 2015.

Small pulses of LED light are used to calibrate the PMTs. When the LED light hits the photocathode of a PMT, each photon then excites a photoelectron from the photocathode with a probability given by the quantum efficiency of the PMT. The LED signals provide peaks in the amplitude and charge distributions that are recorded by the LUCID detector in data acquisition runs between LHC fills, when there are no collisions. The stability of the PMT gain is controlled by measuring and maintaining the mean value of charge distributions, obtained from the LED calibration. During Run-2 the high voltage was regularly changed to keep the PMT gain constant, as is the case during the VdM scan.

To use LED sources as a reference for the PMT gain monitoring system, the intensity of the light delivered to the PMT needs to stay constant over a long period of time. The stability of the LEDs is controlled by PIN-diodes that are located in front of the LED lights. Therefore, it is necessary to make sure the light is always stable and the condition of the optical fibres which deliver light to the PMTs stays the same. Nevertheless, we do have issues with the stability of the LED calibration. A better alternative is the use of a radioactive source placed on the PMT window. It was decided to use a ^{207}Bi source because it provides 1 MeV mono-energetic electrons from an internal conversion process with energies above the Cherenkov threshold in quartz.

In order to use ^{207}Bi to monitor the PMT gain, the radioactive source needs to be put close to the PMT. to obviate the need for a bulky source mounting in front of the quartz windows, liquid ^{207}Bi sources were used, with one drop of source material placed on the quartz windows of the PMTs to be calibrated in this way. In order to prevent contamination by the source, a special PEEK cap was glued on top of the PMT. More detailed information about the calibration of the LUCID PMTs can be found in [61].

Monte Carlo simulations of the LUCID-1 detector showed that a certain relative change in gain resulted in a much smaller relative change of the luminosity and the same has been observed for the LUCID-2 detector. Comparisons of the gain decrease measured by the ^{207}Bi sources and the LED system showed that the latter system was overestimating the gain decrease. The reason for this is not clear. The LED system is more complicated and it has components such as optical filters and fibres that could suffer performance degradation from radiation damage. There is also a difference in wavelength between the LED light and the blue and ultraviolet Cherenkov light produced by the ^{207}Bi sources. During data taking in 2015, we kept track of the charge distribution of all PMTs[6]. Figure 3.6 shows the mean charge distribution of Bi PMTs during 2015 runs. Stability of the average ratio of mean charge to the first run for both sides of the LUCID detector is better than 10%. Figure

[6]The distribution of the charge registered by the PMTs

3.7 shows the mean charge percentage of VDM PMTs that use LED light for calibration. The LED calibration used the single photo-electron peak to give an accurate gain measurement that worked well at lower luminosity, but at high luminosity the measurement was spoiled because of background from the activation of the materials surrounding LUCID. By early 2016, all the PMTs in the LUCID detector had Bi sources.

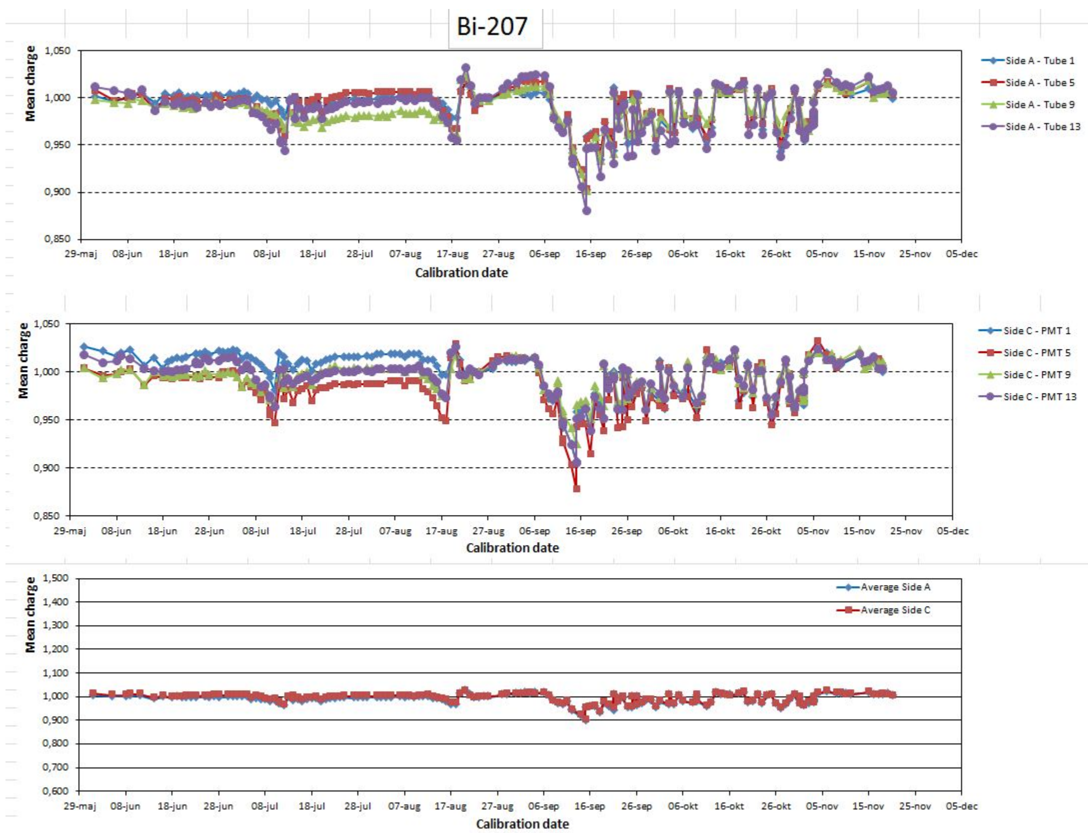

Figure 3.6: Variation of the mean charge percentage of individual and average Bi PMTs on each side during 2015 runs.

The offline analysis was performed regularly to monitor the gain loss of the PMTs which most of the time showed gradual changes giving us enough time to occasionally increase the high voltage. However, in some RUNs in 2015

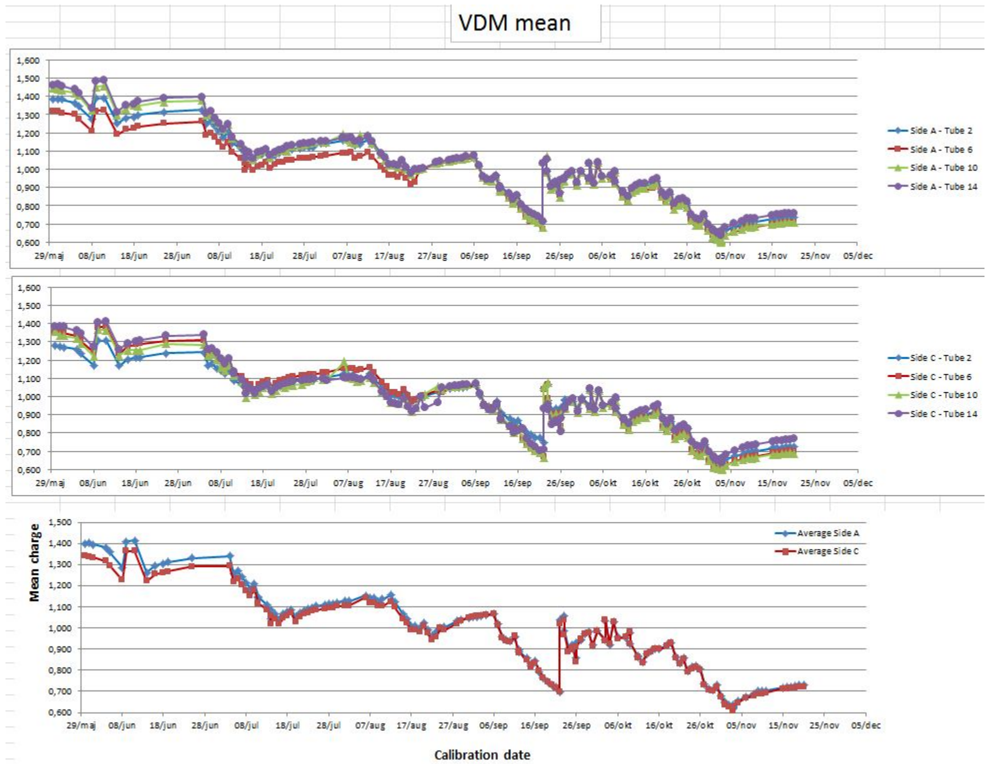

Figure 3.7: Variation of the mean charge percentage of individual and average VDM PMTs on each side during 2015 runs.

there were sharp increases in the luminosity which resulted in a fast decrease of the PMT gains. As the analysis procedure was too slow to correct the high voltage, an automatic script was introduced in 2016 to determine the mean charge of each PMTs after each calibration run which was then used to immediately correct the high voltage supplying the PMTs.

During the 2015 running period, the high voltage was increased by as much as 100 V for some PMTs. The increase of high voltage significantly changed the transit time in the PMTs (up to 6 ns). The measurement system to evaluate the transit time spread of an MCP-PMT is explained in [58]. This led to a part of the signal moving outside of the timing window where it was not recorded, this in turn led to a decreasing efficiency of the detector. During this time, before we discovered the source of the problem, luminosity measured by LUCID was consequently underestimated.

The overall transit time effect was larger for the $LUCID\_BI\_OR\_C$ algorithm (the event "ORC" algorithm for Bi PMTs) measurement than for the $LUCID\_BI\_OR\_A$ algorithm (the event "ORA" algorithm for Bi PMTs) measurement and so the latter algorithm was used for the luminosity measurements in 2015. The blue points in the bottom plot in figure 3.8 show the ratio of the $LUCID\_BI\_OR\_A$ luminosity to the TRACK (Inner detector track counting) luminosity during the 2015 run time.

The transit time problem was different for different PMTs, however, one Bi PMT called BI_C9 was hardly affected. Therefore, BI_C9 was used to derive a transit-time correction for the other PMTs [7]. This correction improved the consistency of the LUCID luminosity measurement compared with those made with the other ATLAS detectors, as shown in figure Fig3-15-Transit-time-correctioin.

Run by run discrepancy

Beside the LUCID detector, there are other sub-detectors that can provide luminosity measurements. The main approach used by ATLAS to investigate systematic effects is to compare measurements of several luminosity detectors which use different algorithms to measure the luminosity. Different detectors have different acceptance coverage, sensitivity, and contribute different sys-

[7] The ratio of $LUCID\_BI\_OR\_A$ to BI_C9 was plotted as a function of the high voltage and a straight line was fitted to the data and used to obtain a correction factor for individual runs.

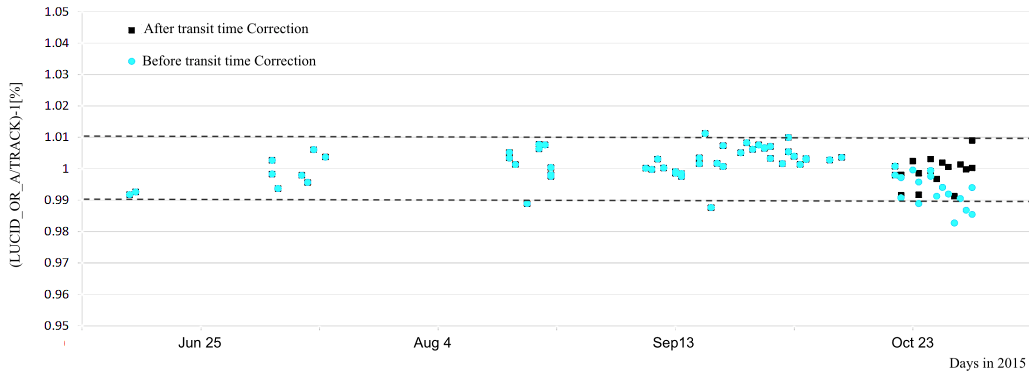

Figure 3.8: Ratio of the measured luminosity per run between *LUCID_BI_OR_A* and TRACK algorithms before and after applying Transit time correction, in 2015 runs.

tematic errors to the measurement of luminosity. Table 3.7 summarizes the properties of other luminosity monitor detectors.

Name	pseudorapidity range	Method	BCID
Tile calorimeter	$\eta < 1.7$	Estimate Particle flux by measuring the current drawn by PMTs	$\times$
EMEC	$1.375 < \lvert\eta\rvert < 3.2$	Estimate particle flux by measuring High voltage drop	$\times$
FCAL	$3.2 < \lvert\eta\rvert < 4.9$	Similar to EMEC	$\times$
Inner detector (TRACK)	$\lvert\eta\rvert < 2.5$	The luminosity is measured by counting the number of reconstructed tracks.	$\checkmark$
Minimum Bias Trigger Scintillators (MBTS)	$2.09 < \lvert\eta\rvert < 3.84$	A scintillator detector designed specially for low luminosity runs	$\times$
The Beam Condition Monitor (BCM)	about 4.2	Four small diamond sensors on each side perform hit counting and provide luminosity in 2015 data taking	$\checkmark$

Table 3.7: ATLAS sub-detectors, beside the LUCID detector, that provide Luminosity for ATLAS.

By comparing the luminosity run-by-run as a function of the time, it is possible to estimate the effect of several systematic problems such as PMT gain change, transit time drift, train dependency and μ dependency.

In 2015, The BCM was the main detector used for studying the systematic errors of the LUCID detector as the BCM can also measure luminosity for individual colliding bunches. In 2015, we discovered that when the LHC employs bunch trains [8], the BCM underestimates the measured luminosity. However, in the VdM scan and runs with isolated bunches, the BCM is still a reliable bunch-by-bunch luminosity monitor. Figure 3.9 shows the ratio of the $LUCID\_BI\_OR\_A$ luminosity to that of two BCM measurements, as well as to the TRACK luminosity and $LUCID\_BI\_OR\_C$. In this figure, the BCM and LUCID luminosities were normalized to the TRACK luminosity in a VdM run. The four different measurements are in good agreement with each other.

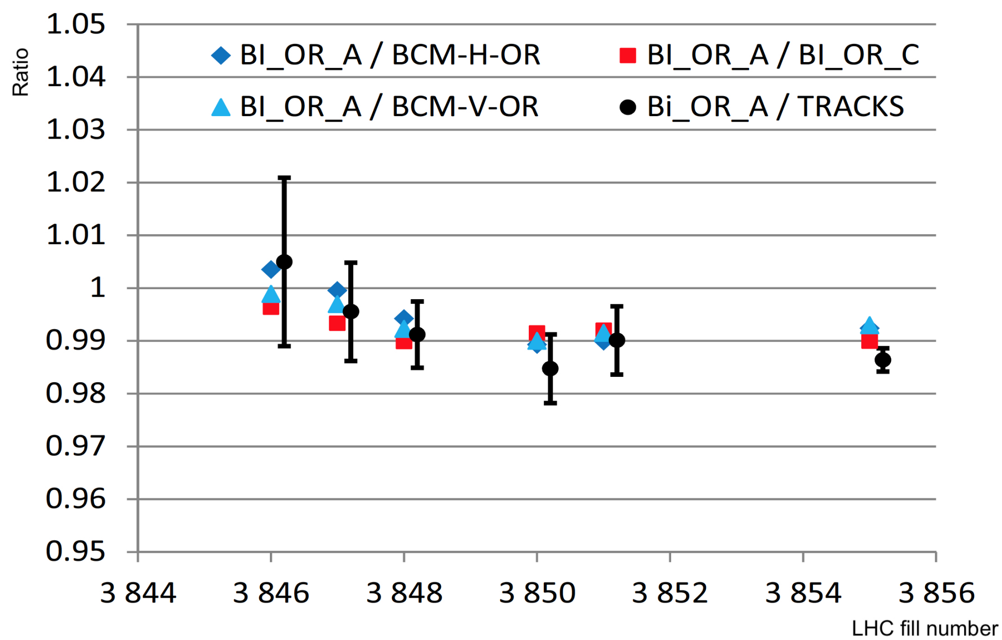

Figure 3.9: The ratio of the $LUCID\_BI\_OR\_A$ luminosity to that of two BCM measurements as well as to TRACK and $LUCID\_BI\_OR\_C$ in 6 LHC fills which are taken in low luminosity and with a small number of isolated colliding bunches.

Figure 3.10 (top) shows the run-to-run comparison of stability of measure-

[8]When more than two consecutive BCIDs are filled in a beam, it is called bunch train.

ments from the TRACK, Tile calorimeter and EMEC detector with respect to the $LUCID\_BI\_OR\_A$ luminosity which was the official luminosity algorithm in ATLAS, for 2015. The relative variations in measurements of all ATLAS luminosities are within ±1.2% and the root mean square of the data points is 0.5% for the Tile calorimeter and 0.6% for the EMEC and the TRACK in 2015.

Figure 3.10 (bottom) shows the ratio of the $LUCID\_BI\_OR\_A$ luminosity to average luminosity determined by the other three detectors. The variations in the luminosity measurements lie within ±1% and the root mean square of the data points is 0.5%.

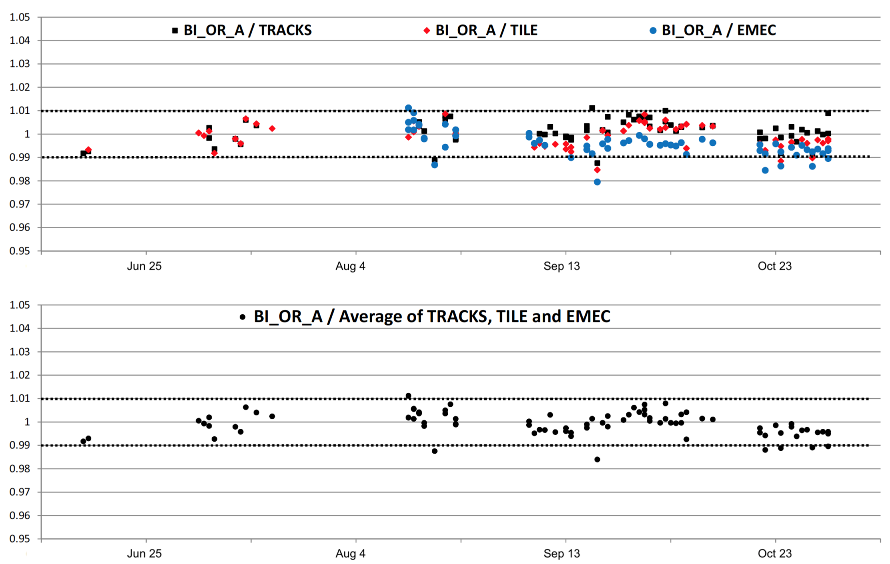

Figure 3.10: (Top plot) Ratio of the measured luminosity of $LUCID\_BI\_OR\_A$ and the Tile calorimeter, EMEC, and TRACK luminosity algorithms per run in 2015. (Bottom plot) Ratio of the measured luminosity of $LUCID\_BI\_OR\_A$ and the average of the Tile calorimeter, EMEC and TRACK luminosity algorithms.

Bunch train dependence

A large effort was made when designing the new LUCID detector and electronics to keep the length of the PMT pulses shorter than the minimum bunch separation of 25 ns. If the pulses are too long they can pile-up in fills with long bunch trains so that the measured luminosity becomes larger for the bunches inside the train compared to the first bunch in the train. This is called the bunch train effect. In 2015 the filling scheme was constantly changing. The 25 ns running started with 2 trains containing 12 colliding bunches and ended with 62 trains with 36 colliding bunches, with many other configurations in between.

Figure 3.11 shows this problem, that was noticed in the 25 ns runs. For the isolated bunches and first BCID in the train, the difference between the ratio of the LUCID and BCM measurements is less than 3% and for any other BCID in the middle of the train, the difference is more than 15%. This due to the fact that the BCM has a very large train dependency that causes a $3-4\%$ shift during 50 ns running and a $15-25\%$ shift during 25 ns running and it is therefore not possible to use the BCM detector to study the LUCID train dependency.

In 2016, the inner detector became available to study the bunch train effect. Figure 3.12 shows the ratio of the luminosity measured by the tracking detector (TRACK) to that measured by LUCID for a selection of runs that were taken close to the VdM scan with which the luminometer was calibrated. The data was normalized so that the ratio becomes one in the VdM run. The ratio has been calculated separately for the first bunches in trains or isolated

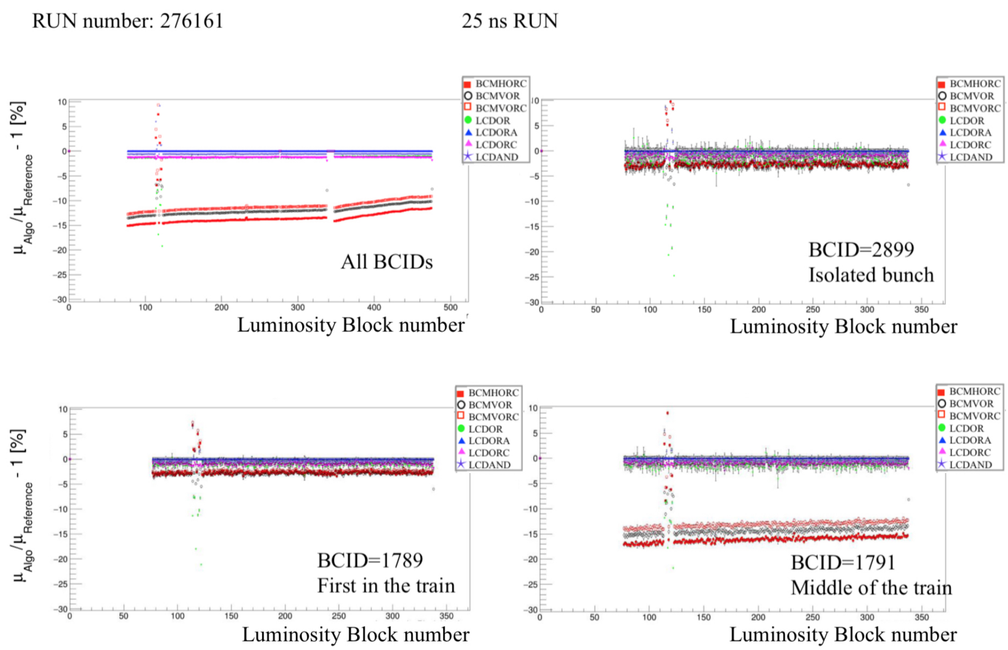

Figure 3.11: The percentage ratio of μ measured by in different algorithm of the LUCID and BCM with respect to $LUCID\_BI\_OR\_A$ in an early 25 ns run. The big difference between LUCID and BCM are coming from the measured μ in bunches in the middle of the train. The isolated bunches and the first BCID in the train are not affected by the train effect.

bunches and for bunches inside the trains. A difference of about 1% is seen between the two selections. With only two detectors available for this study it is impossible to determine if the difference between the LUCID measurement and the TRACK is due to the LUCID detector or the Inner detector.

μ Dependancy

The logarithmic formula used to calculate the event counting luminosity is derived under the assumption that all p-p interactions in a bunch crossing are independent. In other words, we assume that the probability for a given p-p

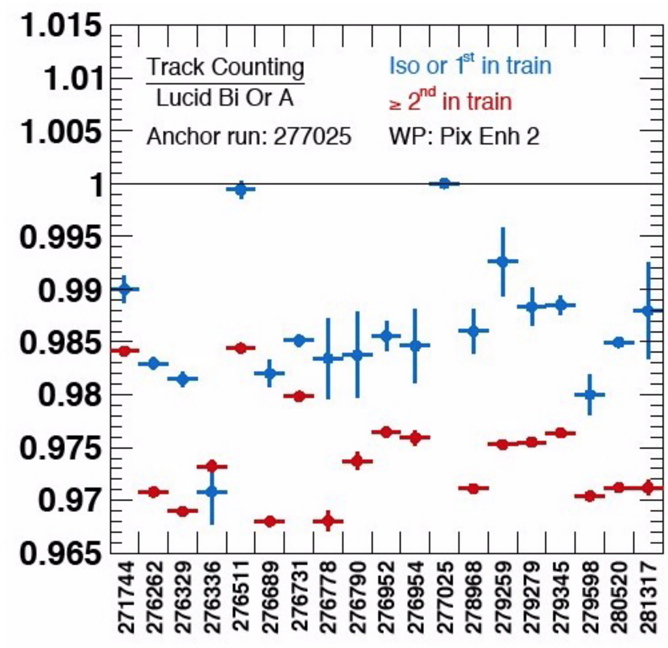

Figure 3.12: The ratio of the luminosity measured by TRACK to that of $LUCID\_OR\_A$ for the first bunches in the trains or isolated bunches and for bunches inside the trains to study the train effect in the LUCID detector.

interaction to cause a hit in the LUCID detector does not depend on the total number of p-p interactions in that bunch crossing. This assumption is not perfectly true for high μ values.

In the gas filled LUCID-1 detector, the signals from several particles crossing the gas volume at large angles could add up to produce a signal above threshold. This migration problem was reduced but not eliminated when the gas vessels were removed. The migration of signals in high μ runs contributes to the μ dependency of the LUCID detector measurements.

The μ dependancy of the LUCID detector was first studied by comparing the μ measurement of the LUCID with the BCM and the Tile calorimeter. Figure 3.13 compares the μ measurement of different algorithms of the LUCID to the two algorithms of the BCM and the Tile algorithms, in one of the mu scans in 2015 with 25 ns bunch spacing. The range of μ varies from 0 to 17. For $\mu < 5$, all the algorithms of the three detectors are in agreement. Points related to the BCM measurements are separated from the LUCID and Tile measurements for $\mu > 5$. The difference between the LUCID measurements and the Tile starts to show up for $\mu > 12$.

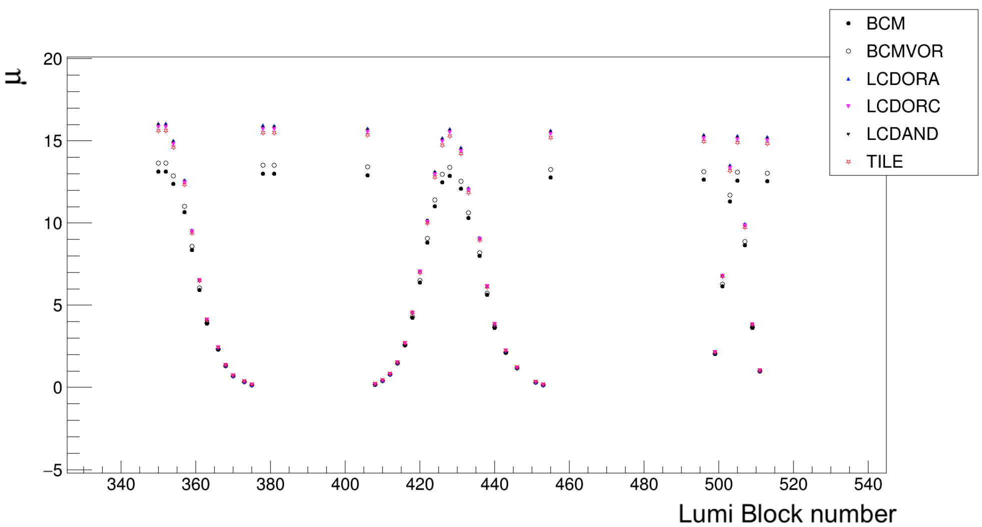

Figure 3.13: μ measurement by Different algorithm of the LUCID, BCM and Tile calorimeter in a μ scan.

Figure 3.14 shows the ratio of the average number of p-p interactions per bunch crossing measured by the Tile Calorimeter to that of $LUCID\_BI\_OR\_A$ as a function of μ. The data samples were normalized such that they give the same luminosity in the VdM fill. The LUCID-2 algorithms are μ-dependent for both the 50 and 25 ns runs. In all 25 ns runs similar decreases are observed. It means μ measurements using the $LUCID\_BI\_OR\_A$ algorithm increase by about 0.2% per unit of μ. In the case of the 50 ns curve, it is flatter and more consistent. The μ measurement with $LUCID\_BI\_OR\_A$ algorithm increase by about 0.1% per unit of μ .

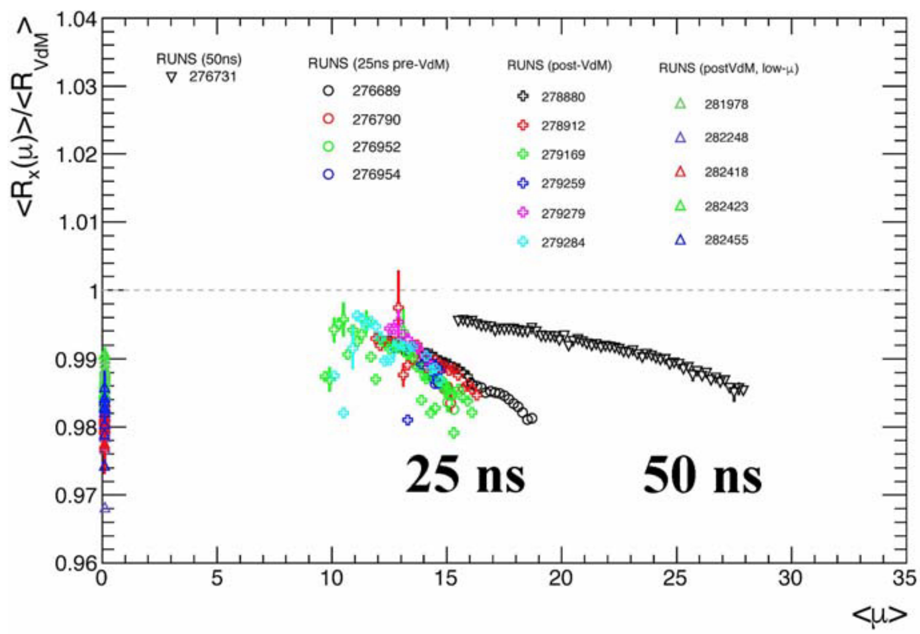

Figure 3.14: The ratio of the average μ measured by Tile calorimeter to that of $LUCID\_BI\_OR\_A$ as a function of the average μ in 25 and 50 ns runs.

The data taken by the LUCID detector could then be corrected LB by LB. However, because different runs have a different average number of p-p interactions or μ, the μ dependency in LUCID could be different from run to run. This is taken into account in the systematic error obtained from the measurement of the run to run fluctuations which is described in the previous section.

All the luminometers in ATLAS are calibrated in the low μ VdM scans. However, due to the μ dependancy of the LUCID, the calibrations obtained in the VdM scans had to be corrected before being used to calculate the luminosity in the physics runs with high μ luminosity, otherwise the detector will systematically overestimate the luminosity. This correction was called a calibration transfer correction because it transferred the calibration obtained in low μ runs with a small number of isolated colliding bunches to high μ runs with bunch trains.The errors due to the calibration transfer correction for the 25 ns running period is determined to be 0.9% by comparing the LUCID data with the TRACK and Tile calorimeter. However, the largest systematic errors in the LUCID luminosity measurement comes from the error in the determination of σ_{vis} which is 1.7%. The long term run-to-run stability has the second most contribution which is estimated to be 1% (see section “Run by run discrepancy”). The total luminosity error of LUCID is obtained by adding these errors in quadrature under the reasonable assumption that they are not correlated and so the total luminosity error of LUCID in the 25 ns data taking period in 2015 is 2.1%.

Chapter 4

ATLAS Forward Proton Tagging Detector (AFP)

4.1 AFP Detector and Forward Physics

The ATLAS Forward Proton (AFP) project [64, 65] will extend the physics reach of ATLAS [103], by enabling the identification of protons that emerge intact from the LHC proton-proton collisions at small angle to the beam direction. Such processes are typically associated with: elastic and diffractive scattering, where the proton radiates a virtual colour-less object (pomeron); and, two photon processes involving quasi-real photons associated with the charged beams.

The prime process of interest for AFP is Central Exclusive Production (CEP) in which the diffracted protons in the final state emerge intact and can be tagged by the AFP detectors. CEP is also recognized by the observation of the central particle such as W or Z boson, a pair of jets, or a neutral Higgs boson allows for a direct determination of its quantum numbers, since to a good approximation only central systems with spin-parity $J^P = 0^+$ [104] can be produced in this manner. Furthermore, tagging both protons allow the mass of the centrally produced system to be reconstructed with a resolution between 3 GeV and 6 Gev per event when both protons are tagged.

AFP consists of four stations, two on each side of ATLAS along the beam-pipe in the forward region. The stations are located at ± 205 m and ± 217 m from the ATLAS interaction point on each side. In each station, there is a Roman Pot which allows the horizontal movement of the detector to move to a few millimetres from the beam. Inside each Roman Pot, there is a tracking system based on 3D silicon pixel sensors [71, 72] which is used to determine the deflection of the protons - and hence their energy loss - in CEP events. The Roman Pots in the far stations also house a Time of Flight (ToF) detector. The ToF t system is essential to reduce background from multiple proton-proton collisions when running at high-luminosity.

4.1.1 The AFP Layout

The three main component of the AFP detector are the Roman Pot (RP), tracking detector, and ToF detector which will be discussed in more detail below.

Roman Pot

In order to tag protons that are deflected slightly from the beam-line without interfering with the primary vacuum of the LHC beam one requires a Roman

Pot device [76].The Roman pot technique has been successfully tested at the LHC and elsewhere. It has been used in both the ATLAS ALFA detector [69] and the CMS TOTEM experiment [13]. TOTEM's cylindrical pot design was copied for the AFP pot with only small modifications.

The cylindrical pots orientation and its motion are horizontal, transverse to the beam direction. In normal operation, the pots internal volume, that houses the detectors, is kept in a 'secondary' vacuum. However, the secondary vacuum may need to be broken for installation or replacement of detectors and components. Moreover, a variety of accident scenarios must be foreseen: the accidental loss of the secondary vacuum being the most likely. Loss of beam vacuum, while the secondary vacuum inside the pot is maintained, is an example of a very rare accident scenario. The catastrophic loss of vacuum, of the secondary or of the beam vacuum, is extremely unlikely. Therefore, the pressure differential to be considered is at most 1 atmosphere. Figure 4.1 (a) shows a Roman Pot and the placement of the detectors inside the far Roman pot.

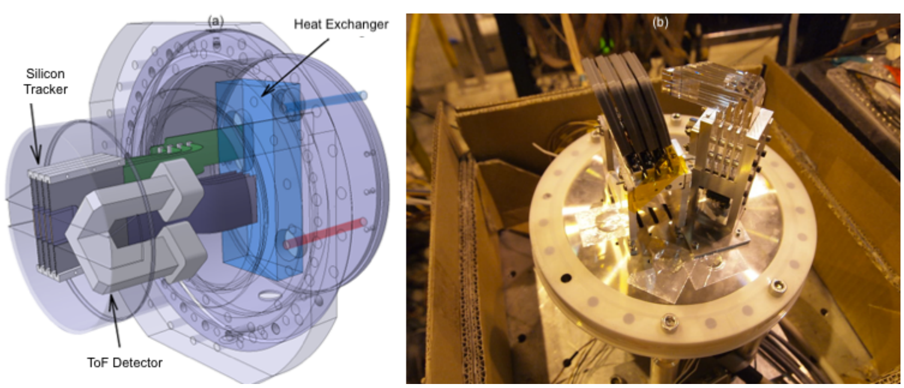

Figure 4.1: (Left) Schematic view of Roman Pot and shows the position of ToF detector and the silicon tracker detector. (Right) Shows the prototype of the ToF detector and the silicon tracker installed inside the Roman Pot.

The pot has a cylindrical shape and guided by a sliding mechanism with a stepping motor to move precisely along the sliding guide and get as close as a few millimetres to the beam. The schematic diagram in figure 4.2 shows the movement of Roman pot with respect to the beam.

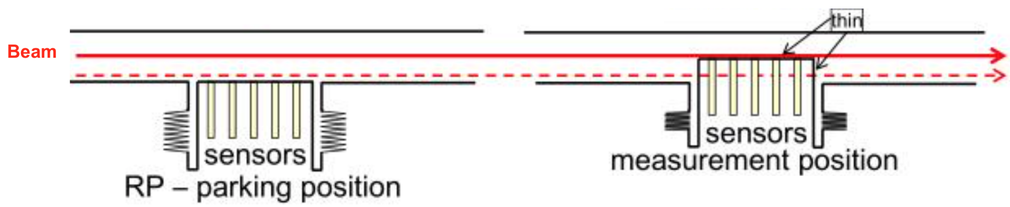

Figure 4.2: A vacuum chamber which houses the detectors is attached to the beam-pipe by means of bellows and the deformation on the bellows bring the detectors as close as possible to the beam line.

4.1.2 Silicon Tracking Detector

The key component of the AFP detector is the silicon tracker system. Its purpose is to track the protons hits that are deflected at small angles during proton-proton collisions. The LHC dipole and quadrupole magnets, guide the protons towards the AFP detector in the forward direction. By determining the proton's trajectory through the silicon tracker allowing the measurement of the proton's deflection angle and energy loss.

Experimentally, there are three main variables which characterize the Central Exclusive Diffractive(CED) events (see also chapter 6): the fractional momentum loss of the two intact protons, and its transverse momentum. The proton fractional energy loss is given by $\xi_{1,2} = 1 - \frac{E_{proton1,2}}{E_{beam}}$, where $E_{proton1,2}$ is the first or second deflected proton energy and E_{beam} is the nominal LHC beam energy. The four-momentum transfer squared can be determined as:

$$\sqrt{-t} = 2E_{proton}E_{beam}sin\frac{\theta}{2}, \tag{4.1}$$

where θ is the deflection angel of the proton.

The missing mass of the central system, which only depends on the fractional momentum loss of the protons ξ_1 and ξ_2, is given as:

$$M_{central} = \sqrt{s\xi_1\xi_2} \tag{4.2}$$

AFP provides a $5 - 10$ GeV per event mass resolution. The energy loss of the proton is determined from the trajectory of the proton as measured by the tracking detectors in the Roman Pots together with the LHC magnets.

In order to measure a very small deflection angle of protons with angular resolution of about 1 μrad, a very special detector with high spatial resolution of 10(30) μm per detector station in $x(y)$ direction is needed. The AFP detectors must also be able to operate in the high background environment near to the beam-pipe in the forward regions. FLUKA simulations were used to predict doses and fluences for the LHC [73]. At a few centimetres from the beam, the dose and fluences integrated over $100fb^{-1}$ of LHC luminosity are 200 Gy, 5×10^{11} neutron equivalent per cm^2, and 10^{11} high energy hadrons per cm^2. These simulations were for $\beta = 0.55$ m optics and included beam-beam interactions only. The measured values approximately confirm the predictions from the simulations. In addition to all these requirements, as the detector should get as close as possible to the beam line, the inactive edge region of the detector should be as small as possible in order to maximize the light mass acceptance. Therefore, 3D silicon pixel detectors were chosen for the purpose of tracking proton at the AFP[9]. The inactive edge of AFP's 3D tracking sensors has been engineered to be as small as $100 - 150$ μm [65].

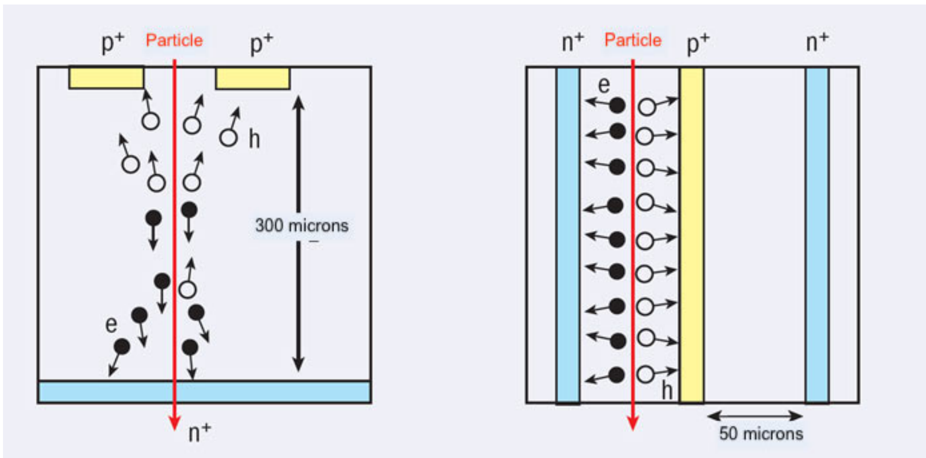

Figure 4.3: Schematic cross-sections of (left) a planar sensor design and (right) a 3D sensor, showing the charge collection in the two designs.

The 3D pixel detector is a new generation of silicon detectors. Figure 4.3 shows the schematic structure of a 3D pixel detector, compared with the traditional planar design. In the production of this type of detector, a new etching technology has been used that allows an array of n- and p-type electrode columns passing through the silicon substrate rather than being implanted on its surface. n^+ and p^+ electrodes are developed in these holes. The diameter of electrodes is 10 μ m, spaced at 20 μm to a depth of less than 285 μm on the surface of the silicon wafer of the sensors. There are several advantages for this structure over the regular planer pixel detectors, which are used in the inner detector of the ATLAS. First, the smaller inner-electrode distance leads to a

[9] The AFP pixel detectors is based on the 3D double sided sensors developed by CNM (Centro Nacional de Microelectronica, Barcelona, Spain) for the Insertable B- Layer (IBL)

shorter collection time and smaller depletion distance. Secondly, an ionizing particle generates charge carriers almost parallel to the collecting electrodes in the 3D detector; therefore all charges generated from the track have similar collection times inducing a signal with a faster rise time. This implies that the device is extremely fast, has high charge collection and a low operating voltage, and therefore low power consumption, even after a high irradiation dose. Aside from all the other bonuses of 3D design, the enclosed structure of the unit cell of the 3D detector will also reduce the amount of charge sharing, which could be advantageous in increasing the signal in a given pixel after heavy irradiation. These features make the 3D sensor more radiation resistant compared to the regular planar sensors. Thirdly, since both types of electrodes can be accessed from the top surface of the detector, it is possible to do the read-out simultaneously from both n^+ and p^+ electrodes. Finally, the excess material surrounding the detector can be etched away and this technique eliminates the need of using guards [10] (which is a necessary part of the saw-cut detectors). Therefore the electric field can extend right up to its physical edge (115 μm).

There is a 3D-silicon tracking station to measure scattered protons in each of the AFP Roman Pots. Each tracking station consists of four tracking detectors each comprised of a single FE-I4B [20] front-end chip which features an array of 336×80 pixels with a pixel size of 50×250 μm^2 [65]. Therefore, the active area covered by the tracking detector is approximately 17×20 mm^2. The single chip 3D pixel modules used by AFP are similar to the ones used in the ATLAS Insertable B-Layer (IBL) detector and have demonstrated radia-

[10] The role of a guard rings is to draw the excess leakage current from the sensors

tion tolerance. The FE-I4B readout chip meets the specific requirements for AFP: the granularity of cells provides a sufficient spatial resolution[11]; the chip is sufficiently radiation hard (up to 3 MGy $\frac{\mathrm{MJ}}{\mathrm{kg}}$) [67]; and, the size of the chip is quite large (it is the largest readout chip that has been used at the LHC).

4.1.3 Time of Flight System

ToF is a fast timing detector that measures the time difference between the arrival of the two outgoing scattered protons in the AFP detectors on either side of the ATLAS interaction point, enabling the z-position of their common vertex, if any, to be calculated. This determination allows pileup background to be severely reduced.

As the instantaneous luminosity increases at the LHC the number of pile-up events increases. At high luminosity, the ToF detector becomes essential since the AFP detector can tag the two outgoing protons from a diffractive process in the very forward region of the ATLAS detector. The ToF detector resolution lies between 10 ps [12] and 30 ps allowing us to determine the longitudinal position of the vertex with precision of 2.1 mm to 6.4 mm, respectively. By matching the vertex position as determined in the central system, measured by the central detector with precision of 50 μm and the vertex position determined by AFP, it can be concluded whether the two protons originate from the same interaction, otherwise, the event will be tagged as pile-up.

At the nominal luminosity of the LHC, an important exclusive DPE pro-

[11] In a test beam in 2016, the overall resolution of the tracker detector has been measured as 15 μm (73 μm) in the short (long) pixel direction

[12] When two oppositely directed particles are timed relative to each other, with a time difference Δt, the point of origin z can be determine with the precision of $\Delta z = \frac{C\Delta t}{\sqrt{2}}$. Therefore, precision of 10 ps translates to $\Delta z = 2.1$ mm in the vertex position

duction background is when: two single diffractive events with a central hard scatter all overlap, as shown in figure 4.4 case (a). In this case the two diffracted protons come from separate vertices. There are also two more situations possible in which events from two independent interactions superimpose to form a background event. The first of these occurs when one interaction with the central system overlaps with a double tag soft interaction, as shown in figure 4.4 case (b). The second two-vertex case happens when single diffractive jet production with one tagged proton overlaps with a single tag soft interaction, as shown in figure 4.4 case (c).

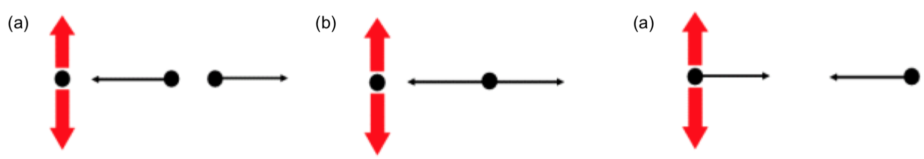

Figure 4.4: A schematic diagram of overlap backgrounds to central exclusive production

LQbar

The Quartic detector is used to determine the ToF of the deflected protons from, an exclusive interaction, entering the AFP detectors on either side of the ATLAS interaction point. Quartic is a Cherenkov detector utilizing quartz bars as radiators with a Micro-channel Plate Photomultiplier (MCP-PMT) for readout. In the Quartic design, the fused silica (quartz) bars are oriented at the Cherenkov angle. As a result, the reflection of the light inside the bars will be reduced and a number of the Cherenkov photons created by the proton passing through the quartz radiator bars will reach the PMT at the same time.

In the new design, the timing system is again based on Cherenkov emission in fused silica radiators. It consists of fused silica ("Suprasil") bars to guide the Cherenkov light to the PMTs. Because of the geometry of Roman Pot, the light has to be brought out perpendicular to the beam, therefore, the quartz bar has designed in L-shaped configuration and hence are called "LQbar".

For technical reason, the LQbars are not made in one piece but two pieces. The two bars are glued together as it is shown in figure 4.5. Because the relativistic protons emit a Cherenkov light in a Cherenkov cone of 48^0 the radiator arm has 48^o cut on its free side. After the beam of protons hit the radiator arm at 48^0 angle and produce Cherenkov light, the radiator which also acts as a light guide conducts the light in a direct path. In order to reach the MCP-PMT, the light is reflected through 90^o by a 45^o cut of the radiator at the junction of the two arms of the LQbar. A layer of aluminium is electro-deposited on the outside of the 45^o junction to enable reflection of the Cherenkov light, generated by the passage of a proton through the LQbar, into the MC-PMT. Figure 4.5 shows the schematic view of the 4×4 row of LQbar radiators of the ToF detector.

In summary, the baseline design of AFPs ToF detector (QUARTIC) consists of 16 LQbars organized into four rows (called trains) of four LQbars each. The length of all the radiators bars in the z-direction is 6 mm and the length in the x-direction ranged from 35 to 57 mm in order that the prompt Cherenkov light, from a traversing proton, in each bar can reach the PMT at the same time. The light reaching the MC-PMT is converted to a signal by a specialized 4×4-pixel MCP-PMT. The signals of all PMTs are amplified, discriminated by

CFD (Constant Fraction Discriminator) and digitized by the HPTDC (High Precision Time to Digital Converter) board.

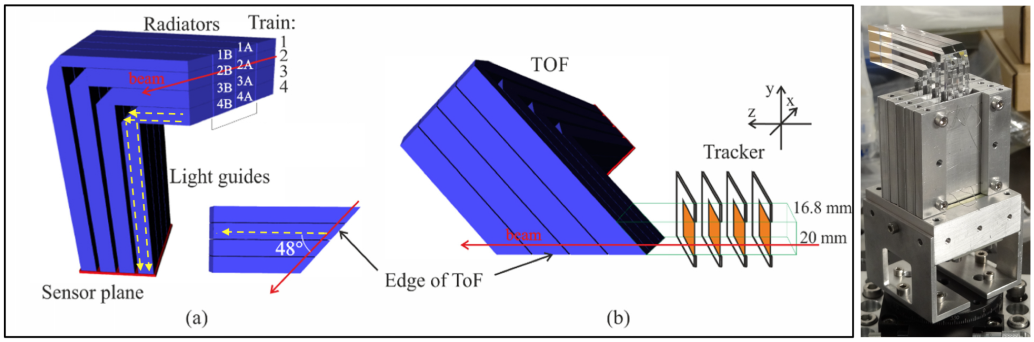

Figure 4.5: The left hand picture is the schematic view of the 4×4 row of LQbar radiators of the ToF detector. It shows the passage of a Cherenkov photon emitted from a proton through the Silicon Tracker detector and LQbars in ToF detector. The right hand picture is a prototype of the new LQbar-mounting made in the University of Alberta.

4.1.4 ToF Electronics

The primary purpose of the ToF electronics is to measure the flight time of charged particles while preserving the timing resolution of the overall detector at the level of 20 ps. The ToF electronic consists of MCP-PMT, preamp, CDF, and HPTDC as shown in figure 4.6. The ToF electronics system will be discussed in more detail below.

MCP-PMT

The ends of all the LQbars were brought into contact with a 10 μm channel size MCP-PMT by photonics. MCPs are quite different in structure and operation from conventional PMTs. They consist of an input window, photocathode, anode, and Micro-channel plates (MCPs) instead of dynodes. The MCP con-

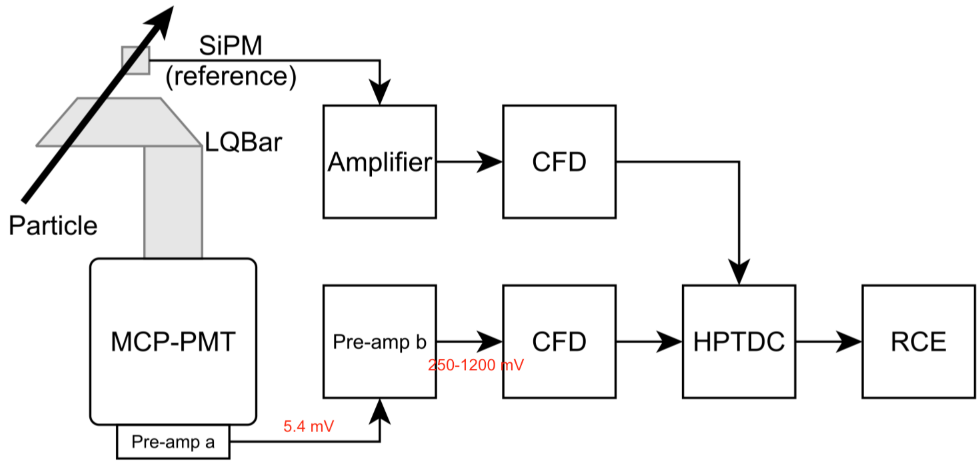

Figure 4.6: AFP electronic readout layout.

sists of an array of small diameter special glass tubular channels bundled in parallel and sliced to form thin discs with thickness of around 100 times the diameter of the glass tubes. In the case of AFP, each channel has an internal diameter around 10 μm that acts as an independent electron multiplier. A schematic view and working principle of an MCP is shown in figure 4.7. A photon incident on the window of the MCP is absorbed by the photocathode deposited on the inner surface of the window. The electron resulting from this interaction is accelerated by an electrical potential and hits the MCP surface, usually within the mouth of one of the micro-channels constituting the MCP. On average, more than one electron is emitted by the material of the micro-channel wall. A strong electric field is maintained across the MCP, electrons impinging on a MCP start a cascade of electrons in a micro-channel that propagates through the channel, amplifying the original signal by several orders of magnitude depending on the electric field strength and the geometry of the micro-channel plate. The resulting pulse of electrons exits the opposite side of the plate where they are collected by the anode structure of the MCP-PMT. Also, because the electron amplification occurs in a very spatially confined region, Transit Time Spread (TTS) is very small. This design gives significantly better single photon time resolution than those of the standard PMT tubes due to the shorter electron travel and reduced transit time jitter.

The MCP-PMT has the ability to work in a magnetic field without dramatic loss of gain. It is compact and, for the AFP application, is equipped with a position sensitive multi-anode readout system with 4×4 anode pixels of 6×6 mm^2 size with a position resolution that depends on the anode structure and size. The transit time jitter of the MCP-PMT can be as small as several picoseconds, allowing the possibility of a time resolution of the same order as that of the transit time jitter.

Despite the compact size of MCP-PMT, the amplification is about one order of magnitude less than regular PMTs (about 10^5). The MCP-PMT used in the AFP ToF detector is operated at lower gain about 5×10^4, to maximize its lifetime.

CFD and Preamplifier

Discriminators generate precise logic pulses in response to input signals exceeding a given threshold. There are two main types of discriminators, the leading edge discriminator and the constant fraction discriminator. The simpler leading edge discriminator produces an output pulse at the time when the input pulse crosses a given threshold voltage. However, the timing of the output pulse varies with amplitude of the input signal.

CFD's are designed to produce accurate timing information from analog

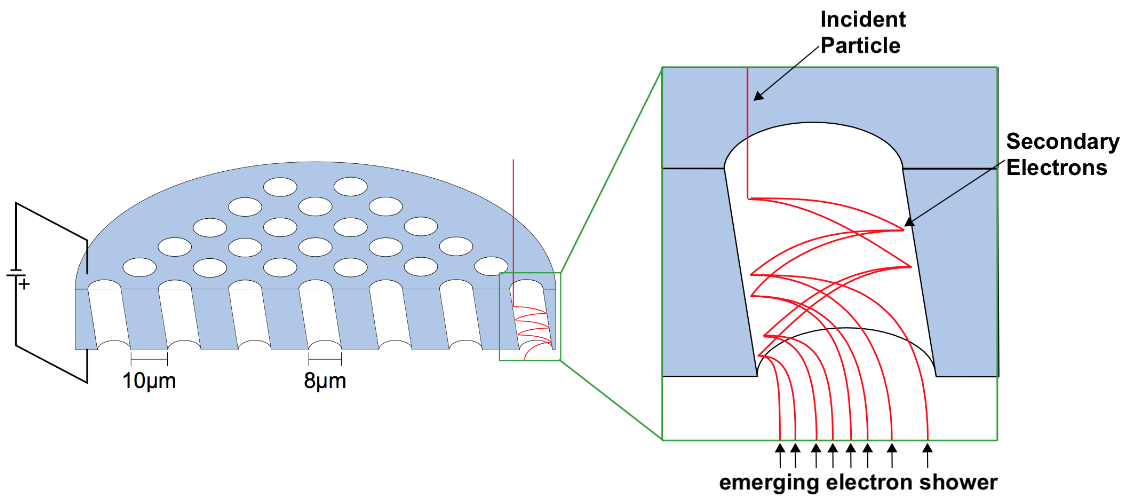

Figure 4.7: Schematic view of a MCP

signals of varying amplitudes but similar rise times. They accomplish this by producing a timing signal at a constant fraction of the input amplitude, usually chosen to be around 20%. The output from the CFD is sent to a High Precision Time Digitizer board (HPTDC) to get digitized.

The typical MCP-PMT output signal peak value at this gain is about 5.4 mV. Whereas the input for CFD is in the range of $50 - 1200$ mV. Therefore, we need a pre-amplifier to connect them.

High Performance Time Digitizer (HPTDC) board

The HPTDC is a High Performance multi-hit and multi-channel Time to Digital Converter (TDC) chip [75] used to processes the signals that are received from CFD. The HPTDC ASIC allows precise time-tagging of up to 32 input channels relative to an external clock reference of 40MHz. Based on an integrated clock multiplying Phase Locked Loop (PLL), a 32-channel Delay

Locked Loop (DLL) with integrated RC-delay lines provides time interpolation down to 25 ps. The HPTDC board has Low-voltage differential signalling (LVDS) inputs [13], internal buffers, multi-hit, multi-event and trigger matching capabilities and it is sensitive to both leading and trailing edges of the pulses that makes it capable of measuring pulse width.

The HPTDC architecture is divided into two main functional units: A timing unit, a digital data processing and buffering, as shown in Fig:4.8.

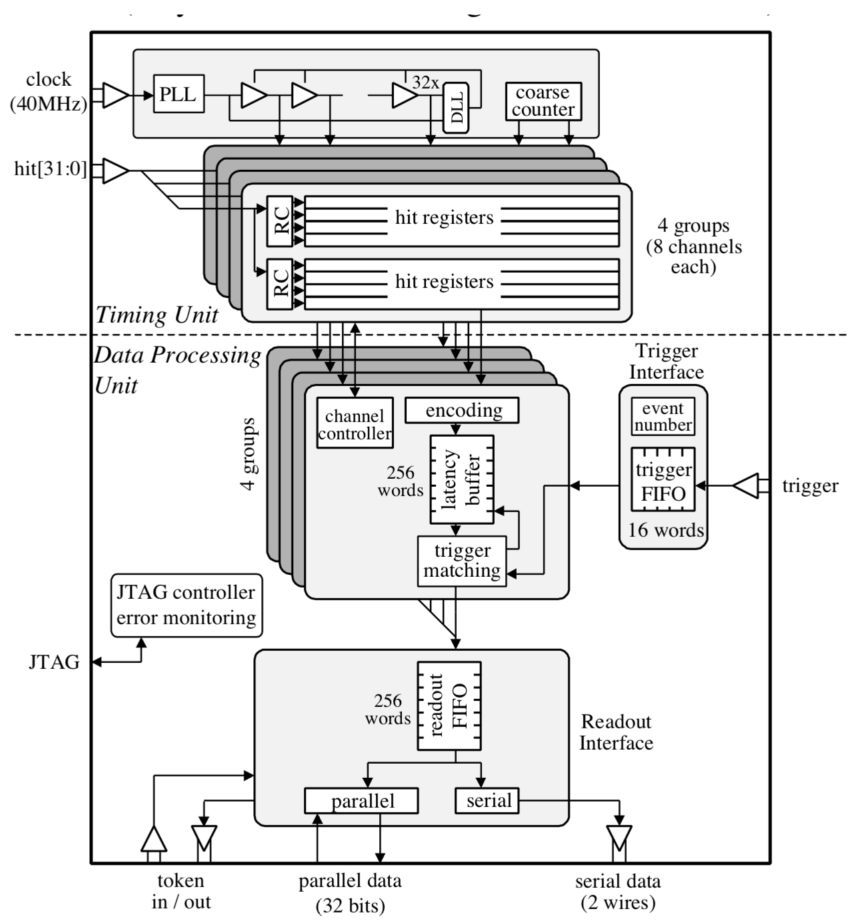

Figure 4.8: The architecture of the HPTDC chip [75].

[13]LVDS digitally transmits information as the difference between the voltages on a pair of wires. The receiver detects the voltage difference between the two signals and determine the logic level.

The timing unit performs digitization to time with high precision. It also consists of three elements, shown in figure 4.9.

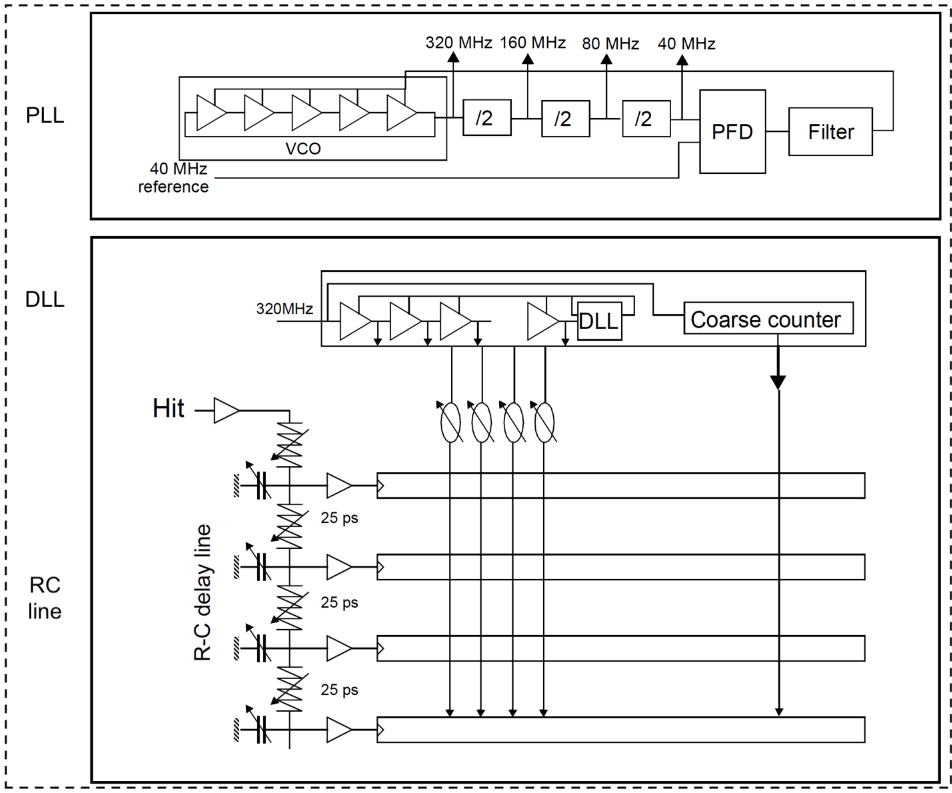

Figure 4.9: HPTDC timing unit [75].

A Phase Locked Loop (PLL) is used to reduce jitter on the incoming clock signal and generates a 320 MHZ clock from the LHC clock. The HPTDC ASIC uses the LHC 40.08 MHz bunch-crossing reference clock to synchronize the input signals to the bunch crossings of the LHC. Without the PLL, the resolution of TDC is limited by the frequency of the reference clock but the PLL can perform clock multiplication - to increase time resolution - from a 40 MHz (input clock) to 160 MHz, and ultimately to 320 MHz.

A Delay Locked Loop (DLL) is used to perform time interpolation within the reference clock cycle to increase the precision of the time measurements. The DLL consists of a chain of 32 delay elements. Therefore one clock period can be divided into 32 clock phases. The best time resolution the TDC can obtain on 32 taps is 97 ps [14]. As the DLL is sensitive to jitter on its input clock, any jitter on the clock will directly deteriorate the precision of the time measurements. The PLL can remove jitter on the input clock to some extent. In the next chapter, we will discuss a method of calibration to reduce the jitter of the clock even more during the analysis of data.

Aside from DLL, another method of the resolution improvement is to use an adjustable resistor capacitor (RC) delay line. An RC delay line interpolation is obtained by sampling the signal with the DLL four times. In this way the time resolution will be improved four times. Therefore, the time delay is equal to $T_{delay} = T_{clock}/(32 * 4) = 24.4$ ps.

The second part of the HPTDC is digital data processing and buffering. When a ToF hit signal reaches the HPTDC, a hit measurement is performed by storing the state of the DLL, RC and the coarse counter in binary code, when a hit is detected in a channel. The channel buffers enable multiple time measurements to be made with short dead time of 5 ns. The complete time measurement is written into the L1 buffer together with a channel identifier. The L1 buffer is a 256-word circular buffer shared by a group of 8 channels. Each HPTDC chip has 32 channels but in high resolution mode 4 channels are combined, the HPTDC chip can support 8 high resolution inputs but pairs of channels share one L1 buffer. To avoid the overflow of the L1 buffer at high rates there are only 4 channels on each chip.

[14] $T_{clock}/32 = 97$ ps

The L1 buffer output is passed to the trigger matching function which perform a time match between a trigger time tag and the time measurements from the L1 buffer. Then the hits that are matching the trigger are passed to the 256 words deep read-out FIFO.

4.1.5 The AFP Trigger and Data Acquisition System

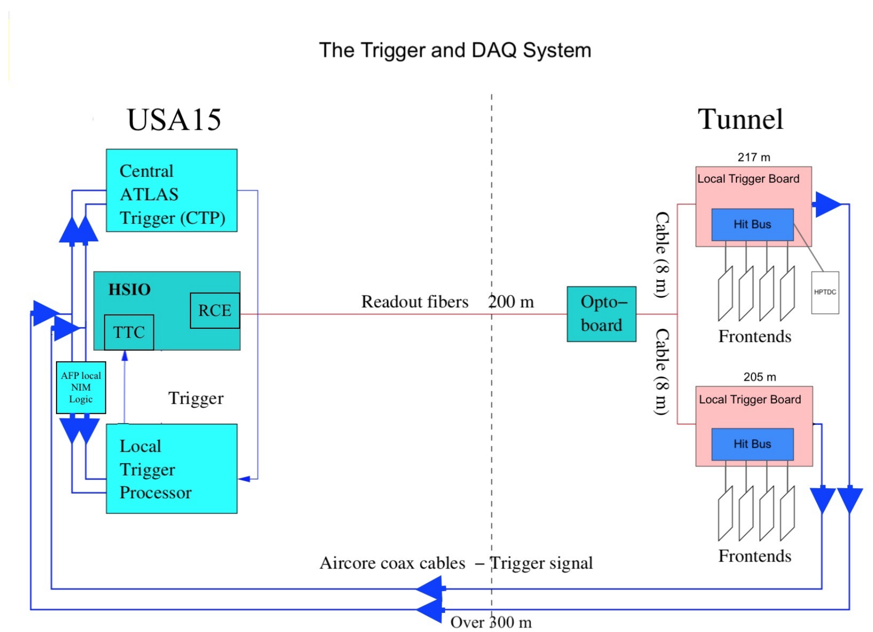

Figure 4.10: AFP Trigger setup

The AFP stations are located far from the ATLAS TDAQ system. In order to use ATLAS TDAQ system for triggering and processing data, the local trigger formation of AFP must be formed at the front end in 100 ns to be within the ATLAS L1 acceptance window, which is 2.5 μs. In this section, the AFP L1 trigger and its functionality are discussed.

Four FE-I4B readout modules are located at the 205 m station, and another four modules plus the ToF HPTDC module are placed in the 217 m station.

L1 triggering for the silicon Trackers is based on the HitOR from the FE-I4B readout chips. Each FE-I4B chip gives a HitOr signal if at least one pixel fires which is available about 50 ns after the charge injection. Using the rad-hard HitBus ASIC [62], installed on a Local Trigger Board (LTB) in each station allows selection of three out of four FEI4 modules to produce a majority trigger, if at least two planes detect signal.

The ToF front-end electronics (HPTDC) can also be used for triggering using the signals from the LQbar. The advantage of using the HPTDC board as a trigger for L-1 triggering is that the dead time is as low as a few nanoseconds and it is possible to trigger all the events whereas in the Tracker system some events will be missed due to the high dead-time of the trigger.

The AFP trigger delay must be minimized in order to be inside the L1 acceptance widow, which puts a premium on ultrafast cables and trigger logic. The signals travel from AFP station to ATLAS USA 15 cavern [15] over 350 m along special air-core cables with the transmission speed of 93% of the speed of light.

In ATLAS USA 15 cavern, the signals are split between the ATLAS CTP and the AFP local NIM logic which produces logical AND or OR and then sends the resulting signal to the AFP Local Trigger Processor (LTP). The CTP generates an L1A signal derived from the trigger inputs according to the L1 trigger and fans it out to the Timing, Trigger, and Control (TTC).

The LTP provides the facility to run with the trigger and timing signals from the CTP but it also selects the source of the AFP trigger either as ATLAS

[15] The USA 15 cavern in the ATLAS experiment is an underground halls that contains most of the electronics for the experiment

trigger, if the AFP participates in the ATLAS combined partition, or, as the NIM local logic, when the AFP performs commissioning or calibration runs.

The TTC interface transmits the L1A signal and the trigger control commands to the High-Speed Input-Output (HSIO)-II board to process and forms the data request for the front-ends.

The output signal is then transmitted over a 200 m long optical MTP fibre ribbon to the Opto-board. The Opto-board decodes and converts the bitstream to 40 MHz clock and 40 Mbps data stream in LVDS format and forwards them to the HitBus chip at the LTB via an 8m long twisted pair cable.

On the return path, the stream of the front-end data is then deserialized, decoded and stored in the HSIO. When the data from all front-ends arrive, the HSIO forms a single data fragment and sends it off via the SFP output line to the ATLAS Readout System.

4.1.6 Performance of the ToF system

To understand the performance of the AFP detector and its components in response to high energy particles, beam test studies are essential. The first unified AFP prototype, which combined tracking and timing prototype detectors (excluding the Roman pot housing) was tested at the SPS with 120 GeV pions in November 2014, September 2015, and September 2016. The AFP prototype was built of five tracking planes and a ToF system.The timing system consisted of four rows of two LQbars. In addition to the ToF detector, two fast timing reference detectors consisting of quartz bars (3×3 mm^2

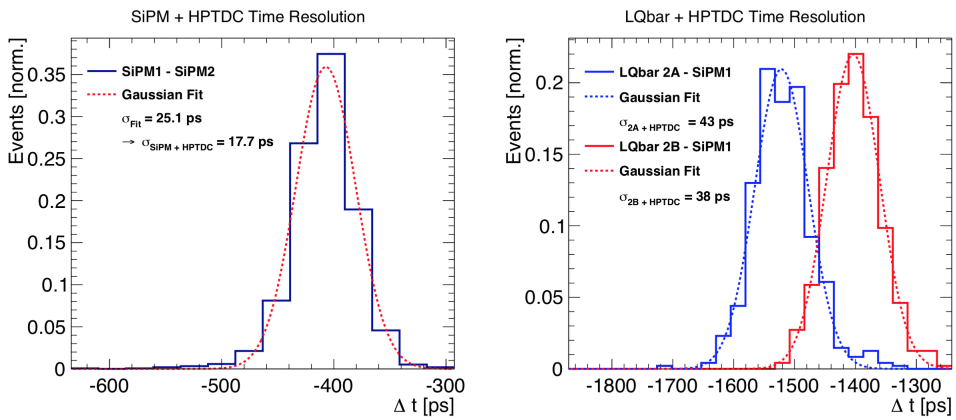

Figure 4.11: Time differences measured with the HPTDC-RCE readout. (Left plot) shows the time differences between the two SiPM channels measured by the HPTDC. (Right plot) shows the time differences between the LQbars and the SiPM reference channel.

.

cross-section, 1 cm long in beam direction) coupled to silicon photomultipliers (SiPM) that were placed behind the AFP prototype about 5.5 mm away from the LQbar cut edge which gives partial overlap with the LQbar (only trains 1 and 2). These two channels are used as the time reference. Then signals of all timing detectors were amplified, discriminated using CFD, and digitized with the 12-channel HPTDC.

In order to determine the precision of the ToF detector we need to understand the time resolutions of the SiPM reference devices and HPTDC. Figure 4.11 shows a Gaussian distribution with a total convoluted width of 25 ns is fitted to the time difference between SiPM1 and SiPM2 including the HPTDC contributions. Therefore, the resolution of a single SiPM+HPTDC device is $\sigma SiPM + HPTDC = \frac{25}{\sqrt{2}} = 17.7$ ps. A similar analysis has been performed with the LeCroy SDA760ZI oscilloscope, with a time resolution substantially better than the HPTDC, in order to measure the resolution of SiPM which is $\sigma_{SiPM} = 11$ ps and the resolution of the oscilloscope is ignored. Therefore, the HPTDC resolution can be estimated from quadratic subtraction as $\sigma_{HPTDC} = 13.9$ ps[16], which is within the range of 12 to 17 ps measured in the laboratory. In the next chapter, the test performed on HPTDC in the laboratory of the University of Alberta will be shown.

The LQbar time resolutions were also measured from the time differences between one bar and one of the SiPM references while the SiPM and the LQbar channels were connected to different HPTDC chips. This measurement could only be performed for the trains 1 and 2 (for LQbar 1A, 1B, 2A, 2B) which had an overlap with the SiPMs so that the test beam particle passes through both SiPM and LQbar. The time differences shown in figure 4.11 gives the time resolutions of the full LQbar timing detectors including the PMT, CFD and HPTDC contributions were measured between 38 ± 6 ps and 46 ± 5 ps per LQbar. Also, in this test, the resolution of the average time of the two LQbars in one train, for both A and B trains, is measured at $V_{MCP-PMT} = 1900$[17] to be 35 ± 6 and 37 ± 6 ps per train. As it is expected the train average (with two LQbar in each train) improves the resolution with respect to the measurement with one LQbar.

[16] Assuming both channels+SiPM combinations have the same resolution with no correlation

[17] Voltage of the MCP-PMT can change the resolution of the ToF and its efficiency. The highest resolution is achieved when $V_{MCP-PMT} = 1900$ V, however the efficiency reduces as the voltage goes down

4.2 The HPTDC Testbed

This chapter provides the overview of the testbed that was built for the purpose of calibrating and testing the precision of HPTDC channels. The main purpose of this testbed was to measure the $\sqrt{n}$ improvement in time resolutions when combining multiple ToF measurements.

4.2.1 Introduction and Apparatus

When multiple measurements (N) of the same quantity are made by the identical detectors with resolution sigma then the overall resolution is $\frac{\sigma}{\sqrt{N}}$. This is provided that the channels are all independent and not affected by any coherent noise effects. The AFP ToF detector has taken advantage of the "square root" effect to improve the resolution of the detector by sampling each of the four LQbars in the train through which the proton passed and then combining the multiple (4) measurements. In this chapter, we study this effect with individual channels of a HPTDC board.

The HPTDC boards that are used in AFP electronic system were designed and constructed at the University of Alberta. The time resolution of each of the 8 channels is approximately 13 ps. The HPTDC chip designed by microelectronics group of CERN is the main element of the HPTDC board. It has a total of 32 input channels. In high resolution mode, four channels are ganged to together, giving 8 high resolution channels per chip. The time resolution of the HPTDC chip in high resolution mode is 25 ns per high resolution channels (4 regular channels). Each board houses three HPTDC chips which are controlled by a Field Programmable Gate Array (FPGA) which also control and handles the flow of data. The current versions of the HPTDC board was used successfully at various beam tests, and for AFP data taking as part of the ATLAS detector.

The radioactive environment on the tunnel floor, where the TDC boards are installed, may degrade the timing performance over time. Therefore testing was performed with a board at the University of Alberta already exposed to 10^{12} Neutron/cm^2. Figure 4.12 shows the HPTDC that we used for the test. No obvious degradation in performance was measured.

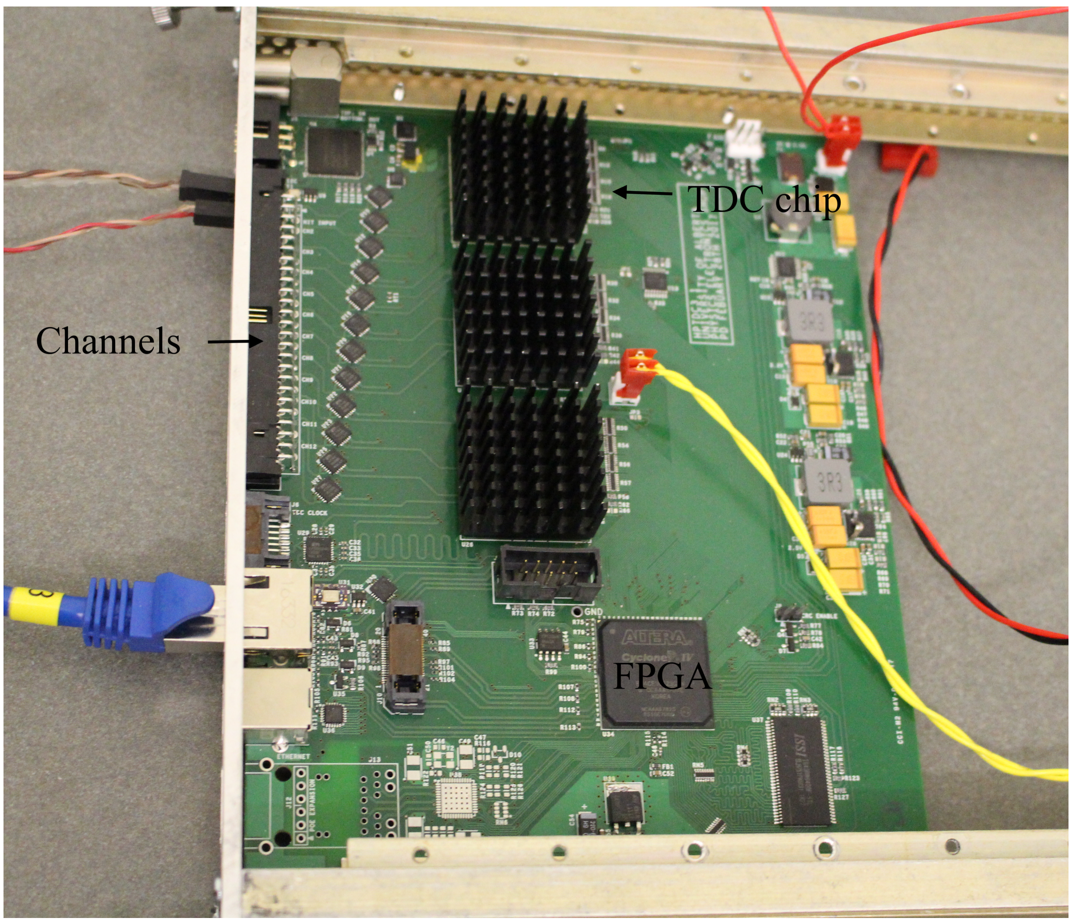

Figure 4.12: The University of Alberta HPTDC board.

The time measurements on each HPTDC chip comes from course counter

(PLL), fine measurement (DLL) and four-stages RC delay are stored in 21-bit data packets. The course counter which increments every 3.125 ns provides the most significant 11 bits of the time measurement. The next 5 bits encode the fine time measurement which is a 32 element delay locked loop(DLL) with each delay being 97 ps. Finally, in high resolution mode, the state of the course counter and fine measurement is captured four times with 24.4 ps delay between each measurement and then interpolated by determining where the DLL value changed to provide the final 2 bits of the time measurement.

The HPTDC chip uses a set of RC delay lines to produce these delays. Capacitor loads can be switched into each delay line to adjust the delay. By producing a histogram of the last 2 bits of the time measurement the delays can be inferred and the delay lines adjusted with the bins that are too high representing delays that are too long and bins that are too small representing delays that are too short. Unfortunately, the HPTDC chip does not allow these delays to be adjusted for each individual channel but must share a common setting for all channels. As well there is not enough adjustability so that bins cannot be fully adjusted to their ideal [75].

Moreover, the delay line used by the TDC chip is not linear as it ideally should be for precise measurement. Some bins end up being larger than others and this accumulates along the length of the delay line. This non-linearity can contribute a timing error of up to ±6 bins (±150 ps). This non-linearity can be measured by performing a code density test where a signal that is not correlated to the TDC clock is connected to each hit input. An ideal TDC with no nonlinearity would show a flat histogram with the equal number of hits per bin. In reality, the time represented by each bin varies and therefore the histogram varies too. Bins that are larger will show a higher number of hits in the histogram while short bins will be lower. For a precise time measurement all the bins need to be calibrated to the fine time bin size which is 24.4 ps in the HPTDC, also known as the least significant bit (LSB).

The following subsections describe the testbed that is used for the calibration of each HPTDC channels and precision measurements.

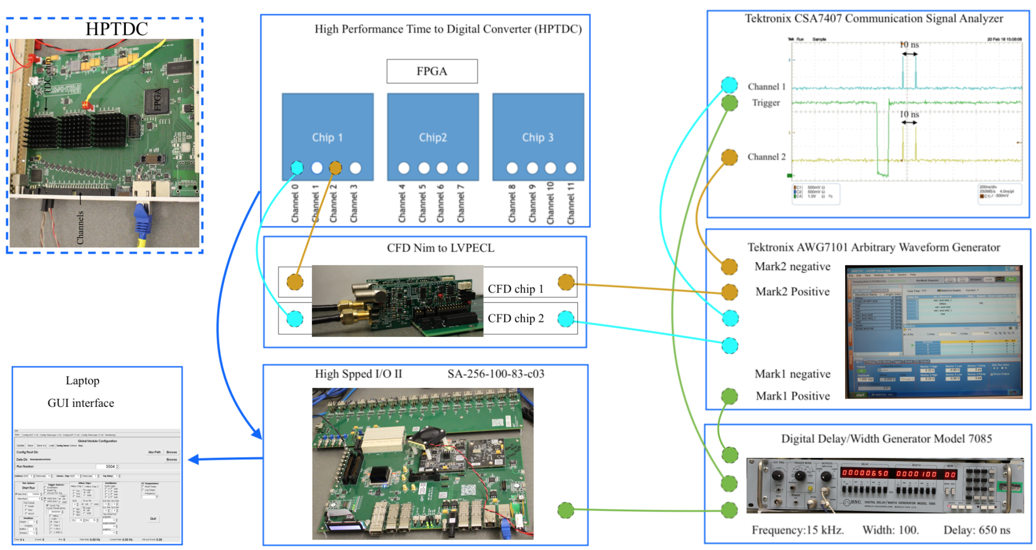

Figure 4.13: A general view of the setup for testing HPTDC channels calibration and precision.

Figure 4.13 shows a general view of the setup we used for all the tests described in this section. We used aTektronix AWG7101 Arbitrary Waveform Generator (AWG) to produce random hits for calibration of the TDC channels and a double pulse for resolution measurement. Random hits are needed that are not correlated with the reference clock. We set the sampling rate of the AWG to the 9.23 Gsample/s to desynchronized the generated pulses from the 40 MHz HPTDC internal clock. In this way the pulses hit the HPTDC at random time, each HPTDC bin should receive about the same numbers of hits.

Double signals are made from two simple signals with the sufficiently large time interval for measuring the resolution of the HPTDC channels without any inter-channel interference.

To trigger the AWG and RCE system simultaneously, a Digital Delay/Width Generator which set to output a 15 kHz square wave with the width of 100 ns has been connected to both systems. Each signal is sent to a CFD which is used as NIM to LVPECL convertor[18]. Then the signal passes to the HPTDC through one of the twelve LVPECL inputs. The channels are numbered from 0 to 11. In the HPTDC the time of the rising edge of each input is captured continuously with bins of 24.4 ps and a 5 ns dead time. The channels of the three HPTDC chips on the HPTDC board are numbered as: TDC 1 includes Ch0 to3, Ch 4 to 7 are on TDC2 and Ch 8 to11 are on TDC3. Finally, data from HPTDC board passes to the HSIO board which is used to readout the HPTDC data via an on-board FPGA which decodes commands and formats the HPTDC data output stream. The software for the HSIO is a ROOT-based program which communicates with the module and sends the data to the local laptop. Cosmic Graphical User Interface (GUI) is used as the TDAQ. The tasks of the GUI is to monitor the system status, control the number of events and produce root files from the data that sent from HSIO.

[18]Only in this setup

4.2.2 Channel Calibration

The delay line used by the TDC chip is not linear as it ideally would be. Some bins end up being larger than others and this accumulates along the length of the delay line which leads to a big error in time measurement by TDC. This non-linearity can be measured by performing a code density test where a repetitive signal that is not correlated to the TDC clock passed to one channel of TDC and generates a corresponding hit distribution in the bins. In an ideal TDC with no non linearity, the distribution of hits would be equal in all $2^{10} = 1024$ bins from the RC (2 bits), DLL (5 bits) and PLL (3 bits).

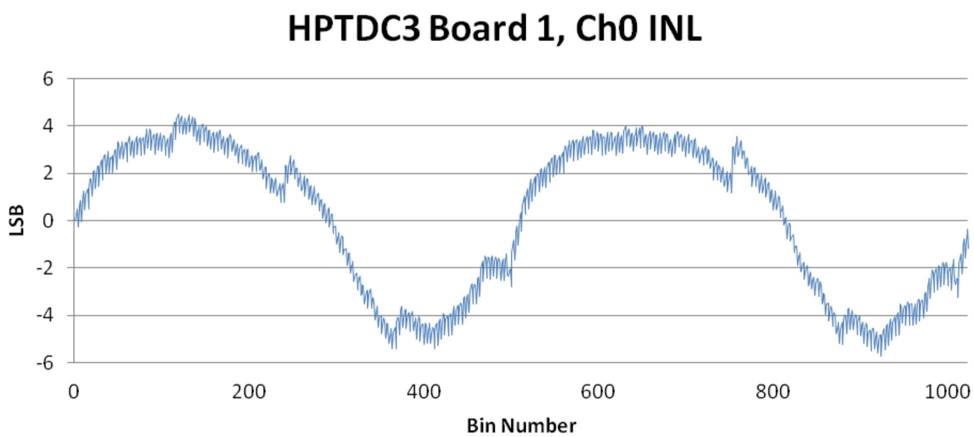

Figure 4.14: Shows the HPTDC bin offset: ($bin_i = \frac{2^{10}A}{B} - 1 + \sum_i bin_{(i-1)}$) where A is the hit number in bin_i and B is the total number of hits

Figure 4.14 shows the offset error or INL (Integral nonlinearity), which is the deviation between the ideal input value and the measured value, for each bin in a specific channel in terms of LSB. The histogram test reveals the accumulated nonlinearity error, including all PLL, DLL and RC related errors. This non-linearity can contribute a timing error of up to ± 6 bins (± 150 ps). The same test can be performed for each channel of HPTDC, in order to calibrate each channel individually.

To compensate for the offset bins, we provided a text file from the histogram in figure 4.14 with the list of offset LSB numbers for all 1024 bins for each channel and subtract the offset value from the related bin number in the offline analysis. Currently, the correction is only applied offline during analysis of the data. However, because of the sensitivity of INL to the environmental changes, future revisions may perform the calculation on board. Figure 4.15 shows the distribution of the hits in one channel before and after the correction and it improved the resolution of the channel from 38.8 ps to 15.97 ps.

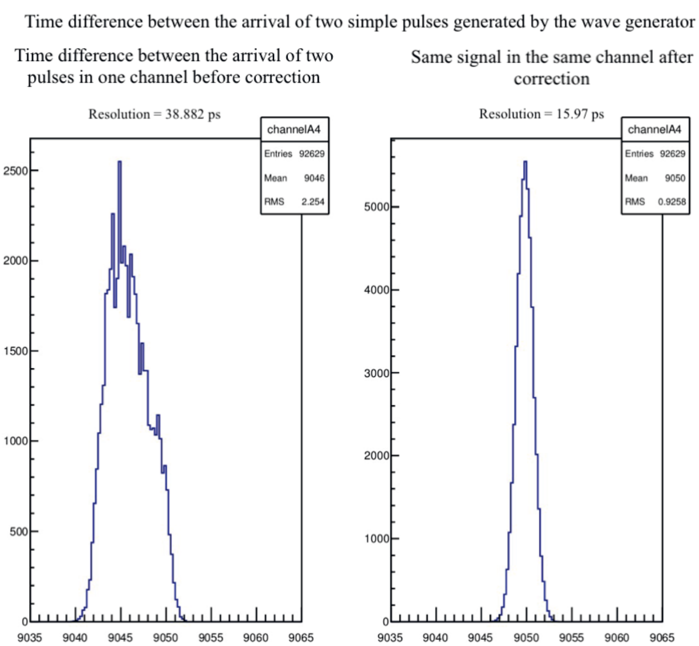

Figure 4.15: HPTDC channel calibration. (Left plot) shows the time difference between the arrival of two pluses in one channel without LSB correction. (Right plot) same distribution after applying Applying the LSB correction.

4.2.3 Resolution for Each HPTDC Channel

After applying the INL calibration in the analysis, the next step is to determine HPTDC channel timing precision. In this test, two simple consecutive pulses are produced via wave generator then the difference of the two leading edges are measured on the same channel. To obtain the intrinsic TDC resolution one can divide the width of this distribution by the square root of two. For the purpose of this test the time interval between the two pulses is chosen to be about 150 ns, all the other channels were inactive to avoid any crosstalk or correlation between channels. Table 4.1 shows the resolution of each individual HPTDC channels. The resolution of the channels varies between 12 ps to 17 ps.

Channel	0	1	2	3	8	9	10	11
Resolution (ps)	14.26	13.76	14.85	16.84	12.72	13.63	12.79	13.69

Table 4.1: The performance of each channel of HPTDC

4.2.4 Standard Error Of The Mean In Two-Times-Measurement

In this subsection, we explain the test of the square root effect in the HPTDC channels using the setup that described in the previous section. The pulses that are used in this test are two simple double pulses that are sent to two different channels on two different chips on HPTDC, simultaneously. On each channel, the rising edge of each of the pulses in the double signal pulse are measured by the HPTDC and the distribution of the difference between the times measured by two channels are obtained in 100000 events. In this test, we used channel 0 on the first chip along with one of the other channels on the first chip and the third chip.

	Channel	Resolution (ps)	Measured resolution of the two channel (ps)	Expected resolution using "Square Root Effect"(ps)	"Square Root Effect" error (%)	Correlation between the two channel
1	ch0	18.38	13.79	12.20	13.03%	12.54%
	ch1	16.15				
2	ch0	18.69	13.83	12.96	6.71%	7.02%
	ch2	17.96				
3	ch0	21.00	16.35	14.00	16.78%	17.42%
	ch3	18.62				
4	ch0	17.74	13.45	11.67	15.25%	16.11%
	ch4	15.28				
5	ch0	17.72	12.94	11.89	8.83%	9.03%
	ch5	15.92				
6	ch0	17.74	13.14	11.8	11.35%	11.38%
	ch6	15.64				
7	ch0	17.72	14.03	12.55	11.79%	12.61%
	ch7	17.78				

Table 4.2: The performance of two active channels of HPTDC, measuring the arrival of the same waveforms.

Table 4.2 shows the resolution of the two active channels (σ_x and σ_y), standard deviation of the mean of the two active channel divided by square root of 2, $(\frac{\sigma_{mean}}{\sqrt{2}})$[19], average of the standard deviation of the two channel divided by square root of two $\sigma_{Expected} = \frac{Mean(\sigma_a+\sigma_b)}{\sqrt{2}}$, the square root effect error $(\frac{\sigma_{Average}-\sigma_{Expected}}{\sigma_{Expected}})$, and the correlation of the two channels $(\sum_i \frac{(x_i-\bar{x})(y_i-\bar{y})}{\sigma_x \sigma_y})$.

Due to the possible correlation between the active channels, the resolution of the individual channels drops by a few picosecond as more than one channel is active at a time. Clearly, the precision of the measurement with two channels $(\frac{\sigma_{mean}}{\sqrt{2}})$ improves in comparison with the resolution of each individual channel. However, this improvement is not as good as that predicted by the "square root of two" effect. This is due to the presence of a slight correlation between the channels.

4.2.5 Conclusion and Future Work

In this section, the calibration method and the timing resolution of an HPTDC board that is used in ToF electronics are reported. The resolution of the individual channels varies between 12 to 17 ps. However, the resolution of each channel in isolation degrades slightly when more than one channel on the board is active at the same time. We also have tested the square root effect by measuring the same quantity with two separate channels. The double measurement of the same quantity makes the measurement more precise compared to the individual channel precision when there are other active channels at the time of measurement.

There are possible improvements that can be made to automate the calibration and improve the timing resolution of the HPTDC. Firstly, currently, the

[19] Average histogram $(bin_i) = \frac{\text{First channel histogram } (bin_i) + \text{Second channel histogram } (bin_i)}{2}$

correction is applied offline during analysis of the data. Future revisions may perform the calculation on board. Secondly, by identifying and removing the sources of the correlation, that are believed to be mainly due to cross-talk on the board. After crosstalk correlation effects are removed, by a HPTDC board redesign, we should see a significant improvement of the timing resolution of the HPTDC

Chapter 5

Higgs production in exclusive diffraction

5.1 Quantum Chromodynamics, Asymptotic Freedom and The Running Coupling Constant

QCD is a quantum field theory that describes the strong interaction which is interpreted as the interaction between colour-charged quarks q_f and vector gluons A_μ. The QCD Lagrangian is comprised of three parts that describe the gauge bosons (gluons), the fermions(quarks) and their masses and finally the interaction part (between quarks and gluons) with coupling g_s.

$$\mathcal{L}_{QCD} = \mathcal{L}_{gluon} + \mathcal{L}_{quark} + \mathcal{L}_{interaction}, \tag{5.1}$$

where:

$$\begin{aligned}\mathcal{L}_{gluon} &= -\frac{1}{4}F_{\mu\nu}F^{\mu\nu} \\ F_{\mu\nu} &= \partial_\mu A_\nu - \partial_\nu A_\mu - ig_s[A_\mu, A_\nu],\end{aligned} \tag{5.2}$$

and

$$\begin{aligned}\mathcal{L}_{quark} &= \sum_f q_f(i\gamma^\mu\partial_\mu - m_{q_f})\bar{q_f} \\ \mathcal{L}_{inteaction} &= \sum_f q_f(\gamma_\mu g_s A^a_\mu t^a)\bar{q_f},\end{aligned} \tag{5.3}$$

where t^a represents the eight generators of the $SU(3)$ algebra.

The Feynman rules for QCD [91] can be derived from equations 5.2 and 5.3. The resulting Feynman rules are summarized in Appendix A.

Quarks are fermions and a fundamental constituent of matter. They combine to form composite particles called hadrons. The quarks which determine the quantum numbers of hadrons are called constituent or valence quarks. There are six types of quarks, known as flavours: up (u), down (d), charm (c), strange (s), top (t) and bottom (b). Quarks carry a fractional electric charge of value, either$-1/3$ or $+2/3$ times the elementary charge (where the electron has -1 unit), depending on flavour. Up-type quarks, u, c and d have a charge $+2/3$, while down-type quarks, d, s and b have charge $-1/3$.

Quarks and gluons, also known as partons also possess a property called colour charge. The colour-charge is the analog of electric charge in Quantum Electrodynamics(QED). However, unlike electric charge, which is a scalar quantity, the colour-charge is a quantum vector charge, a concept similar to angular momentum in quantum mechanics. The quarks have three basic colour-charge states, red, green, blue and also the corresponding anti-colours for anti-quarks. Colour-charged particles (such as quarks and gluons) cannot be directly observed. This phenomenon is called colour confinement and forces partons to clump to gather and form colour-less particles called hadrons.

The strong forces between colour-charged quarks are mediated by gauge particles called gluons. A simple way to understand this is that the gluons in strong interactions play the role of photons in QED, which mediate electromagnetic interactions between charged currents. Just like photons, gluons are massless, spin-1 particles with two polarization states.

In QED, the vacuum surrounding an electron is filled with virtual e^+e^- pairs. The charge of the electron polarizes the vacuum as the virtual electrons are repelled and the virtual positrons are attracted. In this way the "bare" charge of the electron is screened. This phenomenon is called vacuum polarization. Thus, the charge of the electron observed in the laboratory is smaller than its "bare" charge. An example of vacuum polarization is the electromagnetic interaction between two electrons, as shown in figure 5.1 (b) and (c). The quantum vacuum polarization effectively reduces the strength of the interaction.

The problem with the loop diagrams shown in figure 5.1 is that the momentum of the intermediate particle in the loop (or bubble) can take any value according to Uncertainty Principle; as it is an internal particle. Computation of diagram shown in figure 5.1(b) involves not only an extra power of coupling constant, α, but also an integration over the possible values of the loop momentum k over the momentum phase space $\int dk^4$. This results in a con-

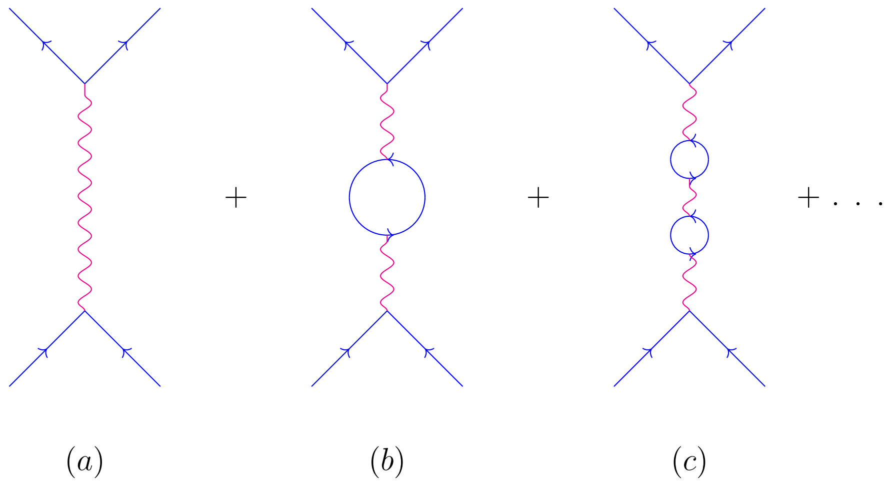

Figure 5.1: (a) First order Feynman diagram of electron-positron pair production via a photon mediator. Diagrams (b) and (c) show the same process in higher order with one loop and more.

tribution proportional to $\int \frac{dk^2}{k^2}$. We can introduce an arbitrary ultraviolet (UV) cut-off[20] λ^2 to eliminate the ultraviolet divergence, however, this only makes the divergence logarithmic. The bubble contribution becomes proportional to $\int \frac{dk^2}{k^2} = ln(\frac{\lambda^2}{Q^2})$, where the other momentum scale, Q^2, comes from the virtuality of the space-like exchanged photon (the off-shellness of the photon propagator), $q^2 = -Q^2$.

There are many virtual diagrams which can contribute to electron-positron scattering, an example is shown in 5.1. However, the first order diagram, the one-loop and multiple successive one-loop along the propagator diagrams contribute most to the cross-section. To achieve physically meaningful results from the calculation of such diagrams, we need to compute the cross-section in terms of an effective coupling α_{eff} as a function of scale Q^2. If we call the bare value of the original coupling constant α_{bare}, which is not directly observed,

[20]The effective coupling is not sensitive to the UV cut-off

the relationship between α_{eff} and α_{ebare} can be deduced as follows:

$$\alpha_{eff}(Q^2) = \alpha_{bare}(1 + \alpha_{bare}B(Q^2) + (\alpha_{bare}B(Q^2))^2 + ...) = \frac{\alpha_{bare}}{1 - \alpha_{bare}B(Q^2)}, \tag{5.4}$$

where $B(Q^2)$ is the bubble contribution to the photon propagator. As we mentioned previously, the bubble contribution is proportional to $ln(\frac{\lambda^2}{Q^2})$. Therefore, as $\lambda \to \infty$, the divergence problem appears. However, we can rewrite everything in terms of the observed value $\alpha_{eff}(Q^2 = \mu^2)$ at a known reference scale μ^2 which for QED can be taken as zero or small value like electron rest mass. Therefore, we get:

$$\frac{1}{\alpha_{eff}(Q^2)} = \frac{1}{\alpha_{eff}(\mu^2)} - (B(Q^2) - B(\mu^2)) \tag{5.5}$$

The actual lowest order result for the QED running coupling is:

$$\alpha_{eff}(Q^2) = \frac{\alpha_{eff}(\mu^2)}{1 - \beta\alpha_{eff}(\mu^2)ln\frac{\mu^2}{Q^2}} \tag{5.6}$$

In QED, the β function takes the positive value of $\frac{1}{3\pi}$. Details of this calculation can be found in [81]. Therefore, in QED, as Q^2 increases $\alpha_{eff}(Q^2)$ decreases. This is similar to the vacuum polarization phenomena in which the charge of electron appears smaller when probed from longer distance.

The same analogy can be applied to the colour-charge of a quark. Similar to QED, in QCD, the vacuum state is not an empty space. However, in this case, the vacuum consists of the virtual quark-antiquark pairs and also virtual gluon pairs, as indicated in figure 5.2. This occurs due to the gluon

Figure 5.2: The two lowest order diagrams of QCD vacuum polarization. The first diagram is shared by QED and QCD. The quark-anti loop interaction has a screening effect because of the positive β-function. The second diagram arises from the interaction between gluons in QCD and has the anti-screening effect, which makes the coupling weaker at a short distance.

self-coupling interaction. In the vacuum state of QCD, quark-antiquark pairs cause the screening effect due to the quark-loop positive β-function. On the other hand, the gluon pairs have an anti-screening effect due to the gluon-loop negative β-function. Once the negative contribution is larger than the positive contribution, the effective β-function is negative which means the vacuum polarization causes an anti-screening effect. This anti-screening effect causes the asymptotic freedom phenomenon which indicates that at short distances, equivalently at large momentum transfer, the effective coupling constant of strong interaction vanishes. In other words quarks do not interact at all between themselves at very short distance.

In QCD, the lowest order of β function is $\beta_{QCD} = -11N_c + 2N_f$ where $N_c = 3$ represents the number of colour-charges and N_f is the number of the light quark flavours at the scale Q^2. Therefore, QCD is asymptotically free ($\beta_{QCD} < 0$) if there are 16 or fewer flavours of quarks.

After renormalization, the coupling constant of QCD can be shown to have the following scale-dependence [91]:

$$\alpha_S(Q^2) = \frac{\alpha_S(\mu^2)}{1 + \frac{11N_c - 2N_f}{12\pi}\alpha_S(\mu^2) ln\frac{\mu^2}{Q^2}} \tag{5.7}$$

In QCD, the parameter Λ_{QCD} is called the QCD scale which is the energy scale below which quarks, antiquarks, and gluons would no longer exist as separate components of a plasma but as quark bound states, forming the lighter hadrons. Because at scale $Q = \Lambda_{QCD}$, $\alpha_S(Q^2)$ diverges to infinity, using equation 5.7, Λ_{QCD} can be written as:

$$\Lambda_{QCD} = \mu^2 exp(\frac{-12\pi}{(11N_c - 2N_f)\alpha_S(\mu^2)}) \tag{5.8}$$

Now, we can rewrite the strong coupling constant at scale Q^2 in terms of QCD scale as follows:

$$\alpha_S(Q^2) = \frac{12\pi}{(11N_c - 2N_f)ln\frac{\Lambda^2_{QCD}}{Q^2}} \tag{5.9}$$

The consequence of the asymptotic freedom of QCD is that the perturbative approach behaves well at higher energy scales, $Q^2 \gg \Lambda^2_{QCD}$, due to the effective coupling constant decreasing.

However, equation 5.9 is not valid when $Q^2 \leqslant \Lambda^2_{QCD}$, since, at the energy scale around Λ^2_{QCD} the running coupling of the strong interaction becomes infinite. In chapter 6, we will talk more about higher orders of coupling constant and the running coupling in the non-perturbative region.

5.2 Diffraction

Generally, in hadron-hadron scattering, interactions can be classified as either elastic or inelastic by the characteristic signatures of the final states. The elastic scattering occurs where the two scattered particles are the only particles involved in the interaction and no other final state particles were produced. This means that the kinetic energy of the two initial particles is unaltered and only the kinematics of the two outgoing protons is changed. About 24% of the total amount of interactions at the LHC correspond to elastic events. The inelastic interaction occurs where the kinetic energy of the initial particles is not conserved, and the result is the creation of a multi-particle final state.

Furthermore, it is conventional to divide inelastic processes into diffractive and non-diffractive parts. In about 55% of all events colour exchanges between the particles result in the multi-particle final states which are called non-diffractive events. In contrast, diffractive processes involve the exchange of one or two colour-less objects, the pomeron (colour-singlet), which allows the interacting protons to remain intact. The pomeron carries the quantum numbers of the vacuum.

Diffractive events at hadron colliders can be classified into the following categories: single, double, and central diffraction (also known as Double Pomeron Exchange), and also higher order multi-pomeron processes, as shown in figure 5.3.

Single diffraction happens when one of the initial protons emerges as a final state particle, but with an energy loss, and the other initial protons breaks up into a multi-particle state travelling in roughly the same direction as the initial particle in the forward region. It means that in the final state of single diffraction which consists of one of the initial protons and a system of new particles, a region empty of particles will be observed which is called rapidity gap, as shown in figure 5.3. Single diffractive events correspond to about 14% of all collisions at the LHC.

In double diffraction, depicted in figure 5.3, both initial particles break up into multi-particle states, as the result of a colour-less exchange with vacuum quantum numbers. The two systems are produced in two distinctive regions, almost at the same direction as the initial particle in the forward region. It means that in the final state of double diffractive process a space empty of particle would appear between the remnant of the the two protons empty of particle and that is called rapidity gap. This type of diffraction correspond to 10% of all events.

One may consider a process in which the protons do not break up and the full pomeron energy goes into the hard state. Such a process is called central exclusive diffractive (CED) production. This occur as the result of an interaction of pomerons from each of the initial protons. This means that the initial particles remain unchanged, except for a loss of energy and changed kinematics. In addition, the two colliding pomerons produce a massive central state. Each of these three systems, the two initial particles and the central state, are separated distinctly from the others by two Rapidity Gaps. About 1% of all events are expected to be Central diffractive events. Finally, the total cross-section of hadron-hadron collision can be written as the following series:

$$\begin{aligned} \sigma_{tot} &= \sigma_{el} + \sigma_{inel} \\ &= \sigma_{el} + \sigma_{non-diff} + \sigma_{diff} \\ &= \sigma_{el} + \sigma_{non-diff} + \sigma_{SD} + \sigma_{DD} + \sigma_{DPE} \end{aligned} \tag{5.10}$$

where SD and DD are single and double diffraction evens, respectively and

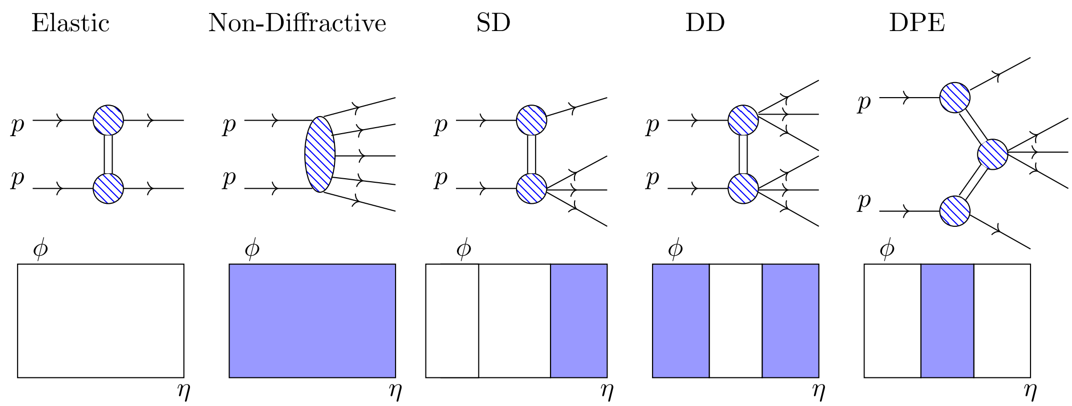

Figure 5.3: Event topologies in η vs ϕ for elastic and diffractive p-p interactions. Shaded areas represent particle production region and empty areas show rapidity gap regions.

DPE corresponds to the Double Pomeron Exchange. Figure 5.3 shows the Feynman diagram of all the different interactions in hadron-hadron collisions.

Diffractive events are signified by a large gap in the pseudo-rapidity distribution of final state particles. A rapidity gap can be defined as the difference between the rapidity of the diffractively scattered proton and that of the particle closest to it in pseudo-rapidity. The size an number of rapidity gaps determine the type of diffractive process. From the experimental point of view, rapidity gaps should ideally be defined by a total absence of particles in a particular interval of pseudo-rapidity. In the next section we will talk about probability that the rapidity gaps survive soft and semi hard rescattering effects.

5.3 Survival Probability of Large Rapidity Gap

The exchange of a gluon or a quark between two hadrons at high energies leads to events in which, in addition to all the hard scattering may have occurred, the entire rapidity space can be filled with soft particles. Such underlying events will spoil the so-called rapidity gap which serves as a signature of diffractive events.

The absence of QCD radiation and the soft interactions between the colliding interaction that leads to particle production can guarantee the survival of the diffractive event and consequently the survival of rapidity gaps. However, all these effects results in a suppression of the cross-section as compared to the hard scattering process alone. The survival probability of a rapidity gap is affected by the Sudakov Form Factor [102], which is the probability not to emit bremsstrahlung gluons. The Sudakov Form Factor will be discussed in more details below.

The so-called Rapidity Gap Survival Probability (RGSP) encodes the probability that no additional particles are produced by accompanying soft proton-proton interactions. The survival factor is not a simple multiplicative constant, but rather depends quite sensitively on the outgoing proton transverse momenta; loosely speaking, as the transverse momentum decreases, or equivalently, as the colliding protons become more separated in impact parameter, the additional secondary particle production will fill the gap.

The gap can be filled by the secondary rescattering caused by the rescatterings of the two incoming protons or the protons with the intermediate partons.

These effects are described by the so-called Eikonal survival factor$< S^2_{eik} >$ and enhanced survival factor $< S^2_{enh} >$, respectively. The precise size of the enhancement effect which is the suppression caused by the rescatterings of the protons with the intermediate partons is uncertain. But due to the relatively large impact parameter in the peripheral collision, it is only expected to suppress the corresponding cross-section by a small factor, much weaker suppression than in the case of the Eikonal survival factor [99]. Due to this uncertainty, the enhancement effect is omitted entirely in this study.

To calculate the Eikonal survival factor, first, we must add the rescattering amplitude $\mathcal{M}_{res}$ to the bare amplitude (with no rescattering) $\mathcal{M}$ as shown in figure 5.4.

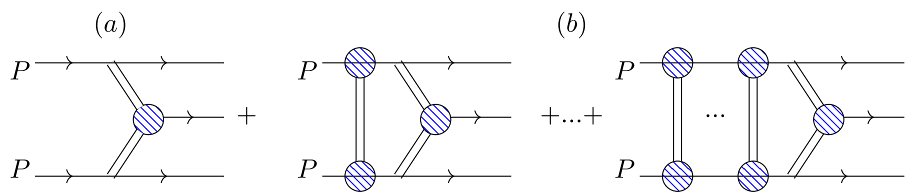

Figure 5.4: The effective amplitude, $\mathcal{M}_{eff}$, of a diffractive event is the summation of its bare amplitude, $\mathcal{M}$, shown in Feynman diagram in figure (a), with all the higher order rescattering amplitudes $\mathcal{M}_{res}$, shown in figure (b).

Therefore, the RGSP is given by:

$$\Big\langle \mid S^2 \mid \Big\rangle = \frac{\int \big(\mathcal{M}(s, p_{1\perp}, p_{2\perp}) + \mathcal{M}_{res}(s, p_{1\perp}, p_{2\perp})\big)^2 d^2p_{1\perp} d^2p_{2\perp}}{\int \mathcal{M}^2(s, p_{1\perp}, p_{2\perp}) d^2p_{1\perp} d^2p_{2\perp}} \tag{5.11}$$

where the integral is over the transverse momentum of the exchanged pomerons, $p_{1\perp}$ and $p_{2\perp}$. In transverse momentum space, the amplitude including rescattering corrections is calculated by integrating over the transverse momentum $K_\perp$ carried round the pomeron loop, as follows:

$$\mathcal{M}_{res}(s, p_{1\perp}, p_{2\perp}) = \int d^2K_\perp \mathcal{M}_{elas}(s, K_\perp^2)\mathcal{M}(s, p_{1\perp} - K_\perp, p_{2\perp} + K_\perp) \quad (5.12)$$

The elastic scattering amplitude, $\mathcal{M}_{res}$, in transverse momentum space is related to the opacity $(\Omega(b, s))$(eg optical density), or equivalently the mean number of rescatterings $(< n(b, s) >)$ in impact parameter space (b) space as explained in Appendix B,

$$\mathcal{M}_{elas}(s, K_\perp^2) = 2s \int e^{-iq.b}(1 - e^{-\Omega(b,s)})^2 d^2b = 2is \int e^{-iq.b}(1 - e^{-\Omega(b,s)})^2 d^2b \quad (5.13)$$

where $q = p_{1\perp} - p_{2\perp}$ is the momentum transfer.

When one ignores any internal structure of the proton, a diffractive event occurs when the spectator systems of the two protons do not interact inelastically. Therefore, the RGSP which determines the fraction of surviving diffractive events, is given by the following equation derived from equation 5.13 and 5.11 in the impact parameter space (b):

$$\left\langle \mid S^2 \mid \right\rangle = \frac{\int \mathcal{M}^2(s, b_1, b_2)e^{-\Omega(s,b)}d^2b_1 d^2b_2}{\int \mathcal{M}^2(s, b_1, b_2)d^2b_1 d^2b_2} \qquad b = b_1 + b_2 \quad (5.14)$$

where $\mathcal{M}(s, b)$ is the Fourier conjugate of the elastic amplitude, $\mathcal{M}_{elas}(s, K_\perp^2)$, in the impact parameter space and $e^-\Omega(b, s)$ is called Eikonal function which represents the probability that two hadrons pass through each other at impact parameter b without any detectable additional inelastic interaction which will populate the gap.

Note that the above equation is only valid in the simplest "one-channel" model, which ignores any internal structure of the proton.

It is assumed that both $\mathcal{M}^2(s, b_{1t}, b_{2t})$ and $e^{\Omega(b_t)}$ are well approximated by a Gaussian distribution in the b-space [78]. The distribution of $\Omega(b, s)$ is given by the following equation:

$$\Omega(b, s) = \nu(s) e^{-\frac{b^2}{R(s)^2}} \tag{5.15}$$

The gaussian expressions of opacity allow us to express the physical observables of interest as functions of $R(s)$ and $\nu(s)$ which are the constants of the model used to fit the experimental distribution. The determination of these variables enables us to produce a global fit to the total, elastic and diffractive cross-sections.

After substituting $\Omega(b, s)$ in the equation 2.7 (appendix B), the total, elastic and inelastic cross-sections can be expressed in terms of R(s) and $\nu(s)$ as follows:

$$\begin{aligned}
\sigma_{tot} &\approx 2\pi R^2(s) ln[\nu(s)] + C - e^{-\nu(s)} \\
\sigma_{inel} &\approx 2\pi R^2(s) ln[2\nu(s)] + C - Ei(-2\nu(s)) \\
\sigma_{el} &\approx 2\pi R^2(s) ln[\frac{\nu(s)}{2}] + C + e^{-2\nu(s)} - 2e^{-\nu(s)}
\end{aligned} \tag{5.16}$$

where $E(x)$ is the integral exponential function $E(x) = \int_{-\infty}^{x} \frac{e^t}{dt}$, and C is the Euler constant, $C = 0.5773$.

The values for $R(s)$ and $\nu(s)$ can be extracted from the experimental data, using the expressions for σ_{tot} and σ_{el} given in equation 5.16.

There are other models that describe the Eikonal function and total cross-section which all result in different RGSPs. Gostman and *et. al.* [86] have studied some of these models with the assumption that that the internal structure of the proton can be ignored. Their results are summarized in table 5.1, where the Eikonal function, ν, R^2, σ_{tot} and $< |S|^2 >$ are listed. These values obtained from the fits to the $p-p$ and $p-\bar{p}$ cross-sections.

The first four models listed in table 5.1 assume that the projectile particles have no substructure, and hence only take into account rescatterings between the colliding protons. However, in the "GLM 2-Channel" [88] and "KKMR 2-Channel" [89] models, the inelastic diffractive intermediate rescatterings are included as well. Therefore, equation 5.14 needs to be modified for these models to include a projectile with substructure.

Inelastic diffraction is a consequence of the internal structure of the protons. At high energies, each constituent of the proton can undergo scattering and thus the outgoing superposition of states will be different from the incident particle, so we will have inelastic, as well as elastic, diffraction.

Now let us consider simple two-channel diffraction. Besides the pure elastic two-particle intermediate states shown in figure 5.5(a), there is the possibility of proton excitation, $p \to N^*$, shown in figure 5.5(b). The diffractive eigenstates can be expressed as the superposition of its two channels, $|p\rangle$ and $|N^*\rangle$, as follows:

$$|i\rangle = \frac{1}{\sqrt{2}}(|\,|p\rangle + |N^*\rangle) \qquad |j\rangle = \frac{1}{\sqrt{2}}(|\,|p\rangle - |N^*\rangle) \tag{5.17}$$

However, note that if both channel $|p\rangle$ and $|N^*\rangle$ of the incoming diffractive state $|i>$ were absorbed equally then the diffracted superposition would be proportional to the incident one and again the inelastic diffraction would be zero as if the projectile had no substructure. Details of this calculation can be found in [89]. So, equation 5.14 is still valid for the two-channel diffraction only Ω will be substitute by matrix Ω_{ij} .

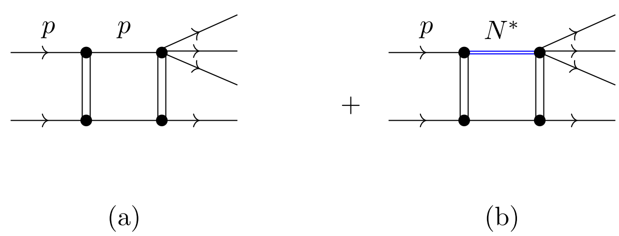

Figure 5.5: The double pomeron exchange contribution to a single diffractive production in the simple two-channel model.(a) Only elastic interaction can happen (b) the intermediate interaction can be inelastic as long as the final interaction is inelastic. Black parallel lines represent the pomeron exchange.

Finally the survival probability can be express as follows:

Probability of the proton P to be in diffractive estate i

Average over diffractive estates i, j

Survival factor with respect to the soft $i - j$ interaction

$$\left\langle \mid S^2 \mid \right\rangle = \frac{\sum_{i,j} \int d^2b |a_{Pi}|^2 |a_{jP'}|^2 \mathcal{M}^2_{i,j} e^{-\Omega_{i,j}(s,b)}}{\sum_{i,j} \int d^2b |a_{Pi}|^2 |a_{jP'}|^2 \mathcal{M}^2_{i,j}}$$

Integral over phase space b

Hard scattering amplitude

More details about Opacity in these two models, “KKMR” and “GLM 2-channel”, can be found in [88, 89].

Recently, PYTHIA was used to estimate gap survival probabilities for the case of central exclusive Higgs production [90]. The models employs the Eikonalization [21] of the partonic cross-section in hadronic collisions can be combined with any hard sub-process to describe the additional production of hadrons due to secondary partonic scatterings. The gap survival probability estimated using PYTHIA is 2.6% for the LHC at the centre of mass energy of 14 TeV. This is remarkably close both to the values used in “KKMR” and to the “GLM 2-channel” values presented in table 5.1.

[21] Using the Eikonal function to describe the cross-section.

Model	$\Omega(s,b)$	$\sqrt{s}$ (TeV)	ν	R^2 (GeV^{-2})	σ_{tot} (mb)	$\langle\lvert S\rvert\rangle^2$ (%)
Minijet	$w_{ij}(b)\sigma_{ij}^{QCD}(s)$ [22]	16	3.9	22.6	107	5.5
Lipatov 1	$\frac{a_1 s^{a_2}}{lns^{a_3}} e^{-\frac{b^2}{R^2(s)}}$ [23]	16	2.69	28.02	113	8.2
Lipatov 2	$\frac{a_1 s^{a_2}}{lns^{a_3}} e^{-\frac{b^2}{R^2(s)}}$	16	2.24	32.66	115	9.2
Dual parton	$\frac{\sigma_S}{8\pi R_S^2} e^{-\frac{b^2}{R_S^2}} + \frac{\sigma_H}{8\pi R_H^2} e^{-\frac{b^2}{R_S^2}}$	16	2.23	32.67	109	5.3
GLM 2-channel	$\Omega_{i,j} = \frac{2\nu_{i,j}}{\pi R_{i,j}^2} e^{-\frac{2b^2}{R_{i,j}^2}}$	14	-	-	103.8	2.7
KKMR 2-channel	[89]	14	-	-	-	2.4-2.6

Table 5.1: Parameters and predictions of different models [88]

5.4 Proton Structure and Evolution Equation

5.4.1 Deep Inelastic Scattering

As mentioned earlier, the fact that asymptotic freedom is observed allows processes with sufficiently large energy scale to be treated like perturbative cases. In the framework of the parton model, perturbative calculations deal directly with quarks and gluons rather than with the hadronic states observed experimentally.

Unfortunately, the parton distribution function inside a hadron cannot be explicitly calculated because it is a non-perturbative quantity in QCD. Hence, the parton distribution function from a set of experiments at some momentum transfer scale and its evolution to other momentum transfer scale calculated using the Dokshitzer-Gribov-Lipatov-Altarelli-Parisi (DGLAP) evolution equations.

The partonic structure of a nucleon is best probed in scattering processes like Deep Inelastic Scattering (DIS). The DIS is a process in which a lepton scatters off a nucleus by transferring large amounts of energy to the nucleon via the exchange of a high energy boson with high virtuality. Figure 5.6(a) shows a DIS process. The whole point of studying the DIS process is that leptonic part and QED interactions, which are well understood, are used to probe the hadronic part of the process.

The kinematics of the DIS can be explained by the two main kinematical variables: Q^2 the virtuality of the photon that is the negative square of the 4-momentum transferred to the hadron ($Q^2 = -q^2$); and, the Bjorken variable x, given by the fraction of the proton momentum carried by the parton struck by the virtual photon. These two variables are related via the centre-of-mass energy of the process, $s = \frac{Q^2}{x}$.

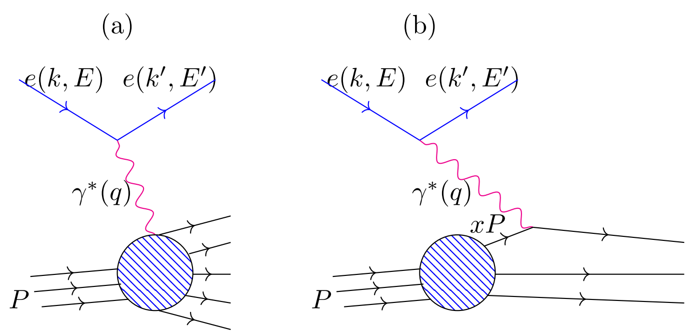

Figure 5.6: (a) Deep inelastic electron-proton scattering of an electron from a proton, (b) Deep inelastic scattering of an electron from a quark constituent of the proton in the parton model.

The DIS amplitude factors into the convolution of a perturbatively short-distance contribution, known as leptonic tensor $\mathcal{L}^{\mu\nu}$, and the non-perturbative long-distance contribution, known as hadronic tensor $W_{\mu\nu}$. The amplitude of the DIS is given by the following equation:

$$\mathcal{M}^2 = \frac{e^2}{Q^4} 2\pi m_N \mathcal{L}_{\mu\nu} W^{\mu\nu} \tag{5.18}$$

The leptonic tensor is trivial to compute as the leptons are point-like fermions and it can be expressed by the following equation:

$$\mathcal{L}^{\mu\nu} = 4k^\mu k^\nu - 2q^\mu k^\nu - 2k^\mu q^\nu + g^{\mu\nu} q^2 \tag{5.19}$$

where k and q are the 4-momentum of the electron beam and the transferred photon, respectively, and $g^{\mu\nu}$ is the metric tensor.

Unlike the leptonic tensor, the partonic tensor $W^{\mu\nu}$ cannot be computed directly from QCD because of its non-perturbative character. The most general form of the hadronic tensor $W^{\mu\nu}$ is constructed out of $g^{\mu\nu}$ and independent momentum of proton p and photon q: (see [100], chap. 8 and 9 for more details.)

$$W^{\mu\nu} = W_1(q^2, p.q)[-g^{\mu\nu} + \frac{q^\mu q^\nu}{q^2}] + \frac{W_2(q^2, p.q)}{m_N^2}[p^\mu - \frac{p.q}{q^2} q^\mu][p^\nu - \frac{p.q}{q^2} q^\nu] \tag{5.20}$$

This decomposition of $W^{\mu\nu}$ introduces the two independent arbitrary structure functions W_1 and W_2 which have the same dimension.

We use the Mandelstam variables which are defined as $s = (p+k)^2$, $u = (p-k')^2$, $t = (k-k')^2$, and the Bjorken variable x, to simplify the cross-section of electron-hadron interaction. Here, k, k' and p represent the 4-momenta of the incident electron, the scattered electron and the proton, as shown in figure

5.6. After algebraic manipulation, the result of the simplified cross-section can be written as flowing:

$$(\frac{d\sigma}{dtdu})_{eP\rightarrow eX} = \frac{4\pi\alpha^2}{t^2s^2}\frac{1}{s+u}[(s^2+u^2)xF_1+usF_2] \tag{5.21}$$

where the form factors $W_1(\nu, Q^2)$ and $W_2(\nu, Q^2)$ are expressed through the unpolarized structure functions $F_1 = M_pW_1$ and $F_2 = \nu W_2$ with $\nu = E - E'$. M_p represents the mass of proton, E and E' represent the energy of the incident electron and the scattered electron, respectively.

The simplest structure that can be considered for a proton is 3 point-like quarks. At high energies, the partons can be thought of as independent point-like particles (no correlation with each other) which are moving in the direction of the hadron carrying a longitudinal fraction of its momentum x. Therefore, the cross-sections can be expressed through the sum of all partonic contributions to the hadron. The cross-section of a partonic process can then be easily calculated using perturbative theory (Feynman diagrams). This model is shown in the DIS process in figure 5.7.

To describe the hadronic cross-section a term called Parton Distribution Functions (PDFs) is introduced, reflecting the probability of finding a quark of type q with momentum fraction x of the proton in the proton. Using the factorization method the inelastic electron-proton cross-section is explained by the convolution of elastic electron-parton scattering and the PDF, $f_q(x)$, integrated over all possible x and summed over all possible q's, as follows:

$$(\frac{d\sigma}{dtdu})_{eP\rightarrow eX} = \sum_q \int_x dx f_q(x)(\frac{d\sigma}{dtdu})_{eP\rightarrow eq} \tag{5.22}$$

Thus, if we substitute the well-known cross-section of elastic scattering of $eP \to eq$ in the above equation then the hadronic cross-section of the DIS can be expressed as:

$$(\frac{d\sigma}{dtdu})_{eP\to eX} = \sum_q \int_x dx f_q(x) \frac{2\pi\alpha^2 e_q^2}{t^2 s^2}[(s+u)^2 - 2su]\delta(t + x(s+u)) \quad (5.23)$$

Comparing the two equations 5.23 and 5.21 yields the following relation between structure functions and the PDF.

$$2xF_1(x) = F_2(x) = \sum_q x e_q^2 f_q(x) \quad (5.24)$$

$f_q(x)$ is the probability that the struck parton q carries the fraction x of proton's momentum p. Therefore, the dimensionless structure function of the proton, with momentum fraction x and charge e_q is $F_2(x') = \sum_q \int dx e_q^2 x f_q(x) \delta(x - x')$ which is independent of the virtuality of the photon, Q^2.

When one abandons the concept of point-like partons and adopts the field theory concept of "dressed" particles [24], the first step is to consider the NLO correction to equation 5.22. Or, in more physical terms, consider that the quarks participating in the interactions can branch and emit gluons.

The probability of one gluon emission with the transverse momentum be-

[24] In QFT, the concept of bare field or point-like particle is replaced with the "dressed" particle where all particles are surrounded by a cloud of fermion-antifermion pairs and gauge bosons.

(a) (b)

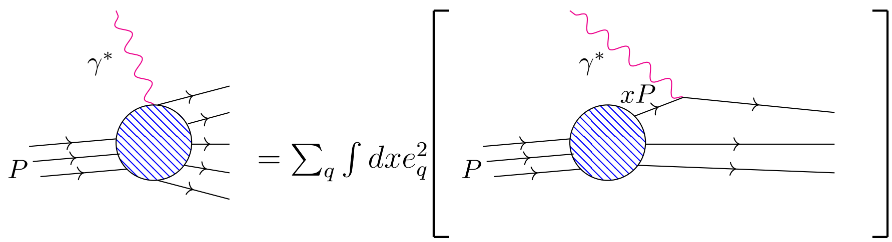

Figure 5.7: (a) The hadronic part of the DIS of an electron from a proton. $\gamma*$ is the emitted virtual photon that interacts with the other beam proton. (b) Under the assumption that proton consist of uncorrelated point-like quarks, the hadronic cross-section of the DIS can can be expressed through the sum of all partonic contribution of the hadron. In this case, the partonic contribution is the DIS of an electron from a quark constitutent of the proton.

tween $k_\perp^2$ and $k_\perp^2 + dk_\perp^2$ is given by:

$$\frac{\alpha_s}{2\pi}\frac{dk_\perp^2}{k_\perp^2}P_{ab}(z)dz \tag{5.25}$$

$P_{ab}(z)$ is the probability that parton a radiates parton b with the fraction z of the original momentum carried by the particle and is called the DGLAP splitting function [115]. The leading order splitting functions and associated diagrams are shown in figure 5.8 for all combinations of quark and gluon emissions [91].

Therefore, when we don't naively assume the parton constituent of the proton are point-like particles, the hadronic cross-section of $\gamma^* q \to qg$ in equation 5.22 could be rewritten in the following format:

$$(\frac{d\sigma}{dtdu})_{\gamma * q \to qg} \propto \int_0^{Q^2} \frac{\alpha_s}{\pi}\frac{dk_\perp^2}{k_\perp^2}P_{ab}(x)(\frac{d\sigma}{dtdu})_{\gamma * q \to q} f(x)dx \tag{5.26}$$

here the cross-section of $\gamma^* q \to q$ is convoluted with the probability of a gluon emission off the quark.

Because the integral $\frac{dk_\perp^2}{k_\perp^2}$ in equation 5.26 diverges at zero, we need to add an arbitrary lower limit, μ, on the transverse momentum of the gluon to regularize the collinear divergence. Then, the PDF function in equation 5.27 can be written as:

$$2xF_1(x,Q^2) = F_2(x,Q^2) = \sum_q \frac{xe_q^2\alpha_s}{2\pi} \int_x^1 \frac{dy}{y} f_q(y,\mu^2)[P_{qq}(\frac{x}{y}) ln\frac{Q^2}{\mu^2}] \tag{5.27}$$

The details of this calculation can be seen in [101].

From the above equation, it is obvious that the PDF function ($f_q(y,\mu^2)$) depends on renormalization scale μ^2 (lower boundary on the transverse momentum of the quark, q^2). However, the structure function ($F_2(x,Q^2)$) is a physical term so it cannot depend on an arbitrarily chosen scales such as μ scale. Thus, $\frac{\partial F_2(x,Q^2)}{\partial ln(\mu^2)} = 0$ which leads to the DGLAP evolution equation that describes the variation of PDF ($f_q(y,\mu^2)$) with μ^2 as follows:

$$\frac{\partial f_q(x,\mu^2)}{\partial ln\mu^2} = \frac{\alpha_s}{2\pi} \int_x^1 \frac{dy}{y} f_q(y,\mu^2) P_{qq}(\frac{x}{y}) \tag{5.28}$$

5.4.2 Generalized Parton Distribution Function

In the previous section we showed that the inclusive cross-section of the DIS process can be written in a factorized form as the convolution of PDFs, which only depend on the momentum fraction x of the struck parton, the scale μ^2, and the parton level cross-section as a function of the Mandelstam variables.

$P_{qq}(z) = C_F[\frac{1+z^2}{(1-z)_+} + 3\delta(1-z)]$ $\qquad$ $P_{gq}(z) = C_F[\frac{1+(1-z)^2}{z}]$

$P_{qg}(z) = T_F(z^2 + (1-z)^2)$ $\qquad$ $P_{gg}(z) = C_A[\frac{1-z}{z)} + z(1-z) + \frac{z}{(1-z)_+}] + \delta(1-z)\frac{11C_A - 4T_F n_f}{6}$

Figure 5.8: Leading order DGLAP splitting functions. $C_F = \frac{4}{3}$, $C_A = 3$, and $T_F = \frac{1}{2}$ are the QCD color factors

However, for less inclusive processes a treatment in terms of conventional PDFs cannot necessarily be directly applied. One interesting example of this is the class of elastic hadronic processes, such as Central Exclusive Production of Higgs boson $p+p \to p+H+p$, or Deeply Virtual Compton Scattering (DVCS). These type of processes are described in terms of so-called Generalized Parton Distribution Functions (GPDs), $H_{q,g}(x, \xi, \mu^2, t)$ [25]. In this process, we cannot use the naive point-like incoherent parton model to describe hadrons. Instead, GPDs express the coherence between the state of initial parton which carries a fraction $x+\xi$ of the nucleon momentum and the state of final parton carrying a fraction $x-\xi$ of the nucleon momentum, at the given values of t and Q^2. The Bjorken variable x and the skewness parameter ξ, where $\xi = \frac{x_B}{2-x_B}$ in the Bjorken limit, describe the momentum fractions carried by the emitted and absorbed partons and $t = (p_1 - p_2)^2$ is the momentum transfer between the two hadrons.

[25] t is the transverse momentum

However, under the condition that $Q^2 >> \mu^2$ and $Q^2 >> t$, factorization in the DVCS and the DIS are quite similar, with the exception that the cross-section factorization is written in terms of the corresponding skewed[26] GPDs instead of conventional PDFs. Also, in the limit $t \to 0$ and $\xi \to 0$ the skewed distributions will reduce to the conventional PDFs:

$$\begin{aligned} H_q(x, 0, 0) &= q(x) \\ H_q(-x, 0, 0) &= -\overline{q}(x) \\ H_g(x, 0, 0) &= xg(x) \end{aligned} \tag{5.29}$$

Due to the low cross-section of elastic hadronic processes, direct determination of the skewed parton distributions function with a high accuracy is not possible. Moreover, GPDs depend on four variables x, ξ, t and μ^2 which make the situation more complicated. Shuvaev and et al. [113] have demonstrated how, in small $\xi << 1$ region (for $t \to 0$), the skewed GPDs are determined in terms of the small x behaviour of the conventional PDF which is known from experiment as demonstrated by Shuvaev et al.[113].

The skewed distribution function depends on the momentum transfer t between the two hadrons. However, in the limit that $|t| << \mu^2$, the t dependance of the skewed distribution function is typically assumed to factorize from the longitudinal momentum dependence as a form factor $F(t)$. We will assume this to be the case in what follows, omitting the t dependence for simplicity. Thus, $H(x, \xi, \mu^2; t) = H(x, \xi, \mu^2)F(t)$.

Therefore, we can write the skewed distribution function as a convolution

[26] $\xi \neq 0$

of the conventional PDFs with the hard scattering kernels k_q. The Kernel function is the modified DGLAP splitting function that specifies just how much total angular momentum is carried by partons in the hadron. At scale μ^2, the skewed distribution function can be written as:

$$H(x,\xi) = \int_{-1}^{1} dx' k_q(x',\xi) f(x'). \tag{5.30}$$

The splitting kernel $k_q(x,\xi,x')$ is calculated in [119] given by the following equation:

$$k_q(x,\xi,x') = -\frac{1}{\pi|x'|} Im(\int_0^1 ds(1-y(s)x')^{-\frac{3}{2}}) \tag{5.31}$$

where $y(s) = \frac{4s(1-s)}{x+\xi(1-2s)}$ and the imaginary part is defined as $Im(F(x)) = \frac{1}{2i}[F(x+i\delta(x)) + F(x+i\delta(x))]$. When $\xi = 0$, $k_q(x,\xi,x') = \delta(x-x')$ and $H(x,\xi) = q(x)$, as expected.

By substituting the Kernl function in equation 5.30, the equation for GPDs can be expressed as follows:

$$H_q(x,\xi) = \int_{-1}^{1} dx' [\frac{2}{\pi} Im \int_0^1 \frac{ds}{y(s)\sqrt{(1-y(s)x')}}] \frac{dq(x')}{d|x'|} \tag{5.32}$$

The formula for the gluon is slightly different to that for the quarks. The additional x in the gluon reveals itself as an extra factor of $x+\xi(1-2s)$ in the kernel equation.

$$H_g(x,\xi) = \int_{-1}^{1} dx' [\frac{2}{\pi} Im \int_0^1 \frac{ds(x+\xi(1-2s)}{y(s)\sqrt{(1-y(s)x')}}] \frac{dg(x')}{d|x'|} \tag{5.33}$$

In this study, we will consider the GPDs at low-x processes and the skewed regime (for example $x' + \xi = x$ and $x' - \xi = 0$). In this case, the ratio of the skewed distribution $H_i(\frac{x}{2}, \frac{x}{2})$ to the diagonal distribution $H_i(x, 0)$ at momentum fraction x is given by:

$$K_i = \frac{H_i(\frac{x}{2}, \frac{x}{2})}{H_i(x, 0)} = \frac{2^{2\lambda+3}\Gamma(\lambda + 5/2)}{\sqrt{\pi}\Gamma(\lambda + 3 + p)} \tag{5.34}$$

5.5 Central Exclusive Higgs Diffractive (CED) Process

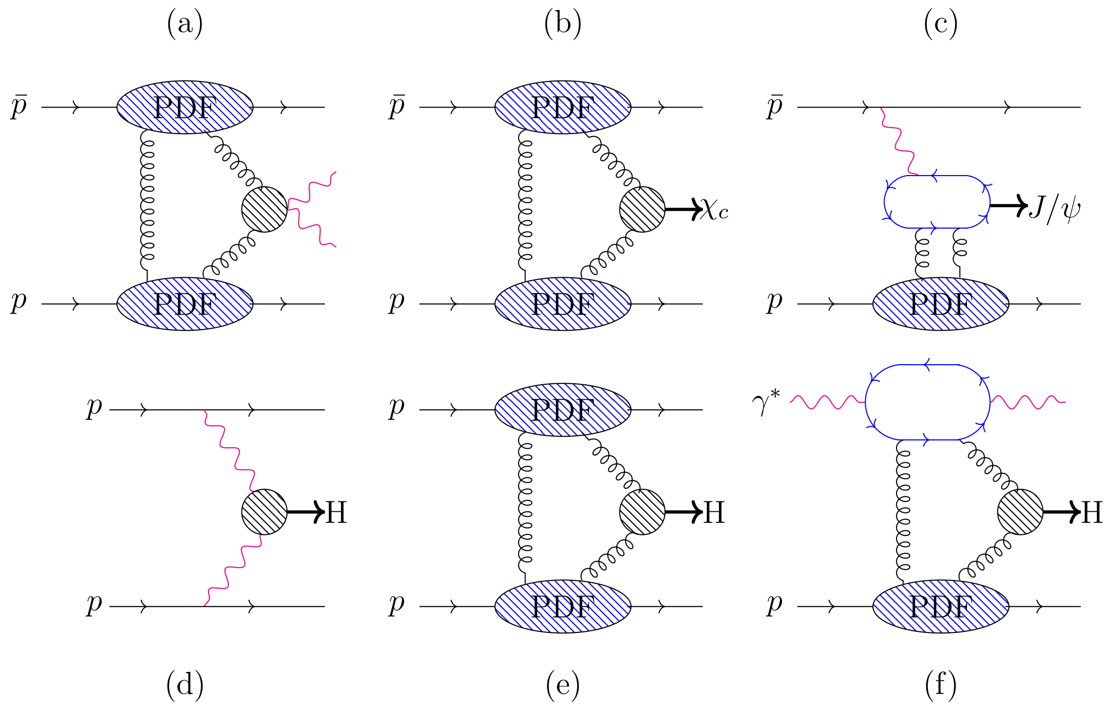

Figure 5.9: The dominant Feynman diagrams for some relavant example CED processes. First row: (a) $p\bar{p} \to p + \gamma\gamma(l^+l^-) + \bar{p}$, (b) $p\bar{p} \to p + \chi_c + \bar{p}$, (c) Elastic photo-production of J/ψ, $p\bar{p} \to p + J/\psi + \bar{p}$, (d) $pp \to p + H + p$, (e) Double Pomeron exchange(DPE), $pp \to p + H + p$, (f) $\gamma p \to \gamma + H + p$.

The CED is defined as $p + p \to p \oplus X \oplus p$ with no radiation emitted between the intact outgoing beam of hadrons and the central system X which are shown by $\oplus$ signs and used to denote the presence of large rapidity gaps. If a large region of rapidity is devoid of particles, only photon and pomeron exchanges are significant as colour-charge exchanges between the two protons cause QCD that act to fill the rapidity gaps.

In the past decade, interest in studies of CED processes in high energy proton-(anti)proton collisions has increased, both theoretically and experimentally. There are some important advantages to study these processes: 1- they provide an especially clean environment in which to probe some processes that are difficult to probe in regular QCD interaction as a result of significant background. 2 - The new forward proton tagging detectors at the ATLAS and CMS can be utilized for investigation of crucial identification issues such as the spin and CP parity and the bb coupling of the newly discovered particles. 3 - They could be used for precise measurement of Higgs boson mass and the studies of heavier Higgs-like particles expected in beyond standard model theories.

It is also worth mentioning that in the CED process, the projection of the total angular momentum of the outgoing protons is $J_z = 0$ along the beam axis. Also due to the conservation of parity, the CED process strongly favours $J_z = 0^+$ quantum numbers for the centrally produced particle state [99].

The dominant Feynman diagrams for some of the CED processes are shown in figure 5.9. The first row of diagrams are the CED processes in $p\bar{p}$ collisions studied by the CDF II detector and the second row shows the CED processes by which Higgs bosons can be produced at the LHC. The $p\bar{p} \to p + \gamma\gamma + \bar{p}$ with the primary process $\mathbb{PP} \to \gamma\gamma$ through a quark loop is shown in figure 5.9

(a). The SM cross-section for this CED process is predicted by Durham group to be $\sigma \approx 1.42$ pb [93] which is compatible within errors of the experimental value taken in Run-2 of CDF $2.48^{+0.40}_{-0.35}(stat)^{+0.40}_{-0.51}(syst)$ [92]. The process $p\bar{p} \to p + \chi_c + \bar{p}$, with the primary process $\mathbb{P}\mathbb{P} \to \chi_c$ is shown in figure 5.9 (b). The predicted cross-section by Durham group is $\frac{d\sigma}{dy}|_{t=0} = 130$ nb [95] and it is in good agreement with the Tevatron result at centre of mass energy of $\sqrt{s} = 2$ TeV [96]. Elastic photo-production of J/ψ, $p\bar{p} \to p + J/\psi + \bar{p}$ with the primary process $\gamma\mathbb{P} \to J/\psi$ through a quark loop, is shown in figure 5.9 (c) . The predicted differential cross-section by Durham group is $\frac{d\sigma}{dy}|_{t=0} = 3.0$ nb [94] and it is measured experimentally, at the CDF at $\sqrt{s} = 2$ TeV, to be $\frac{d\sigma}{dy}|_{t=0} = 3.6$ nb [95]. Process $pp \to p + H + p$ with the primary process $\gamma\gamma \to H$ through a quark loop is shown in figure 5.9 (d). The predicted cross-section at the LHC ($\sqrt{s} = 14$ TeV) is calculated to be 0.18 fb [108]. Double Pomeron exchange (DPE), $pp \to p + H + p$. with the primary process $\mathbb{P}\mathbb{P} \to H$ through gluon fusion is shown in figure 5.9 (e). The Durham Group's prediction for this cross-section at the LHC ($\sqrt{s} = 14$ TeV) is 3 fb [27] [97]. The $\gamma p \to \gamma + H + p$ reaction with the primary process $\mathbb{P}\mathbb{P} \to H$ through gluon fusion is shown in figure 5.9 (f). We have evaluated the cross-section of this process in this thesis.

We have used the Durham formalism [98] to calculate the cross-section of Higgs boson production via Central Exclusive Diffractive "Photo-production" in Ultra-Peripheral Collision(CEDP) and determined the numerical value of the cross-section using the Fortran code (please see chapter 7 for the analytical process and chapter 8 for the blueprint and more details on the Fortran code).

[27] This value is highly dependant on the PDF set choice.

We also have calculated the numerical value of the cross-section of DPE using the same set of code for confirmation.

Chapter 6

"Photoproduction" of Higgs Boson

6.1 Introduction

After the discovery of a scalar state, that looks increasingly like the Standard Model Higgs boson, in 2012 at the LHC, a new era of precision measurement of Higgs boson has begun. In order to make precise measurements of the Higgs sector, it is important to study as many models of Higgs production as possible. Recently there has been growing interest in the study of the Higgs production via CED processes $p+p \to p+\oplus H \oplus p$ which raises the possibility to make an enhanced measurement of the properties of the Higgs boson in a way that is challenging to do using the LHC general purpose detectors alone. For example, the invariant mass of the Higgs boson may be measured directly, and the spin and CP properties of the Higgs boson may be explored via this process [103, 104, 105, 106, 98].

The Durham group [98], E. Papageorgiu [107] and David D'Enteria et al.[108], have explored the possibility of studying the Standard Model Higgs boson in central exclusive diffractive processes, via double pomeron exchange and gamma-gamma fusion, in high-energy proton-proton collisions and in proton-A collisions at the LHC. The basic CED processes, $p+p \to p+\oplus H \oplus p$ and $\gamma\gamma \to \gamma \oplus H \oplus \gamma$, as shown in figure 5.9 (e) and (f). However, a related channel, the photo-production of Higgs boson in CED $p + \gamma^* \to p \oplus H \oplus \gamma^*$, figure 5.9 (g), has not received careful attention, despite the fact that its cross-section is comparable with the two other processes previously mentioned. In this work, we evaluate the Higgs production from $\gamma - \mathbb{P}$ collisions also known as Central Exclusive Diffractive "Photo-production" in Ultra-Peripheral Collision (CEDP in UPCs) and we will discuss the benefits of studying this channel as well as the sources of uncertainties in the cross-section.

According to Fermi [111], the field of a fast charged particle can be interpreted as a flux of photons. In the Central Exclusive Diffractive "Photo-production" of Higgs boson in Ultra-Peripheral Collisions (CEDP in UPC), the photon flux generated by one of the protons/ions interact an impinging proton at large impact parameter, b, via a diffractive photo-production process. Diffractive photo-production in proton-proton collisions refers to a class of processes where a photon (quasi-real photon with low virtuality) emitted from one of the protons, interacts with a QCD colour-singlet gluon state called pomeron, extracted from the other proton. The Feynman diagram for this process is shown in figure 5.9 (g). This process can be factorized in three steps. First, the quasi-real photon with virtuality of Q^2 fluctuates into a $q\bar{q}$ pair. Then, this pair interacts with a pomeron emitted from the other proton. Finally, the Higgs boson is produced via gluon fusion. The additional t-channel gluon, called the screening gluon, screens the colour of the annihilating gluons. For the screening gluon that is not coupled to the Higgs boson, it has to have small virtuality $k_T^2 \ll M_H^2$ in order to enhance the probability of screening.

In this processes, due to the large impact parameter, hadronic interactions are not possible. Therefore, the final state of the events will be characterized by a Large Rapidity Gap (LRG). The LRG leads to a much more cleaner final state with only the Higgs boson in the central detector and much more lower background than in hadronic interactions. After the collision, both incoming protons scatter at very low angles with respect to the beam making it possible to tag them with the AFP detector in the LHC tunnel and reconstruct the mass of Higgs boson accurately based on the energy loss of the protons.

Despite all the advantages, the CED processes have over hadronic interactions, their cross-section is strongly suppressed as only a small percentage of proton-proton interactions are diffractive. Moreover, we must also consider the suppression due to the Rapidity Gap Survival Probability (RGSP). On the other hand, in this specific process we are studying here, if one of the protons is substituted by a heavy ion, the cross-section will be enhanced as a result of "Z^2 effect" arising from the charge of heavy ion (Z).

The goal here is to calculate and study the cross-section of Higgs boson production via CEDP in UPC collisions. In section 2, the amplitude and cross-section of the $p + \gamma^* \to p \oplus H \oplus \gamma^*$ process is evaluated. The parton distribution function that is adopted in this calculation is studied in section 3. Then, in section 4, we describe the secondary scattering suppression of the the cross-section. Lastly, in section 5, we consider the "Z^2" enhancement due to the collision of a proton with the heavy ion.

6.2 From Parton-Level to Hadron-Level Amplitude

To calculate the CEDP cross-section, we use the formalism of the general CED processes in high-energy proton-proton collisions studied by Durham group [98] and the Weizsacker-Williams approximation [109, 110] to determine the flux of equivalent photon which is produced in the UPC.

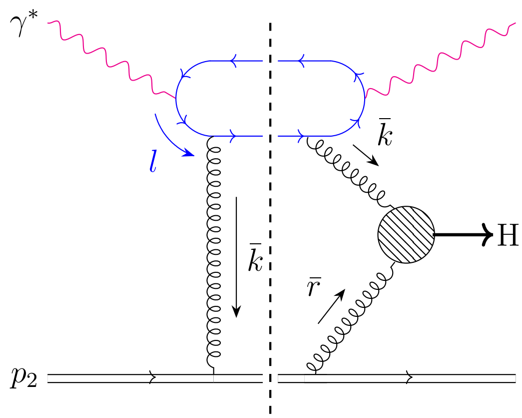

Figure 6.1: Utilization of Cutkosky cutting rules to calculate the imaginary part of the CEDP amplitude. The dotted line indicates the cut which separates the left and right side of the process.

We begin by calculating the imaginary part of the amplitude for the simpler parton-level process, using the Born approximation. Because of the two loops in the Feynman diagram of the process, there would be singularities in the cross-section. To eliminate these singularities, we apply Optical theorem and Cutkosky cutting rules [120, 91], where the cut is made along the dotted line, as shown in figure6.1.

The Optical theorem derived in appendix C leads to the following equation for $p + \gamma^* \to p \oplus H \oplus \gamma^*$ process.

$$Im(\mathcal{M}(\gamma^* p \to \gamma p H)) = -\frac{1}{2} \sum_m \int d\Pi_3 \mathcal{M}(\gamma^* p \to m) \mathcal{M}(m \to \gamma^* p H) \quad (6.1)$$

Where $\mathcal{M}(\gamma^* p \to m)$ and $\mathcal{M}(m \to \gamma^* p H)$ are the amplitude of the left and the right side of the cutting line, respectively, and the summation is over all intermediate states. $\int d\Pi_3$ is the differential phase space of the intermediate propagators which can be simplified to the following equation using simple algebra. More details can be found in appendix D.

$$\int d\Pi_3 = \frac{1}{2\pi^5} \frac{1}{4W^2} \int d\alpha_l d^2\bar{k} d^2\bar{l} \frac{1}{\alpha_l(1-\alpha_l)} \quad (6.2)$$

We can now apply the Sudakov parametrization of momentum for the exchanged gluon (k), exchanged quark in the quark pair loop (l), and the emitted photon (q) as follows:

$$k = \alpha_k p_2 + \beta_k p_1 + k_\perp \quad (6.3)$$

$$l = \alpha_l p_2 + \beta_l p_1 + l_\perp \quad (6.4)$$

$$q = p_2 - x p_1 \quad (6.5)$$

where $0 < \alpha_{k/l} < 1$ and $0 < \beta_{k/l} < 1$ are the sudakov parameteres, $k_\perp$ and $l_\perp$ are the transverse momentum of the exchanged gluon and quark. p_1 is the incoming proton four-momentum, p_2 is the four-momentum of a real photon, $x = \frac{Q^2}{W^2}$ is the the Bjorken scale factor and $W^2 = 2p_1 \cdot q$ is the centre of mass energy of the photon-proton system. Because, a peripheral process is characterized by small values of longitudinal Sudakov parameters $\alpha_{k/l}$ and $\beta_{k/l}$ ($\alpha_{k/l} << \beta_{k/l} << 1$) and the transverse momenta of the order of electron mass, we neglected terms on the order of k^2/W^2. Taking this into account, one obtains the multiplication of the unpolarized amplitude of the left and right side as the following:

$$
\begin{aligned}
\mathcal{M}_1\mathcal{M}_2 &= A\frac{1}{r^2k^4}\Big(\frac{Tr(\Xi_1)}{(l^2-m_q^2)^2} - \frac{Tr(\Xi_2)}{(l^2-mq^2)((q-l-k)^2-mq^2)}\Big) \\
A &= -\frac{\alpha\alpha_s^2}{4\pi^2}\frac{M_H^2\alpha_s}{6\pi v}\sum_q e_q^2\frac{N_c^2-1}{4N_c^2} \\
\Xi_1 &= \Sigma\epsilon_\nu\epsilon_\sigma^*[\gamma^\nu(\not{l}+m_q)\not{p}(\not{l}+\not{k})\not{p}(\not{l}+m_q)\gamma^\sigma(\not{q}-\not{l})] \\
\Xi_2 &= \Sigma\epsilon_\nu\epsilon_\sigma^*[\gamma^\nu(\not{l}+m_q)\not{p}(\not{l}+\not{k})\gamma^\sigma(\not{q}-\not{l}-\not{k}+m_q)\not{p}(\not{q}-\not{l})]
\end{aligned}
\tag{6.6}
$$

Note that the calculation is further simplified by making use of the Eikonal approximation for those vertices which couple the gluons to the external quarks. More details of this calculation can be find in Appendix B.

The amplitude in equation 6.6 can be further simplified by using the standard formula to sum over all the spin states of photons $\Sigma\epsilon_\nu\epsilon_\sigma^* = -g_{\nu\sigma} +$

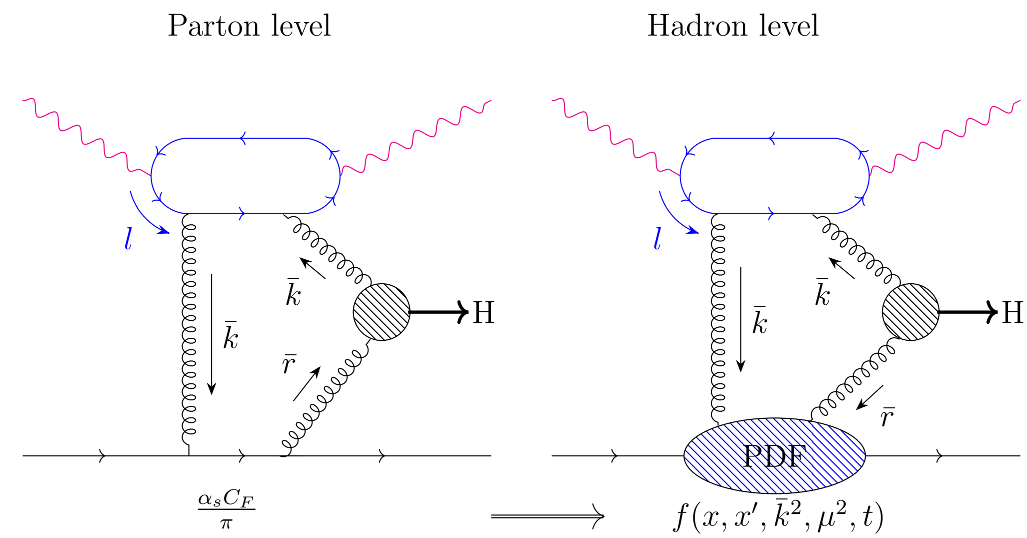

Figure 6.2: Converting parton-level amplitude into the hadron-level amplitude by replacing a factor of $\alpha_s C_F/\pi$ in the amplitude by $f(x, x', \bar{k}^2, \mu^2, t)$.

$4\frac{Q^2}{W^4}p_{1\nu}p_{1\sigma}$ and evaluating the traces. The entire amplitude then becomes:

$$
\begin{aligned}
-i\mathcal{M} =& \frac{4}{3\pi^2}\frac{C_F^2}{N_c^2-1}\frac{\alpha W^2 M_H^2}{v}\int d^2\bar{k}\int_0^1 d\alpha_l\int_0^1 d\tau\alpha_s^3(\bar{k}^2)\sum_q(F_1+F_2)\\
F_1 =& \frac{e_q^2}{\bar{k}^4}\frac{[\alpha_l^2+(1-\alpha_l)^2][\tau^2+(1-\tau^2)]}{\alpha_l(1-\alpha_l)Q^2+\tau(1-\tau)\bar{k}^2+m_q^2}\\
F_2 =& \frac{e_q^2 m_q^2}{\bar{k}^6(\alpha_l(1-\alpha_l)Q^2+\tau(1-\tau)\bar{k}^2+m_q^2)}\big(4(1-\alpha_1+\alpha_l^2)+\frac{2e_q^2\bar{k}^2\tau(1-\tau)(6\alpha_l^2-6\alpha_l+1)}{\alpha_l(1-\alpha_l)Q^2+m_q^2}\big)
\end{aligned}
\tag{6.7}
$$

where the colour factors $C_F = \frac{4}{3}$, $N_c = 3$ is the number of colour charges, α is the QED fine structure constant, α_s is the strong running coupling, W is the CM energy of γ and p, M_H is the mass of Higgs boson, ν is, m_q is the mass of quark, e_q is the charge of quark, $\sum_q$ is the summation over all quarks properties (mass and charge) $\bar{k}^2$ is the absolute value of transverse momentum of exchanged gluon, and Q^2 is the virtuality of emitting photon. More details of this calculation can be seen in Appendix E and F.

To convert parton-level amplitude into the hadron-level amplitude, we must introduce the skewed PDF, in which the momentum of the outgoing proton is not the same as that of the incoming proton, to the amplitude. Following the recipe of general central exclusive production [82], we replaced $\alpha_s C_F/\pi$ (probability of finding a gluons in the proton in the simple three valence quark model) by $f(x, x', \bar{k}^2, \mu^2, t)$ (probability of finding a gluons in the proton in the more realistic model) which, derived from the DGLAP evolution equation for evolution of an initial quark distribution. This process is shown in figure 6.2.

Thus, one obtains the hadron level amplitude as:

$$-i\mathcal{M} = \frac{4}{3\pi}\frac{C_F}{N_c^2-1}\frac{K\alpha W^2 M_H^2}{v}\int d^2\bar{k}\int_0^1 d\alpha_l\int_0^1 d\tau\alpha_s^2(\bar{k}^2)f(x,x',\bar{k}^2,\mu^2,t)\sum_q(F_1+F_2) \tag{6.8}$$

where $f(x, x', \bar{k}^2, \mu^2, t)$ is the unintegrated skewed gluon density [28] of the proton and corresponds to the $x' << x$ limit. Here, $\mu = (\frac{M_H}{2})^2$, $x = \sqrt{M_H^2}/s$ and $x' = \sqrt{k_T^2}/s$ are the momentum fractions carried by the screening and fusing gluons, respectively.

6.3 PDF

As mentioned in chapter 5, in order to define the skewed PDF, a multiplicative factor $K = \frac{f(x,x',\bar{k}^2,\mu^2)}{\frac{\partial xg(x,\bar{k}^2)}{\partial \ln \bar{k}^2}}$, the ratio of the skewed $x' << x$ unintegrated gluon distribution to the integrated conventional density is introduced.

[28] At low-x, the gluon contributes the most.

Therefore, the skewed PDF is evaluated by multiplying the coefficient k by the conventional PDF. For the production of a 125 GeV Higgs boson at the LHC, $K \sim 1.2$ [113, 80]. Also, in the limit that the beam protons scatter at small angles, one can factorize the transverse part of the PDF in form of a Gaussian function, as $\exp(-\frac{B}{2}p_t^2)$, which describes the reduction of the amplitude at higher momentum transfer between the colliding protons at slope B where slope B corresponds to the slope of the electromagnetic proton form factor. In this study we have adopted $B = 4$ GeV^2 which is the slope that is well-measured in diffractive J/ψ electro-production.

The factorization of the PDF function can be written as follows:

$$f(x, x', \bar{k}^2, \mu^2; t) = f(x, x', \bar{k}^2, \mu^2)e^{(-\frac{B}{2}p^2)} \tag{6.9}$$

And eventually, by substituting the skewed PDF with the conventional PDF times factor k in the above equation we have:

$$f(x, x', \bar{k}^2, \mu^2, t) = 1.2e^{(-\frac{B}{2}p_t^2)}\frac{\partial xg(x, \bar{k}^2)}{\partial \ln \bar{k}^2} \tag{6.10}$$

In this work, we used universal integrated gluon distribution functions provided by MSTW08NLO distributions [126] using the fit in Next-to-Leading Order (NLO) in the strong coupling α_s. Further details are given in section 6.6.

6.4 Secondary Particle Radiation Suppression

In the infrared region of $\bar{k}^2$, in equation 6.8, the amplitude diverges. This problem is due to only taking into account the lowest order integral and neglecting virtual loops in the DGLAP equation. This shortcoming can be addressed with the use of a Sudakov form factor, which represents the probability of only emitting resolvable radiation between scale q_1^2 to q_2^2. Adding a Sudakov form factor suppresses real gluon emission from the fusing gluons when the screening gluon fails to screen the colour charge of the fusing gluon

Naively, one can say Sudakov form factor will add a factor proportional to $exp(\ln^2(\frac{M_H^2}{\bar{k}^2}))$ [80] to the amplitude, which will cancel out the diverging effect of $\bar{k}^4$ in the denominator of the amplitude.

In order to determine this factor properly, one needs to calculate the probability of single gluon emission with the transverse momentum between q^2 and $q^2 + dq^2$ which is given by:

$$\int_{q_1}^{q_2} \frac{\alpha_s(q^2)}{2\pi} \frac{dq^2}{q^2} \int\limits_{1/q^2}^{1-1/q^2} \sum_i P_i(z) dz \tag{6.11}$$

here $P_i(z)$ is the DGLAP splitting function, which gives the probability density for a gluon to branch off to a parton i [115].

Following the radioactive decay rule, the Sudakov form factor will take the exponential form.

$$T(\bar{k}^2, M_H^2) = exp\left(\int_{\bar{k}^2}^{(\frac{M_H}{2})^2} \frac{\alpha_s(q^2)}{2\pi} \frac{dq^2}{q^2} \int\limits_{0}^{1-\Delta} (P_{gq}(z) + P_{gg}(z)) dz \right) \tag{6.12}$$

where $\Delta = \frac{\bar{k}}{\bar{k}+m_H}$.

Therefore, the explicit form for the parton distribution function to single log accuracy, with no real gluon emission, can be expressed as:

$$f(x, x', \bar{k}^2, \mu^2, t) = 1.2e^{(-\frac{B}{2}p_t^2)} \frac{\partial\Big(T(\bar{k}^2, M_H^2)xg(x, \bar{k}^2)\Big)}{\partial \ln \bar{k}^2} \tag{6.13}$$

The Sudakov form factor eliminates the hard rescattering of QCD bremsstrahlung gluon from the two fusing gluons, however, soft rescattering of secondary particles can occur between the protons during the exclusive reaction which contaminates the signature rapidity gap of the exclusive interaction, as discussed extensively in chapter 5.

The currently available methods to calculate the RGSP are all model dependent, causing a large uncertainty, of more than a factor of 2, to the cross-section. In General, the calculated values of the RGSP lie between 2% and 6%, as expected for the CED process in the LHC's kinematical regime. In the previous chapter, we discussed extensively the GSP for a CED process. In this study we used the prediction made by GLAM [88] and KMRS [89] models for the two channel pomeron in the CED processes which provide a more reliable estimate of $\Big\langle \mid S^2 \mid \Big\rangle$. The estimated value for the survival probability associated with LHC Higgs production is 2.7% [88, 89].

6.5 Equivalent Photon Flux and Z^2 Effect

Taking y as the rapidity of the Higgs boson, after integrating over the transverse momentum of the proton, the differential cross-section of ($\gamma^* + p \rightarrow$

$\gamma^* + H + p)$ is

$$\frac{d\sigma_\gamma}{dy} = \frac{1}{100\pi^6 b}\Big(\frac{C_F \alpha M_H^2}{(N_c^2-1)v}\Big)^2 \int d^2\bar{q}_\perp (\mathcal{M})^2 \tag{6.14}$$

where

$$(\mathcal{M})^2 = C\Big(\int_{k_0^2}^{(\frac{M_H}{2})^2} d^2\bar{k} \int_0^1 d\alpha_l \int_0^1 d\tau \alpha_s^2(\bar{k}^2) \frac{\partial\Big(T(\bar{k}^2, M_H^2)G(x,\bar{k}^2)\Big)}{\partial \ln \bar{k}^2} \sum_q (F_1 + F_2)\Big)^2 \tag{6.15}$$

The total photo-production cross-section $(p + p \to p + H + p)$ is obtained by convoluting the partonic cross-section $(\gamma^* + p \to \gamma^* + H + p)$ with the equivalent photon flux, $N_\gamma(E)$.

$$\frac{d\sigma_t}{dy} = \int \frac{dE}{E} N_\gamma(E) \frac{d\sigma_\gamma(E)}{dy}, \tag{6.16}$$

where E is the energy carried by the photon.

The flux of equivalent photons from a relativistic particle of charge Z is determined from the Fourier transform of its electromagnetic field represented by Weizsacker-Williams formula [110].

$$\frac{dN_\gamma}{dE} = \frac{2Z^2\alpha}{\pi z E}(\Big(XK_0(X)K_1(X) - \frac{X^2}{2}(K_1^2 K_0^2)) \tag{6.17}$$

K_0 and K_1 are the modified Bessel functions of the second kind, of order zero and order one, as a function of $X = \dfrac{2R_A E}{\gamma}$.

The intensity of the electromagnetic field, and therefore the number of photons in the cloud surrounding the nucleus, scales as the squared charge of the beam, Z^2 as can be seen in equation 6.17.

In case of the proton, the photon flux equation can be simplified to [110]:

$$\frac{dN_\gamma}{dz} = \frac{\alpha}{2\pi z}(1 + (1-z)^2)\Big(\mu - \frac{11}{1} + \frac{3}{\mu} - \frac{3}{2\mu^2} + \frac{1}{3\mu^3}\Big) \tag{6.18}$$

$z = \frac{W_{\gamma P}^2}{S}$ and $\mu = 1 + \frac{0.71GeV^2}{Q_{min}^2}$ and Q_{min} is the minimum momentum transfer needed to produce the vector meson.

6.6 Computing Code Utilized

"Photoproduction" package is a Fortran based Monte Carlo event generator which we wrote to compute the cross-section of the CEDP process in UP Collision and DPE, for a Higgs boson with a mass of 125 GeV. The program uses VEGAS algorithm [131] and random number generator programs to calculate the cross-section. By default, the program makes use of the Fortran LHAPDF [128] library to extract the PDF values at given x and Q^2. The blueprint of the package is described in appendix G.

6.6.1 VEGAS

The VEGAS code gives Monte Carlo estimates of arbitrary multi-dimensional integrals using the VEGAS algorithm of G. P. Lepage [131]. The VEGAS algorithm is shown in figure 6.3. Achieving a good estimate of a multi-dimensional integral requires large sample sizes at higher dimensions which increases the computation time exponentially. Thus, the standard Monte Carlo integration which uses Uniform Sampling wouldn't be efficient. VEGAS algorithm uses Monte Carlo technique to determine the integral however it is based on the concept of adaptive Importance Sampling technique to speed up the convergence of the integral by optimizing the size of each grid, in the multi-dimensional space, based on their contribution to the integral.

The first step of the VEGAS algorithm is choosing a grid which uniformly spaced along the axes of multi-dimensional space. Then, after putting M sample points in the N hyper-cubes[29] so that the number of points in each

[29] In more than 3 dimensions each block in the grid is called hyper-cube.

hypercube is the same $\frac{M}{N}$, the integral at each of these points will be evaluated using Monte Carlo estimate of the integral. From calculations, we can infer the probability density function:

$$P(\vec{x}) = \frac{f(\vec{x})}{\int_{\Omega} f(\vec{x}) d\vec{x}}. \tag{6.19}$$

when the integral is a function of n variables $\vec{x} = (x_1, ..., x_n)$ over a volume Ω and $I = \int_{\Omega} f(\vec{x}) d\vec{x}$.

To simplify the problem, let's limit ourselves to a one dimensional integral which can be expanded to a multi-dimensional integral. For present purposes, we assume p(x) is a step function with N steps. The probability of a random number being chosen from any given step is defined to be a constant, equal to $\frac{1}{N}$ for all steps. Therefore,

$$P(\vec{x}) = \frac{1}{N \Delta x_i} \qquad , x_i - \Delta x_i \leq x < x_i \qquad , i = 1, ..., N \tag{6.20}$$

The probability density is refined by subdividing each step Δx_i into $m_i + 1$ subintervals where

$$\begin{aligned} m_i &= k \frac{f_i \Delta x_i}{\sum_j f_j \Delta x_j} \\ f_i &= \frac{1}{\Delta x_i} \int_{x_i - \Delta x_i}^{x_i} f(x) dx \end{aligned} \tag{6.21}$$

Thus, each interval's contribution to the weight function increases in proportion to its contribution to the integral of $f(x)$.

In order to keep the number of steps to its original value N, groups of new intervals must be combined in such a way that the number of subintervals in each group is constant. Therefore, the net effect is to alter the step sizes, while keeping the total number constant, so that the smallest steps occur where the function is largest, or the variance is optimal. The new grid is used and further refined in subsequent iterations. After several iterations of this process, the grid usually converges to the optimal grid. When the net amount of iterations is reached or a minimum value of variance is obtained, the program stops.

A cumulative estimate of the integral and its standard deviation can be determined using the following formula:

$$\begin{aligned}\bar{I} &= \frac{\sum_i I_i \frac{I_i^2}{\sigma_i^2}}{\sum_i \frac{I_i^2}{\sigma_i^2}} \\ \bar{\sigma} &= \frac{\bar{I}}{\sqrt{\sum_i \frac{I_i^2}{\sigma_i^2}}}\end{aligned} \tag{6.22}$$

Here I_i and σ_i are the integral and standard deviation estimated in iteration i.

6.6.2 The PDF Set

The Fortran LHAPDF library [128] provides access to the numerical values for all parton densities, $xf(x, k^2)$, using a PDF set. The PDF set we are using in this study is called MSTW08NLO [126]. However, the program is flexible enough to use other PDF sets with just a little bit of adjustment for $k^2 < 1$. Because all the PDF sets in the LHAPDF library are mostly valid for $k^2 > 1$ so for $k^2 < 1$ one has to define and add the right PDF and α_s to the code.

A relatively new analysis of parton distribution of the proton that incorporates a wide range of data from $p-p$ or $p-\bar{p}$ or $e-p$ high energy col-

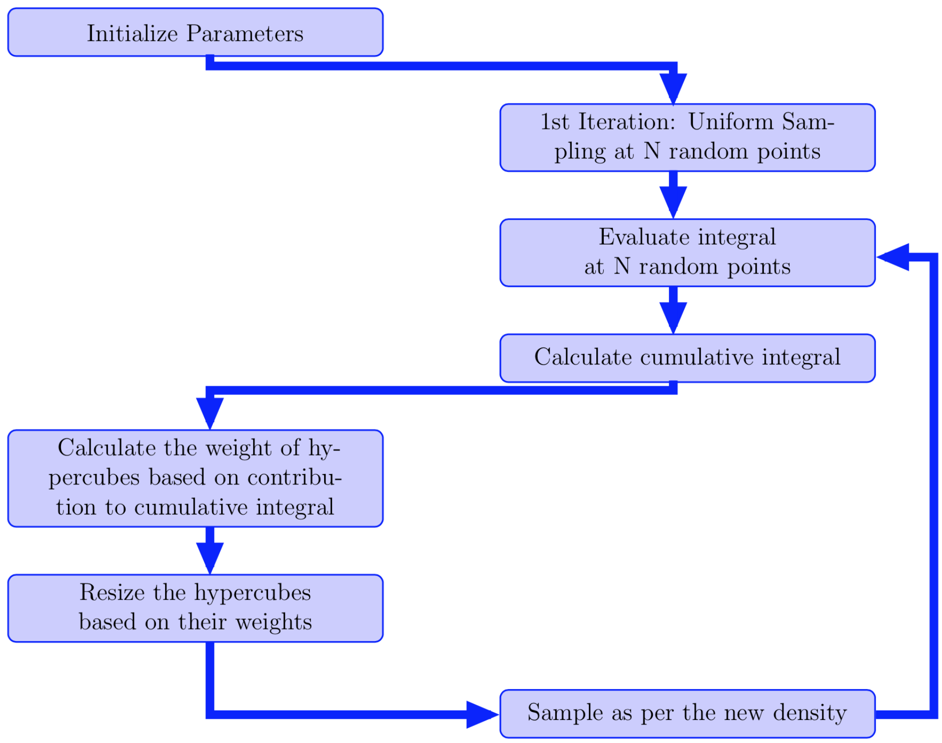

Figure 6.3: VEGAS flowchart

lision is incorporated in the MSTW08 PDF set available in the LHAPDF library. The main processes and data sets included in the PDF analysis for MSTW08NLO are ordered in three groups: fixed-target experiments, HERA ,and the Tevatron in table 1 and 2 of reference [126]. For each process, the dominant partonic subprocesses, the primary partons which are probed, and the approximate range of x are given. The PDF for each type of parton are determined by global fits to all the available DIS[30], and related hard- scattering data[31].

[30] In MSTW08NLO the DIS data from HERA, BCDMS, CCFR, SLAC and NMC used to constrain the PDF behaviour.

[31] In order to put further constraint on the PDFs and reduce their uncertainties, the inclusive jets of H1 and ZEUS, and several LHC and the Tevatron data such as W and Z production by $D\O$ and CDF Collaborations are used.

In the MSTW PDF set, the parameterizations for the input distributions are based on Chebyshev polynomials of the form: [32].

$$xf(x,\mu_0^2) = A(1-x)^{\eta}x^{\delta}(1+\sigma_{i=1}^{n} a - iT_i^{Ch}(y(x)) \qquad (6.23)$$

here $T_i^{Ch}(y(x))$ are Chebyshev polynomials and $y = 1 - 2x^k$. The global fit determines the values of the set of parameters A, δ, η and a_i for each PDF. The parameterization of the parton distributions (distribution of quarks, u, s, d, and gluon g) at the input scale $\mu_0^2 = 1$ GeV^2 [33] are given as as the following equations:

$$\begin{aligned}
xu_v &= A_u x^{\eta_1}(1-x)^{\eta_2}(1+\epsilon_u\sqrt{x}+\gamma_u x)\\
xd_v &= A_d x^{\eta_3}(1-x)^{\eta_4}(1+\epsilon_d\sqrt{x}+\gamma_d x)\\
xS &= A_s x^{\eta_s}(1-x)^{\delta_s}(1+\epsilon_s\sqrt{x}+\gamma_s x)\\
x\Delta &= A_\Delta x^{\eta_\Delta}(1-x)^{\eta_s+2}(1+\gamma_\Delta x+\delta_\Delta x^2 \qquad (6.24)\\
xs+x\bar{s} &= A_+ x^{\eta_s}(1-x)^{\eta_+}(1+\epsilon_s\sqrt{x}+\gamma_s x)\\
xs-x\bar{s} &= A_- x^{0.2}(1-x)^{\eta_-}(1-\frac{x}{x_0})\\
xg &= A_g x^{\delta_g}(1-x)^{\eta_g}(1+\epsilon_g\sqrt{x}+\gamma_g x)+A'_g x^{\delta'_g}(1-x)^{\eta'_g}
\end{aligned}$$

where $u_v \equiv u-\bar{u}$, $d_v \equiv d-\bar{d}$, $S \equiv 2(\bar{u}+\bar{d})+s+\bar{s}$, and $\Delta \equiv \bar{d}-\bar{u}$. $A_{u/d/S/\Delta/g/+/-}$, $\delta_{S/\Delta/g/g'}$, $\eta_{1/2/3/4/S/\Delta/g/g'/+/-}$, $\epsilon_{u/d/S/g/g'}$, $\gamma_{u/d/s/\Delta/g}$, and X_0 are the free parameters.

The extra term $A'_g x^{\delta'_g}(1-x)^{\eta'_g}$ in the gluon distribution is added because It was found [124], that the global fit was considerably improved by allowing

[32]The detailed of this study is in [125, 126]

[33]There is very little sensitivity to variation in μ_0^2 for the PDFs extracted.

the gluon distribution to have a second term with a different small x power, where η_g' is quite large and concentrates the effect of this term towards small x.

The input PDFs are subject to three constraints from the valence quark number sum rules

$$\int_0^1 dx.u_v(x,\mu_0^2) = 2, \int_0^1 dx.d_v(x,\mu_0^2) = 1, \int_0^1 dx.s_v = 0 \tag{6.25}$$

and the momentum sum rule.

$$\int_0^1 dx.x\big(u_v(x,\mu_0^2) + d_v(x,\mu_0^2) + S(x,\mu_0^2) + g(x,\mu_0^2)\big) = 1 \tag{6.26}$$

There are, therefore, potentially $34-4=30$ free PDF parameters in the fit (free parameters in equation 6.24 minus the four constraints from the valence quark number sum rules), including the strong coupling defined at the scale of the Z boson mass, $\alpha_s(M_Z^2)$, which is allowed to be free when determining the best fit. The values of these parameters obtained in the LO, NLO and NNLO fits are given in reference [126].

In order to find the PDF value for the given momentum fraction x and scale $k = \sqrt{q_{sq}}$, we need to use the subroutine "*initpdfset* ('$MSTW2008lo68cl.LHgrid$')" to set up the LHAPDF interface code and call the specific PDF set MSTW08NLO 90% confidence level. Once the PDF member is initialized one must call the evolution code which will return the PDF momentum densities, $f(x,k^2)$, at given x and k^2, by using the subroutine "$evolvePDF(x,k^2,f)$"where x is the Bjorken scale and k is the 4-momentum of the parton and f indicates the type of parton. The PDF $xf(x,k^2)$ values come from the GridPDF class in the LHAPD which provides PDF values interpolated from data files.These data files consist of PDF values evaluated on a rectangular grid of "knots" in (x,k^2), with values for all flavours of quarks and gluon, at each point. The spacing of the knot positions in x and k^2 is represented in uniform distributions in log x and log k^2. Also for (x,k^2) points outside the grid range, MSTW provides a sensible extrapolation to small-x, low-k and high-k values [127].

Strong Coupling

We recall from chapter 5, where we discussed the QCD running coupling, that equation 5.7 shows the strong running coupling at scale Q^2 in terms of energy scale k and QCD scale λ_{QCD}. However, in this equation, α_s diverges (Landau pole) as the energy scale gets close to the QCD scale, $Q^2 \leq \lambda^2_{QCD}$, as a result of QCD confinement phenomena.

While a process like DPE, due to having a factor like $T(k^2, M_H^2)/k^4$ [80] in the integrand (T is the Sudakov form factor and k^4 is the transverse momentum of the exchanged gluon), can set the cutoff on the k^2 integral well above the point where the perturbative QCD running coupling becomes invalid, the CEDP process does not have this advantage. Even though, the integrand is safely peaked in the perturbative regime, as shown in figure 6.4, the additional k^2 in the denominator requires a cutoff of around 0.1 GeV^2.

As it is necessary to use an α_s consistent with the PDF evolution, we use the form of $\alpha_S(Q^2)$ used in MSTW08NLO fits which is only valid in perturbative domain and diverges in low energy scale. However, as a result of the low energy

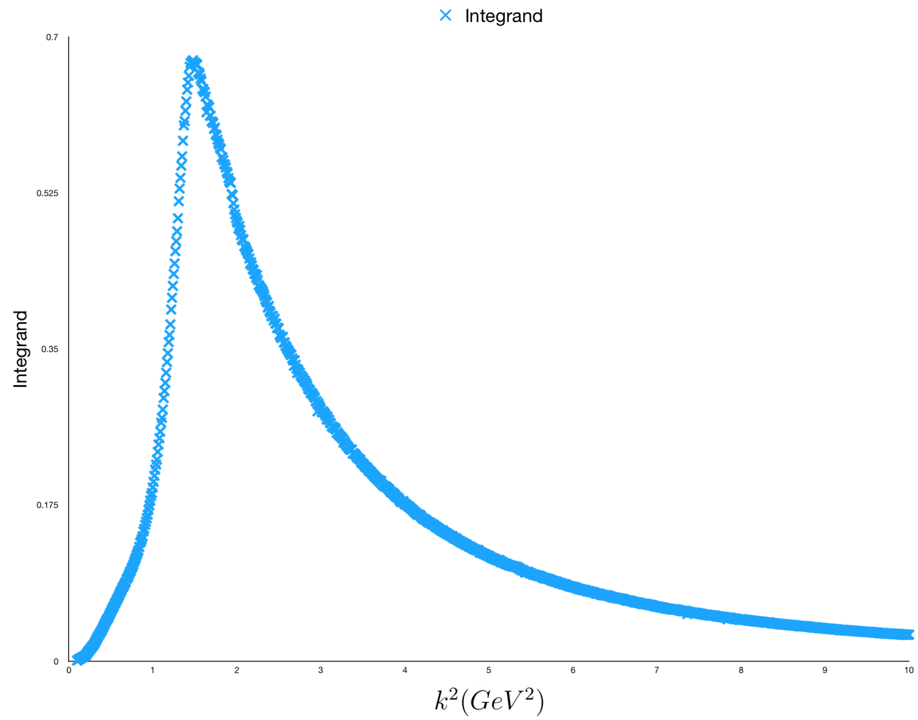

Figure 6.4: The integrand of the k integrand in equation $\int d^2\bar{k} \int_0^1 d\alpha_l \int_0^1 d\tau \alpha_s^3(\bar{k}^2) \sum_q (F_1 + F_2)$. F_1 and F_2 are defined in equation 6.7.

scale cut-off k, we must consider a different models of the infrared behaviour of the strong coupling constant in the non perturbative domain.

One can improve the perturbative QCD (pQCD) series by suppressing the Landau pole and using the analytic approach, also known as analytical perturbation theory. Extended description of this model can be found in [130]. We have chosen the "analytic" approach [116] using the "approximate solution" [129] due to its low k^2 behaviour, well-defined formula, and properties such as gauge-independence, universality, and IR-finite behaviour.

The "analytical" running coupling equation in the Leading order can be expressed as:

$$\alpha_{an}^{(0)}(k^2) = \frac{4\pi}{\beta_0}\Big(\frac{1}{ln(k^2/\Lambda^2)} + \frac{\Lambda^2}{\Lambda^2 - k^2}\Big) \tag{6.27}$$

And the approximate solution for the NLO is shown as the following equation.

$$\alpha_{an}^{(2,approx.)}(k^2) = \frac{4\pi}{\beta_0(N_f = 3)}\Big(\frac{1}{l(L_Q, c)} + \frac{1}{1 - exp(l(L_Q, c))}\Big) \tag{6.28}$$

$$l(L_Q, c) = L_Q + c\ ln(\sqrt{L_Q^2 + 4\pi^2}) \tag{6.29}$$

$$L_Q = ln(\frac{k^2}{\Lambda^2}) \tag{6.30}$$

$$\beta_0 = 11 - \frac{2}{3}N_f \tag{6.31}$$

$$\beta_1 = 102 - \frac{38}{3}N_f \tag{6.32}$$

$$c = \frac{\beta_1}{\beta_0^2} \tag{6.33}$$

We have used $N_f = 3$ as the number of effective (light) flavours and $\Lambda = 0.35$ GeV as the QCD scale parameter in the "analytic" method.

Using the α_s related to the MSTW08NLO PDF set for the perturbative region and $k^2 > 1$ GeV^2 and the fitted "analytic" leading order α_s for the non-perturbative region $k^2 < 1$ GeV^2, the plot of $\alpha_s(k^2)$ shown in figure 6.5 was made. The green line shows the α_s related to the MSTW08NLO PDF set. It diverges for the very small (k^2). The blue line represents the"analytic" model fitted to the α_s plot from MSTW08NLOat $k^2 < 1$ GeV^2.

The values of α_s shown with the green line in figure 6.5 obtained from the fitting of the two models are stored in a grid file of x and k^2 in the

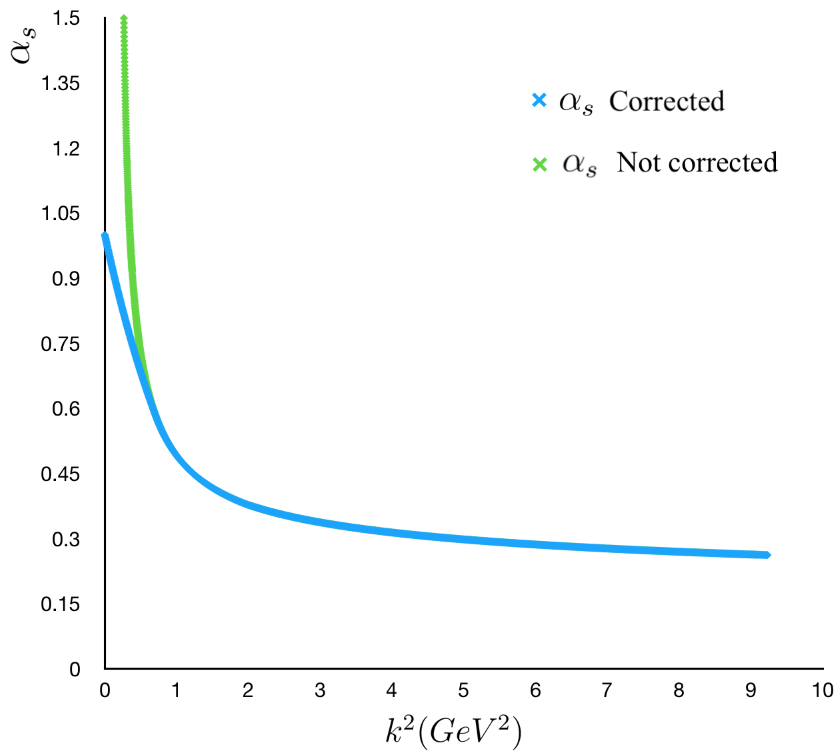

Figure 6.5: Values of α_s MSTW08NLO PDF set and "analytic" model. The green line is the plot of α_s related to MSTW08NLO PDF set. The blue line represents the "analytic" model fitted to the α_s plot from MSTW08NLO at $k^2 < 1$ GeV^2.

LHAPDF along with the PDF values for each x and k^2 and added to the "photoproduction" package.

6.6.3 Results of the Cross-section Calculation

Integrand and the Cross-Section

The integrand for the total cross-section that is used in this package is:

$$\frac{\sigma_{tot}}{dy} = \int dQ(2\pi\gamma q_t Q)\frac{\alpha}{2\pi z}(1+(1-z)^2)\Big(\mu - \frac{11}{1} + \frac{3}{\mu} - \frac{3}{2\mu^2} + \frac{1}{3\mu^3}\Big)\frac{d\sigma_\gamma}{dy} \tag{6.34}$$

where

$$\begin{aligned}
\frac{d\sigma_\gamma}{dy} =& \frac{1}{100\pi^6 b}\Big(\frac{C_F\alpha M_H^2}{(N_c^2-1)v}\Big)^2\int d^2\bar{q}_\perp\Big(\int_{k_0^2}^{(\frac{M_H}{2})^2} d^2\bar{k}\int_0^1 d\alpha_l\int_0^1 d\tau\alpha_s^2(\bar{k}^2)f_g(x,k^2,M_H)\sum_q(F_1+F_2)\Big)^2\\
F_1 =& \frac{e_q^2}{\bar{k}^4}\frac{[\alpha_l^2+(1-\alpha_l)^2][\tau^2+(1-\tau^2)]}{\alpha_l(1-\alpha_l)Q^2+\tau(1-\tau)\bar{k}^2+m_q^2}\\
F_2 =& \frac{e_q^2 m_q^2}{\bar{k}^6(\alpha_l(1-\alpha_l)Q^2+\tau(1-\tau)\bar{k}^2+m_q^2)}\big(4(1-\alpha_1+\alpha_l^2)+\frac{2e_q^2\bar{k}^2\tau(1-\tau)(6\alpha_l^2-6\alpha_l+1)}{\alpha_l(1-\alpha_l)Q^2+m_q^2}\big)
\end{aligned} \tag{6.35}$$

Also, $\gamma = \frac{\sqrt{s}}{2m_P}$, $x = \frac{M_H}{\sqrt{s}}$, $q_t = Qcos(\phi)$, $z = Qsin(\phi)\frac{\sqrt{s}}{m_P}$, $\mu = 1+0.71\frac{\gamma^2}{z^2}$.

This integral is a nine-dimensional integral and the integral parameters are α_l, τ, α_l', τ', the gluon momentum k and k', photon virtuality Q and ϕ the angle between q_t and w (the photon energy). $f_g(x,k^2,M_H) = \frac{\partial\Big(T(\bar{k}^2,M_H^2)G(x,\bar{k}^2)\Big)}{\partial\ln\bar{k}^2}$ is determined from the MSTW08NLO. $\alpha_s(k^2)$, $\alpha_s(k'^2)$ are defined in the extra package that we added to the MSTW08NLO. The cross-section is integrated over the rapidity interval $-2.5 < y < 2.5$.

Finally, we calculated the cross-section of Higgs boson production in CED processes in p-p and Pb-p collisions at the LHC at the CM energy of $\sqrt{s} = 14$

Name	CEDP	DPE	$\gamma\gamma$ process	CEDP	$\gamma\gamma$ process
Process	$p + p \rightarrow p + H + p$			$Pb + p \rightarrow Pb + H + p$	
Subprocess	$\gamma^* q \rightarrow \gamma^* + H + q$	$\mathbb{P}\mathbb{P} \rightarrow H$	$\gamma\gamma \rightarrow H$	$\gamma^* q \rightarrow \gamma^* + H + q$	$\gamma\gamma \rightarrow H$
Cross-section (fb)	0.19 ± 0.005	2.55 ± 0.001	0.18	182.5 ± 0.02	170
RGSP	2.7%	2.7%	100%	2.7%	100%
$\sqrt{s}$ (TeV)	14	14	14	8.8	8.8

Table 6.1: Higgs boson production in CED processes for $M_H = 125$ GeV after considering the RGSP in the calculation. The cross-section for the CEDP and DPE processes are calculated using "Photoproduction" package. The cross-section of $\gamma\gamma$ process is calculated by D'Enteria et al.[108].

TeV and $\sqrt{s} = 8.8$ TeV, respectively . The result is shown in table 6.1. The cross-sections of DPE and CEDP in p-p and Pb-p collisions are calculated using the "photoproduction" package (for more details about this package see Appendix G) and the cross-sections of $\gamma\gamma$ process in p-p and Pb-p collisions as calculated by D'Enterria and Landsberg in reference [108].

The cross-section of DPE in p-p collision was initially calculated by Durham group [121]. We also calculated this cross-section using our "photoproduction" package adapted for DPE to check the reliability of the code. We have calculated the DPE cross-section to be 2.55 fb which is the highest cross-section of the three processes (DPE, CEDP and $\gamma\gamma$ process), in agreement with the Durham Group's calculation [133]. The CEDP process is also expected to have lower cross-section compare to that of DEP process and higher compare to that of $\gamma\gamma$ process due to the fact that this process is partially a QCD process($\sigma \propto \alpha_s^2 \alpha^2$). However, because of the QED nature of the $\gamma\gamma$ process, no secondary gluon will be emitted to fill the rapidity gap and therefore this process with not suffer from the low value of SRGP. Therefore, both CEDP and $\gamma\gamma$ processes have cross-sections int the same order. Both these processes can happen in p-Pb collisions as well. As we discussed in section 6.5, charged beams are associated with a flux of quasi-real photons that is proportional to the square of the charge of the beam particle. Thus, for p-Pb collisions one would naively expect the cross-section to be enhanced by a factor of Z^2 .

Sources of Error

The errors represented in table 6.1 for the cross-sections of DPE and CEDP calculated using the "photoproduction" package are due to the errors in calculation of the integrand. However there are other more important factors that increase uncertainty in the calculation of CED processes. One of these is our estimate of the RGSP. We discussed the estimated value of RGSP in this chapter, however, RGSP is still an open question in high energy physics. With this caveat in mind we shall adopt, without error, the values for RGSP utilized in our calculations above.

After RGSP, the PDF set is the secondmost major source of uncertainty in the calculation of DPE and CEDP cross-sections. In an study by the Durham group [133], the cross-section of the DPE process was calculated using MSTW08 LO and NLO PDF sets, shown in figure 6.6. It shows the sensitivity of the cross-section to the choice of PDF set could be up to 50% for Higgs boson with the mass of $M_H = 125$ GeV. Thus, we assume that the effect of PDF uncertainty is in the same range for the CEDP process.

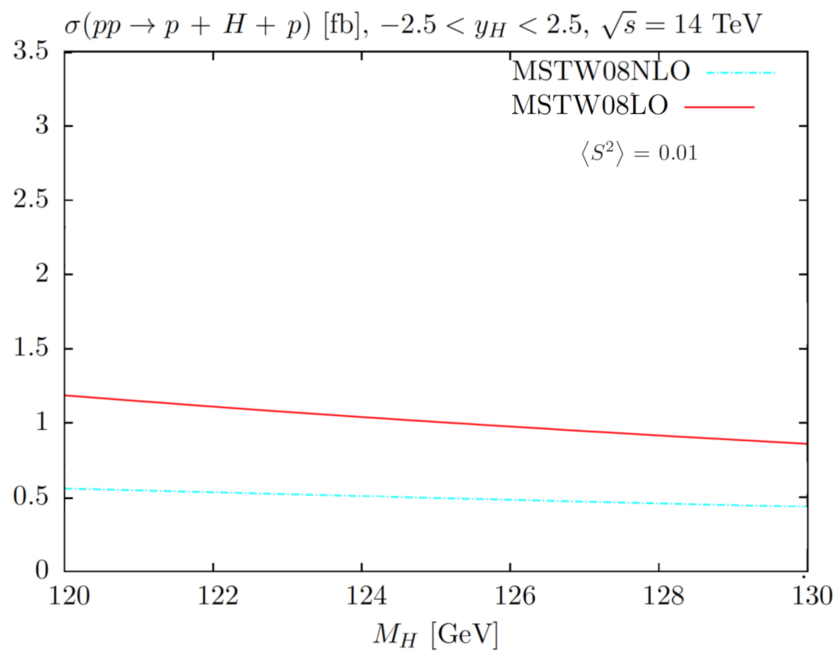

Figure 6.6: Cross-section of the DPE processes in centre of mass energy of 14 TeV, integrated over the rapidity interval $-2.5 < y < 2.5$, for a range of PDFs MSTW08LO and NLO [133].

Mass of the Higgs Boson

We find that the CEDP process is a sensitive measure of the Higgs boson mass since the CEDP cross-section depends quadratically on the Higgs boson mass in equation 6.35, whereas in other similar processes such as DPE and $\gamma\gamma$ process, the cross-section has no direct dependency on the mass of Higgs boson and only the PDF is a function of M_H^2. Therefore as it can be seen in figure 6.7 the cross-section drops as the mass of Higgs boson increases for the process like the CEDP. Figure 6.7 shows the quadratic behaviour of the CEDP cross-section versus mass of Higgs boson and the linear behaviour of DEP cross-section.

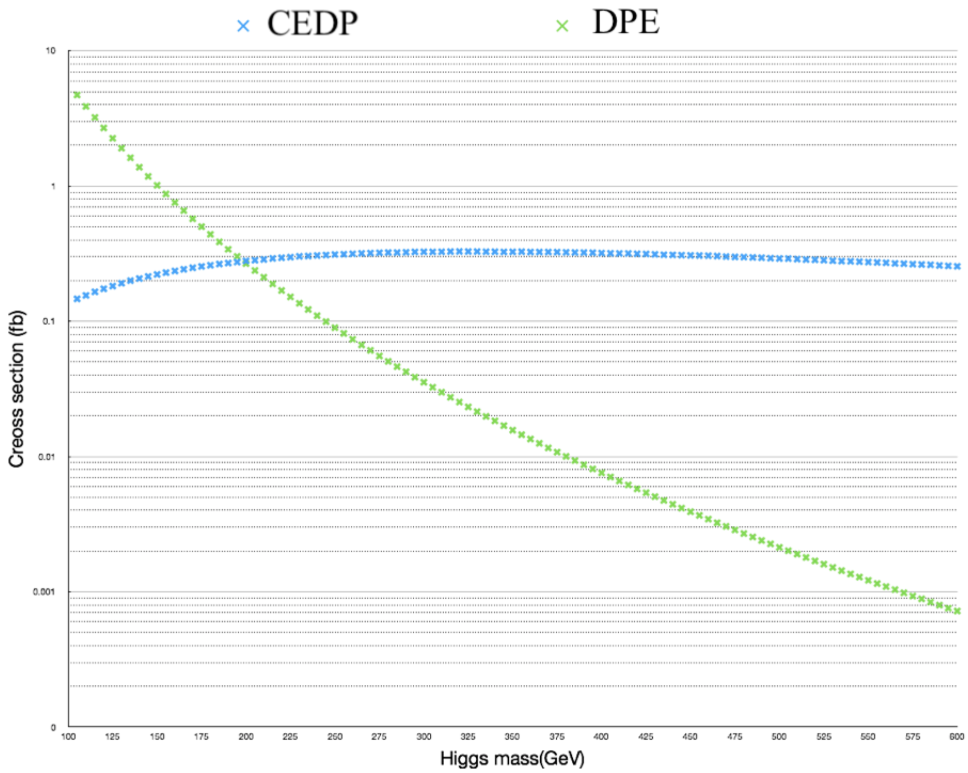

Figure 6.7: The Higgs cross-section dependence upon M_H in DPE and the CEDP process. The blue (dark grey) cross line shows the quadratic behaviour of the cross-section of the CEDP process and the green (light grey) line represent the linear behaviour of DPE cross-section.

Chapter 7

Summary And Conclusion

The work described in this thesis covers three main topics. The first topic involves the LUCID detector upgrades and LUCID's performance during the runs in 2015, as described in chapter 3. I made major contributions in all the studies described in this chapter, during the time I worked with the LUCID group at CERN. This work was part of the mandatory task towards qualification for ATLAS authorship.

My authorship task was to: 1) update the Monte Carlo description of LUCID by incorporating the new geometry of the LUCID-2 detector; 2) improve the performance of LUCID-2 by studying how to, practically, reduce its acceptance; and, 3) study the performance of the LUCID-2 detector, compared with other detectors that can be used to determine the luminosity, with a view to determining the systematic errors on the LUCID's determination of the luminosity received by the ATLAS detector. In addition, my studies led to an automatic PMT gain adjustment system being implemented in 2016. As reported in Chapter 3, we achieved an overall error on the LUCID luminosity measurement - in the data-taking period where the bunch spacing was at the LHC design value of 25 ns - of 2.1%. This, high degree of precision combined with LUCID's ability to make bunch-by-bunch luminosity measurements for the LHC machine group, led to LUCID being chosen as the official luminosity monitor of ATLAS.

The second topic that is covered in this thesis, in Chapter 4, is the AFP detector and its electronics. AFP is the newest ATLAS sub-detector. Its purpose is to identify and measure the energy loss of one or both protons that emerge intact from proton-proton diffractive events collisions in ATLAS. For "exclusive" events, from Central Exclusive Diffraction (CED), where both protons survive and are measured in AFP, it is possible to determine the mass and quantum numbers of central state with high precision. This opens up a whole new physics arena of diffractive physics for ATLAS by turning the LHC into a pomeron-pomeron, photon-photon and photon-pomeron collider.

The Alberta contributions to this detector were to the Roman Pot mechanics used to pace the proton spectrometer within millimetres from the beam and to the readout system for the precision ToF system. My contributions to the AFP detector were concentrated on the readout electronics for the precision ToF detector that is of critical importance in reducing the background from pileup backgrounds. My responsibility here was to create a test-bed for the HPTDC modules - used to readout the AFP ToF detectors - that we built here at the University of Alberta and to use this test-bed to validate the performance of these modules. One of the key issues here was the increase in precision due to multiple, separate, measurements of the ToF. In principle the precision increases according to the square root of the number of separate measurements. After calibrating the HPTDC modules, I verified using the test-bed that this is not quite the case as a coherent effect, affecting all the channels, reduces the expected improvement of the resolution by about 20%. The overall time resolution delivered by our electronics was 14 ps per channel. The overall timing resolution of the ToF detector plus electronics has been found from test-beam to be between 35 to 37 ps for a train of only two LQbars.

The third and main topic of my thesis is the study of three channels of the Higgs production via CED, $p + p \to p \oplus H \oplus p$. In particular I made the first reliable calculation of the ultra-peripheral CED "photoproduction" of the Higgs boson via the diagram shown in Figure 6.2 for both proton-proton and proton-heavy-ion collisions at the LHC. In addition, I calculated CED Higgs production via double pomeron exchange and photon fusion, for the purpose of comparison and verification of my main calculation.

Using "Photoproduction" package w/o RGSP: $\sigma(\gamma^* q \to \gamma^* + H + q) = 7.04 fb$

Using "Photoproduction" package with RGSP: $\sigma(\gamma^* q \to \gamma^* + H + q) = 0.19 fb$

Using "Photoproduction" package with RGSP: $\sigma(\mathbb{P}\mathbb{P} \to H) = 2.5 fb$

Durham group value with RGSP [133]: $\sigma(\mathbb{P}\mathbb{P} \to H) = 1.5 fb$

It turns out that the cross-sections for proton-proton production of all three processes is similar in size. The results of my calculation of Higgs production by DPE are in good agreement with previous results published by the Durham Group [133].

An interesting and important feature of the ultra-peripheral "photoproduction" and photon fusion production of the Higgs boson is that they are enhanced by approximately Z^2. For proton - lead beam this factor is 6.7×10^3. Another, feature of the "photo-production" channel is that the cross-section has a significant dependence on the Higgs mass. In the era of precision Higgs measurements it is important that as many Higgs decay channels are studied as precisely as possible. Especially if the cross-section for the process is mass dependent as is the case with the ultra-peripheral CED "photoproduction" of the Higgs boson, studied in this thesis.

Bibliography

[1] H. T. Edwards, "The Tevatron Energy Doubler: A Superconducting Accelerator", Ann. Rev. Nucl. Part. Sci. **35**, 605 (1985).

[2] "HERA", URL: www.desy.de/research/facilities__projects/hera/index_eng.html

[3] "HeavyIonPublicResults", URL: https://twiki.cern.ch/twiki/bin/view/AtlasPublic /HeavyIonsPublicResults

[4] "LuminosityPublicResults", URL :https://twiki.cern.ch/twiki/bin/view/AtlasPublic /LuminosityPublicResults#2011-_Pb_Pb_Heavy_Ion_Collisions

[5] R. Bruce *et al.*, "LHC Run 2: Results and challenges", Proceedings, 57th ICFA Advanced Beam Dynamics Workshop on High-Intensity and High-Brightness Hadron Beams (HB2016): Malmo, Sweden, July 3-8, 2016

[6] "Longer term LHC schedule", URL: http://lhc-commissioning.web.cern.ch/lhc-commissioning/schedule/LHC-schedule-update.pdf

[7] G. Aad *et al.* [ATLAS Collaboration], "The ATLAS Experiment at the CERN Large Hadron Collider", JINST **3**, S08003 (2008).

[8] S. Chatrchyan *et al.* [CMS Collaboration], "The CMS Experiment at the CERN LHC", JINST **3**, S08004 (2008).

[9] K. Aamodt *et al.* [ALICE Collaboration], "The ALICE experiment at the CERN LHC", JINST **3**, S08002 (2008).

[10] A. A. Alves, Jr. *et al.* [LHCb Collaboration], "The LHCb Detector at the LHC", JINST **3**, S08005 (2008).

[11] O.Adriani *et al.* [LHCf Collaboration], "The LHCf detector at the CERN Large Hadron Collider", JINST **3**, S08006 (2008).

[12] J. Pinfold *et al.* [MoEDAL Collaboration], "Technical Design Report of the MoEDAL Experiment", CERN-LHCC-2009-006, MoEDAL-TDR-001.

[13] G. Anelli *et al.* [TOTEM Collaboration], "The TOTEM experiment at the CERN Large Hadron Collider", JINST **3**, S08007 (2008).

[14] [ATLAS Collaboration], "ATLAS central solenoid: Technical design report", CERN-LHCC-97-21.

[15] [ATLAS Collaboration], "ATLAS barrel toroid: Technical design report", CERN-LHCC-97-19.

[16] [ATLAS Collaboration], "ATLAS endcap toroids: Technical design report", CERN-LHCC-97-20.

[17] [ATLAS Collaboration], "ATLAS inner detector: Technical design report. Vol. 1", CERN-LHCC-97-16, ATLAS-TDR-4.

[18] [ATLAS Collaboration], "ATLAS inner detector: Technical design report. Vol. 2", CERN-LHCC-97-17.

[19] [ATLAS Collaboration], "Technical Design Report for the ATLAS Inner Tracker Pixel Detector", CERN-LHCC-2017-021. ATLAS-TDR-030.

M. S. Alam *et al.* [ATLAS Collaboration], "ATLAS pixel detector: Technical design report", CERN-LHCC-98-13.

[20] M. Backhaus [ATLAS Collaboration], "The upgraded Pixel Detector of the ATLAS Experiment for Run 2 at the Large Hadron Collider", Nucl. Instrum. Meth. A **831**, 65 (2016).

[21] A. Abdesselam *et al.* [ATLAS Collaboration], "The barrel modules of the ATLAS semiconductor tracker", Nucl. Instrum. Meth. A **568**, 642 (2006).

[22] A. Abdesselam *et al.* [ATLAS Collaboration], "The ATLAS semiconductor tracker end-cap module", Nucl. Instrum. Meth. A **575**, 353 (2007).

[23] A. Ahmad *et al.* [ATLAS Collaboration], "The Silicon microstrip sensors of the ATLAS semiconductor tracker", Nucl. Instrum. Meth. A **578**, 98 (2007).

[24] E. Abat *et al.* [ATLAS TRT Collaboration], "The ATLAS TRT barrel detector", JINST **3**, P02014 (2008).

[25] E. Abat *et al.* [ATLAS TRT Collaboration], "The ATLAS TRT end-cap detectors", JINST **3**, P10003 (2008).

[26] E. Abat *et al.* [ATLAS TRT Collaboration], "The ATLAS Transition Radiation Tracker (TRT) proportional drift tube: Design and performance", JINST **3**, P02013 (2008).

[27] A.Airapetian *et al.* [ATLAS Collaboration], "ATLAS calorimeter performance Technical Design Report,", CERN-LHCC-96-40.

[28] [ATLAS Collaboration], "ATLAS liquid argon calorimeter: Technical design report", CERN-LHCC-96-41.

[29] [ATLAS Collaboration], "ATLAS tile calorimeter: Technical design report", CERN-LHCC-96-42.

[30] [ATLAS Collaboration], "ATLAS muon spectrometer: Technical design report", CERN-LHCC-97-22, ATLAS-TDR-10.

[31] F. Bauer *et al.*, "Construction and Test of MDT Chambers for the ATLAS Muon Spectrometer", Nucl. Instrum. Meth. A **461**, 17 (2001).

[32] T.Argyropoulos *et al.*, "Cathode strip chambers in ATLAS: Installation, commissioning and in situ performance," IEEE Trans. Nucl. Sci. **56**, 1568 (2009).

[33] G. Aielli *et al.*, "The RPC first level muon trigger in the barrel of the ATLAS experiment,", Nucl. Phys. Proc. Suppl. **158**, 11 (2006).

[34] S. Majewski, G. Charpak, A. Breskin and G. Mikenberg, "A Thin Multiwire Chamber Operating In The High Multiplication Mode", Nucl. Instrum. Meth. **217**, 265 (1983).

[35] F. Pastore [ATLAS Collaboration], "The ATLAS Trigger System: Past, Present and Future,", Nucl. Part. Phys. Proc. **273-275**, 1065 (2016).

[36] A. Borga *et al.*, "Evolution of the ReadOut System of the ATLAS experiment", ATL-DAQ-PROC-2014-012.

[37] [ATLAS Collaboration], "Zero degree calorimeters for ATLAS", CERN-LHCC-2007-01.

[38] P. Jenni *et al.*, "ATLAS Forward Detectors for Measurement of Elastic Scattering and Luminosity", ATLAS-TDR-18, CERN-LHCC-2008-004.

S. Jakobsen, "Commissioning of the Absolute Luminosity For ATLAS detector at the LHC", CERN-THESIS-2013-230.

[39] J. Mitrevski [ATLAS Collaboration], "Electron and Photon Reconstruction with the ATLAS Detector", Nucl. Part. Phys. Proc. **273-275**, 2539 (2016).

[40] S. L. Glashow, "Partial Symmetries of Weak Interactions", Nucl. Phys. **22**, 579 (1961).

S. Weinberg, "A Model of Leptons", Phys. Rev. Lett. **19**, 1264 (1967).

A. Salam and J. C. Ward, "Gauge theory of elementary interactions", Phys. Rev. **136**, 763 (1964).

S. Weinberg, "Non-abelian gauge theories of the strong interactions", Phys. Rev. Lett. **31**, 494 (1973).

[41] S. Weinberg, "A Model of Leptons", Phys. Rev. Lett. **19**, 1264 (1967).

[42] A. Salam, "Weak and Electromagnetic Interactions", Conf. Proc. C **680519**, 367 (1968).

[43] S. L. Glashow, "Partial Symmetries of Weak Interactions", Nucl. Phys. **22**, 579 (1961).

[44] S. Dittmaier *et al.* [LHC Higgs Cross Section Working Group], "Handbook of LHC Higgs Cross-Sections: 1. Inclusive Observables", arXiv:1101.0593 [hep-ph].

[45] M. Tanabashi *et al.* [Particle Data Group], "Review of Particle Physics (RPP)", Phys. Rev. D **98**, 030001 (2018).

[46] G. Aad *et al.* [ATLAS Collaboration], "Observation of a new particle in the search for the Standard Model Higgs boson with the ATLAS detector at the LHC", Phys. Lett. B **716**, 1 (2012).

[47] G. Aad *et al.* [ATLAS Collaboration], "Search for $H \to \gamma\gamma$ produced in association with top quarks and constraints on the Yukawa coupling between the top quark and the Higgs boson using data taken at 7 TeV and 8 TeV with the ATLAS detector", Phys. Lett. B **740**, 222 (2015).

[48] . B. Pontecorvo, "Mesonium and anti-mesonium", Sov. Phys. JETP **6**, 429 (1957).

B. Pontecorvo, "Inverse beta processes and nonconservation of lepton charge", Sov. Phys. JETP **7**, 172 (1958).

[49] Z. Maki, M. Nakagawa and S. Sakata, "Remarks on the unified model of elementary particles", Prog. Theor. Phys. **28**, 870 (1962).

[50] G. Aad *et al.* [ATLAS Collaboration], "Observation of a new particle in the search for the Standard Model Higgs boson with the ATLAS detector at the LHC", Phys. Lett. B **716**, 1 (2012).

[51] S. Dodelson and L. M. Widrow, "Sterile-neutrinos as dark matter," Phys. Rev. Lett. **72**, 17 (1994)

[52] K. M. Case, "Reformulation of the Majorana Theory of the Neutrino," Phys. Rev. **107**, 307 (1957).

[53] "LUCID tags", URL: https://svnweb.cern.ch/trac/atlasoff/browser/ForwardDetectors/LUCID/LUCID_GeoModel/tags/LUCID_GeoModel-00-02-01

[54] "ATLAS Supported Tags", URL: https://atlas-geometry-db.web.cern.ch/atlas-geometry-db/tag_hierarchy_browser.php

[55] S. van der Meer, "Calibration of the Effective Beam Height in the ISR", CERN-ISR-PO-68-31.

[56] C. Rubbia, "Measurement of the Luminosity of p anti-p Collider with a (Generalized) Van Der Meer Method,", CERN-p-anti-p-Note-38.

[57] "Geant4, a toolkit for the simulation of the passage of particles through matter", URL: http: //geant4.web.cern.ch/geant4/.

[58] "Hamamatsu R760 data sheet and Photomultiplier tubes, Basics and applications, Hamamatsu Handbook Edition 3a", URL: https://www.hamamatsu.com/resources/pdf/etd/PMT_handbook_v3aE.pdf

[59] T. Sjostrand *et al.*, "An Introduction to PYTHIA 8.2", Comput. Phys. Commun. **191**, 159 (2015).

[60] G. L. Alberghi *et al.*, “Choice and characterization of photomultipliers for the new ATLAS LUCID detector”, JINST **11**, no. 05, P05014 (2016).

[61] G. Avoni *et al.*, “The new LUCID-2 detector for luminosity measurement and monitoring in ATLAS”, JINST **13**, no. 07, P07017 (2018).

[62] D. S. Smith and S. Bibyk and K. K. Gan and Harris Kagan and R. D. Kass and J. Dopke “Development of the hitbus chip platform for the ATLAS DBM detector at CERN”, IEEE 56th International Midwest Symposium on Circuits and Systems (MWSCAS), P1204 (2013).

[63] L. Adamczyk *et al.*, “AFP: A Proposal to Install Proton Detectors at 220m around ATLAS to Complement the ATLAS High Luminosity Physics Program”, URL: https://atlas-project-lumi-fphys.web.cern.ch/atlas-project-lumi-fphys AFP_TP.pdf

[64] L. Adamczyk *et al.*, “Technical Design Report for the ATLAS Forward Proton Detector”, CERN-LHCC-2015-009, ATLAS-TDR-024.

[65] S. Grinstein, “The ATLAS Forward Proton Detector (AFP)”, Proceedings, 37th International Conference on High Energy Physics (ICHEP 2014): Valencia, Spain, July 2-9, (2014).

[66] T. Bisanz, J. Grobe-Knetter, A. Quadt, J. Rieger, J. Weingarten, “Sub-pixel Mapping and Test Beam Studies with a HV2FEI4v2 CMOS-Sensor-Hybrid Module for the ATLAS Inner Detector Upgrade” JINST **12**, no. 08, P08018 (2017).

[67] C. Royon and N.Cartiglia, "The AFP and CT-PPS projects", Int. J. Mod. Phys. A **29**, no. 28, 1446017 (2014).

[68] V. Berardi *et al.* [TOTEM Collaboration], "TOTEM: Technical design report. Total cross-section, elastic scattering and diffraction dissociation at the Large Hadron Collider at CERN", CERN-LHCC-2004-002, TOTEM-TDR-001.

[69] S. Abdel Khalek *et al.*, "The ALFA Roman Pot Detectors of ATLAS", JINST **11**, no. 11, P11013 (2016).

[70] M. G. Albrow *et al.* [FP420 R and D Collaborations], "The FP420 & Project: Higgs and New Physics with forward protons at the LHC", JINST **4**, T10001 (2009).

[71] S.I. Parker, C.J. Kenney and J. Segal, "3-D: A New architecture for solid state radiation detectors", Nucl. Instrum. Meth. A **395**, 328 (1997).

[72] F. Hartmann, "Evolution of Silicon Sensor Technology in Particle Physics", Springer Tracts Mod. Phys. **275**, pp.1 (2017).

[73] A. Mereghetti [FLUKA Collaboration], "Update on FLUKA calculations of radiation to electronics at Point 1", URL: https://r2e.web.cern.ch/R2E/Presentations/290409_FLUKAupdateP1P5_mereghetti.pdf.25

[74] L. NOZKA *et al.*, "Construction of the optical part of a time-of flight detector prototype for the AFP detector", OPTICS EXPRESS Vol. 24, Issue 24, pp. 27951-27960 (2016).

[75] J. Christiansen, "High Performance Time to Digital Converter", CERN/EP - MIC, Version 2.2 (2004)

[76] P. Y. David *et al.*, "Specification and Validation of the Motion Control System of the ATLAS Forward Proton Roman Pots", ATL-UR-ER-009 (2016).

[77] A. Hald, "A History of Mathematical Statistics from 1750 to1930", New York : Wiley, c (1998).

[78] J. M. Butterworth, J. R. Forshaw and M. H. Seymour, "Multiparton interactions in photoproduction at HERA", Z. Phys. C **72**, 637 (1996).

[79] J. R. Forshaw and D. A. Ross, "Quantum chromodynamics and the pomeron", Cambridge Lect. Notes Phys. **9**, 1 (1997).

[80] J. R.Forshaw, "Diffractive Higgs production: Theory", hep-ph/0508274.

[81] Richard D. Field "Applications of perturbative QCD" Addison-Wesley, The Advanced Book Program (1989).

[82] M. G.Ryskin, R. G. Roberts, A. D. Martin, and E. M.Levin, "Diffractive J/ψ photoproduction as a probe of the gluon density", Zeitschrift für Physik C Particles and Fields, Vol. 76, Issue 2, pp. 231-239 (1997).

[83] L.Frankfurt and M. Strikman, "Color screening and color transparency in hard nuclear processes", Progress in Particle and Nuclear Physics Vol. 27, pp. 135 - 193 (1997).

[84] J. D. Bjorken, "Rapidity gaps and jets as a new physics signature in very high-energy hadron hadron collisions", Phys. Rev. D **47**, 101 (1993).

[85] M. G. Ryskin, A. D. Martin and V. A. Khoze, "Soft processes at the LHC. II. Soft-hard factorization breaking and gap survival,", Eur. Phys. J. C **60**, 265 (2009).

[86] E. Gotsman, E. M. Levin and U. Maor, "Large rapidity gaps in p p collisions", Phys. Lett. B **309**, 199 (1993).

[87] M. Block, R. Fletcher, F. Halzen, B. Margolis and P. Valin, "Theoretical implications of Fermilab Tevatron total and elastic differential-cross-section measurements", Phys. Rev. D **41**, 978 (1993).

[88] E. Gotsman, E. Levin, U. Maor, E. Naftali and A. Prygarin, "Survival probability of large rapidity gaps", hep-ph/0511060.

[89] A. B. Kaidalov, V. A. Khoze, A. D. Martin and M. G. Ryskin, "Probabilities of rapidity gaps in high-energy interactions," Eur. Phys. J. C **21**, 521 (2001).

[90] L. Lonnblad and M. Sjodahl, "Uncertainties on central exclusive scalar luminosities from the unintegrated gluon distributions" JHEP **0505**, 038 (2005).

[91] Michael E. Peskin, and Daniel V. Schroeder, "An Introduction to quantum field theory", Addison-Wesley (1995)

[92] T. Aaltonen *et al.* [CDF Collaboration], "Observation of Exclusive Gamma Gamma Production in $p\bar{p}$ Collisions at $\sqrt{s} = 1.96$ TeV", Phys. Rev. Lett. **108**, 081801 (2012)

K. A. Goulianos [CDF Collaboration], "Aspects of diffraction at the Tevatron: Review and phenomenological interpretation of CDF results on diffraction", AIP Conf. Proc. **698**, 110 (2004)

[93] A. D. Martin, W. J. Stirling, R. S. Thorne and G. Watt, "Parton distributions for the LHC" Eur. Phys. J. C **63**, 189 (2009)

[94] V. A. Khoze, A. D. Martin, M. G. Ryskin and W. J. Stirling, "Diffractive gamma-gamma production at hadron colliders", Eur. Phys. J. C **38**, 475 (2005)

[95] V. A. Khoze, A. D. Martin, M. G. Ryskin and W. J. Stirling, "Double diffractive chi meson production at the hadron colliders", Eur. Phys. J. C **35**, 211 (2004)

[96] T. Aaltonen *et al.* [CDF Collaboration], "Observation of exclusive charmonium production and $\gamma+\gamma$ to $\mu^+\mu^-$ in $p\bar{p}$ collisions at $\sqrt{s} = 1.96$ TeV", Phys. Rev. Lett. **102**, 242001 (2009)

R. Aaij *et al.* [LHCb Collaboration], "Exclusive J/ψ and ψ(2S) production in pp collisions at $\sqrt{s} = 7$ TeV", J. Phys. G **40**, 045001 (2013).

[97] V. A. Khoze, A. D. Martin, and M. G. Ryskin, "Prospects for new physics observations in diffractive processes at the LHC and Tevatron", Eur. Phys. J. C **23**, 311 (2002).

V. A. Khoze, A. D. Martin, and M. G. Ryskin, "Prospects for new physics observations in diffractive processes at the LHC and Tevatron" Eur. Phys. J. C **23**, 311 (2002).

[98] L. A. Harland-Lang, V. A. Khoze, M. G. Ryskin and W. J. Stirling, "Standard candle central exclusive processes at the Tevatron and LHC", Eur. Phys. J. C **69**, 179 (2010).

[99] L. A. Harland-Lang, V. A. Khoze and M. G. Ryskin, "Exclusive physics at the LHC with SuperChic 2", Eur. Phys. J. C **76**, no. 1, 9 (2016).

[100] F. Halzen, and A. D. Martin, "Quarks And Leptons: An Introductory Course In Modern Particle Physics", New York, Usa: Wiley (1984).

[101] R. K. Ellis, W. J. Stirling, and B. R.Webber, "QCD and Collider Physics", Cambridge University Press (1996).

[102] J. C. Collins, "Sudakov form-factors," Adv. Ser. Direct. High Energy Phys. **5**, 573 (1989)

[103] , L. Adamczyk *et al.*, "Technical Design Report for the ATLAS Forward Proton Detector" CERN-LHCC-2015-009, ATLAS-TDR-024.

[104] A. B. Kaidalov, V. A. Khoze, A. D. Martin and M. G. Ryskin, "Central exclusive diffractive production as a spin-parity analyser: From Hadrons to Higgs", Eur. Phys. J. C **31**, 387 (2003).

[105] V. A. Khoze, A. D. Martin and M. G. Ryskin, "Higgs or dijet production in double rapidity gap events,", hep-ph/0006005.

[106] V. A. Khoze, A. D. Martin and M. G. Ryskin, "Double diffractive processes in high resolution missing mass experiments at the Tevatron", Eur. Phys. J. C **19**, 477 (2001).

[107] E. Papageorgiu, “An Intermediate mass Higgs boson in two photon coherent processes at the LHC”, Phys. Lett. B **352**, 394 (1995).

[108] D. d’Enterria and J. P. Lansberg, “Study of Higgs boson production and its b anti-b decay in gamma-gamma processes in proton-nucleus collisions at the LHC”, Phys. Rev. D **81**, 014004 (2010).

[109] C. F. von Weizsacker, “Radiation emitted in collisions of very fast electrons”, Z. Phys. **88**, 612 (1934).

[110] E. J. Williams, “Correlation of certain collision problems with radiation theory”, Kong. Dan. Vid. Sel. Mat. Fys. Med. **13N4**, no. 4, 1 (1935).

[111] E. Fermi, “Über die Theorie des Stoßes zwischen Atomen und elektrisch geladenen Teilchen”, Zeitschrift für Physik **29**, no. 1, 315 (1924).

[112] F. Wilczek, “Decays of Heavy Vector Mesons Into Higgs Particles”, Phys. Rev. Lett. **39**, 1304 (1977).

J. R. Ellis, M. K. Gaillard, D. V. Nanopoulos and C. T. Sachrajda, “Is the Mass of the Higgs Boson About 10-GeV?”, Phys. Lett. **83B**, 339 (1979).

H. M. Georgi, S. L. Glashow, M. E. Machacek and D. V. Nanopoulos, “Higgs Bosons from Two Gluon Annihilation in Proton Proton Collisions”, Phys. Rev. Lett. **40**, 692 (1978).

T. G. Rizzo, “Gluon final states in Higgs-boson decay”, Phys. Rev. D **22**, 178 (1980).

[113] A. G. Shuvaev, K. J. Golec-Biernat, A. D. Martin and M. G. Ryskin, "Off diagonal distributions fixed by diagonal partons at small x and xi", Phys. Rev. D **60**, 014015 (1999).

[114] V. A. Khoze, A. D. Martin and M. G. Ryskin, "Can the Higgs be seen in rapidity gap events at the Tevatron or the LHC?", Eur. Phys. J. C **14**, 525 (2000).

[115] G. Altarelli and G. Parisi, "Asymptotic Freedom in Parton Language", Nucl. Phys. B **126**, 298 (1977).

[116] D. V. Shirkov and I. L. Solovtsov, "Analytic QCD running coupling with finite IR behavior and universal alpha-s (0) value", hep-ph/9604363.

[117] C. Wetterich, "Exact evolution equation for the effective potential", Phys. Lett. B **301**, 90 (1993).

T. R. Morris, "The Exact renormalization group and approximate solutions", Int. J. Mod. Phys. A **9**, 2411 (1994).

[118] M. L. Good and W. D. Walker, "Diffraction disssociation of beam particles" Phys. Rev. **120**, 1857 (1960).

[119] A. Shuvaev, "Solution of the off forward leading logarithmic evolution equation based on the Gegenbauer moments inversion", Phys. Rev. D **60**, 116005 (1999).

[120] R. E. Cutkosky, "Singularities and discontinuities of Feynman amplitudes", J. Math. Phys. **1**, 429 (1960).

[121] V. A. Khoze, A. D. Martin and M. G. Ryskin, "New Physics with Tagged Forward Protons at the LHC," Frascati Phys. Ser. **44**, 147 (2007)

[122] A.D. Martina, W.J. Stirlingb, R.S. Thornec, and G. Watta, "Uncertainties on α_S in global PDF analyses and implications for predicted hadronic cross-sections", Eur. Phys. J. C **64**, no. 4, 653 (2009).

[123] R. G. Roberts, "The Structure of the Proton: Deep Inelastic Scattering", Cambridge University Press, Cambridge, UK, (1990).

[124] A. D. Martin, R. G. Roberts, W. J. Stirling and R. S. Thorne, "MRST2001: Partons and α_s from precise deep inelastic scattering and Tevatron jet data", Eur. Phys. J. C **23**, 73 (2002).

[125] A. D. Martin, A. J. T. M. Mathijssen, W. J. Stirling, R. S. Thorne, B. J. A. Watt and G. Watt, "Extended Parameterisations for MSTW PDFs and their effect on Lepton Charge Asymmetry from W Decays", Eur. Phys. J. C **73**, no. 2, 2318 (2013).

[126] A. D. Martin, W. J. Stirling, R. S. Thorne and G. Watt, "Parton distributions for the LHC", Eur. Phys. J. C **63** 189 (2009).

[127] A. Buckley, J. Ferrando, S. Lloyd, K. Nordstrm, B. Page, M. Rufenacht, M. Schonherr and G. Watt, "LHAPDF6: parton density access in the LHC precision era", Eur. Phys. J. C **75**, 132 (2015).

[128] "LHAPDF Documentation", URL: http://lhapdf.hepforge.org

[129] A. Deur, S. J. Brodsky and G. F. de Teramond, "The QCD Running Coupling", Prog. Part. Nucl. Phys. **90**, 1 (2016).

[130] D. V. Shirkov and I. L. Solovtsov, "Analytic QCD running coupling with finite IR behavior and universal alpha-s (0) value", hep-ph/9604363.

[131] G. P. Lepage, "A new algorithm for adaptive multidimensional integration" Journal of Computational Physics **27**, 192 (1978).

[132] M. B. Gay Ducati and G. G. Silveira, "Diffractive Higgs boson photoproduction in Ultraperipheral Collisions at LHC," Phys. Rev. D **82**, 073004 (2010)

[133] L. A. Harland-Lang, V. A. Khoze, M. G. Ryskin and W. J. Stirling, "Central exclusive production within the Durham model: a review," Int. J. Mod. Phys. A **29**, 1430031 (2014)

Appendices

Appendix A

QCD and QED Feynman Rules

$$
\text{incoming}\left\{
\begin{array}{ll}
\text{fermion:} & U(p) \\[2ex]
\text{anti fermion:} & \bar{V}(p) \\[2ex]
\text{photon:} & \epsilon_\mu \\[2ex]
\end{array}
\right.
$$

$$
\text{ougoing}\left\{
\begin{array}{ll}
\text{fermion:} & \bar{U}(p) \\[2ex]
\text{anti fermion:} & V(p) \\[2ex]
\text{photon:} & \epsilon^*_\mu
\end{array}
\right.
$$

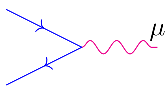

$= -ie_f\gamma_\mu$ fermion-photon vertex

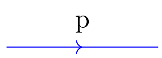

$= i\frac{\not{p}+m}{p^2-m^2+i\epsilon}$ fermion propagator

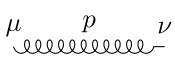

$= -i\frac{g_{\mu\nu}}{p^2+i\epsilon}$ gluon propagator

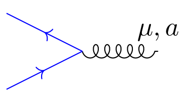

$= -ie_q\gamma_\mu t^a$ quark-gluon vertex

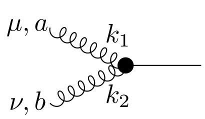

$= V^{ab}_{\mu\nu} = \delta^{ab}F(\frac{M_H^2}{m_t^2})\frac{M_H^2\alpha_s}{4\pi v}\big(g_{\mu\nu} - \frac{k_{1\mu}k_{2\nu}}{k_1.k_2}\big)$ gluon fusion vertex

Appendix B

Eikonal Function

When two partons collide at some impact parameter, b, then the average number of secondary hard scatterings (the average number of jet pairs produced in the proton-proton interaction) is given by:

$$< n(b,s) >= L(s)\sigma(s,b) \tag{2.1}$$

where $L(s)$ is the parton luminosity and $\sigma(s,b)$ is the cross-section for a pair of partons to produce a pair of jets. If one assumes that rescatterings are independent of each other, the distribution of the number of rescatterings at an impact parameter b can be modelled by the Poisson statistics. Within this simple model, the gap survival probability is directly related to the mean number of rescatterings at an impact parameter b.

$$P_h(b,s) = \frac{< n(b,s) >^h}{h!} e^{n(b,s)} \tag{2.2}$$

where $< n(b,s) >$ is the average number of secondary hard scatterings . Therefore, the total cross-section then can be written as:

$$
\begin{aligned}
\sigma_{tot} &= 2\pi \int (\sum_{h=1}^{\infty} P_h(b,s)) d^2 b_t \\
&= 2\pi \int (1 - e^{<n(b,s)>}) d^2 b_t
\end{aligned}
\tag{2.3}
$$

In order to express the total cross-section, one can use optical theorem which relates total cross and imaginary part of the elastic cross-section $a(b, s)$ in impact parameter space b through the unitarity relation as the following equation:

$$
\sigma_{tot} = 4\pi \int Im(a(s,b) d^2 b_t \tag{2.4}
$$

And then the elastic and inelastic part of the cross-section can be expressed as:

$$
\begin{aligned}
\sigma_{el} &= 4\pi \int a(s,b)^2 d^2 b_t \\
\sigma_{inel} &= \sigma_{tot} - \sigma_{el}
\end{aligned}
\tag{2.5}
$$

After comparing the total cross-section in equation 2.3 and 2.5, we can express the elastic amplitude in terms of $< n(b,s) >$ or equivalently the Eikonal function [83], $\Omega(b,s)$, as:

$$
a(s,b) = \frac{e^{<n(b,s)>} - 1}{2i} = \frac{e^{-\Omega(b,s)} - 1}{2i} \tag{2.6}
$$

Therefore, the total elastic and inelastic cross-sections can be express in the following format as functions of Eikonal function:

$$\begin{aligned}\sigma_{tot} &= 2\pi \int (1 - e^{-\Omega(b,s)}) d^2b \\ \sigma_{inel} &= \pi \int (1 - e^{-2\Omega(b,s)}) d^2b \\ \sigma_{el} &= \pi \int (1 - e^{-\Omega(b,s)})^2 d^2b\end{aligned} \tag{2.7}$$

Appendix C

Optical Theorem

The Optical theorem can be deduced from the unitarity of the scattering matrix (S)[34].

$$SS^\dagger = 1 \tag{3.1}$$

where $S = 1 + iT$. The transfer matrix T [35] is not Hermitian. Therefore, the unitarity of S matrix implies

$$\begin{aligned} &1 = SS^\dagger = (1 + iT)(1 - iT^\dagger) = 1 + TT^\dagger - i(T - T^\dagger) \\ &i(T - T^\dagger) = TT^\dagger \end{aligned} \tag{3.2}$$

The left hand side of the above equation is:

$$< f|i(T - T^\dagger)|i >= i(2\pi)^4\delta^4(p_i - p_f)[M^\dagger(i \to f) - M(f \to i)] \tag{3.3}$$

[34] S matrix describes the relation between the outgoing waves to the incoming waves.

[35] Transfer matrix T expresses the coefficients of the wave function on the right hand side of the sample in terms of the coefficients of the wave function on the left hand side.

where M^2 is the amplitude, p_i and p_f are the initial and final momenta, and $|i>$ and $|f>$ are the initial and final states of the scattering process.

Summing over all intermediate states, the right hand side of equation 3.3 is:

$$< f|TT^{\dagger}|i> = \sum_m d\Pi_m < f|T|m >< m|T^{\dagger}|i >$$
$$= \sum_m [(2\pi)^4 \delta^4(p_m - p_f)][(2\pi)^4 \delta^4(p_i - p_m)] \int d\Pi_m M^{\dagger}(f \to m) M(m \to i) \tag{3.4}$$

Therefore, after applying simple algebra the optical theorem is given by the following equation:

$$i[M^{\dagger}(i \to f) - M(f \to i)] = \sum_m \int d\Pi_m M^{\dagger}(f \to m) M(m \to i) \tag{3.5}$$

where $d\Pi_m$ is the phase space factor

Appendix D

Three Body Phase Space

Three body phase space is the differential phase space of the intermediate propagators which follows the general formula of phase space and can be expressed as:

$$\int d\Pi_3 = \int \frac{d^4 l_1}{(2\pi)^3} \frac{d^4 l_2}{(2\pi)^3} \frac{d^4 l_2}{(2\pi)^3} \delta(l_1^2 - m_q^2)\delta(l_2^2 - m_q^2)\delta(l_3^2)(2\pi)^4\delta^4(P + q - l_1 - l_2 - l_3) \tag{4.1}$$

Where l_1^μ, l_2^μ and l_3^μ are the four momentum of the quarks which By applying conservation of energy in the vertices we can subtitled l_1 and l_2 by $q - l$ and $l - k$ and using Sudakov parametrization and characteristic of delta function, the phase space equation will be simplified to:

$$
\begin{aligned}
\int d\Pi_3 &= \frac{1}{2\pi^5}\int d^4l d^4k \delta([q-l]^2 - m_q^2)\delta([l-k]^2 - m_q^2)\delta([P-k]^2) \\
&= \frac{1}{2\pi^5}\frac{W^4}{4}\int d\alpha_l d\beta_l d^2\bar{l} d\alpha_k d\beta_k d^2\bar{k} \frac{1}{W^2(1-\alpha_l)}\delta\big(\beta_l + x - \frac{\bar{l}^2 + m_q^2}{W^2(1-\alpha_l)}\big) \\
&\frac{1}{W^2(\alpha_l-\alpha_k)}\delta\big(\beta_l - \beta_k - \frac{[l \bar{-} k]^2 + m_q^2}{W^2(\alpha_l-\alpha_k)}\big)\frac{1}{W^2(|\alpha_k|)}\delta\big((1-\beta_k) + \frac{\bar{k}^2}{W^2\alpha_k}\big) \\
&= \int d\Pi_3 = \frac{1}{2\pi^5}\frac{1}{4W^2}\int d\alpha_l d^2\bar{k} d^2\bar{l}\frac{1}{\alpha_l(1-\alpha_l)}
\end{aligned}
\tag{4.2}
$$

here Sudakov factors are described as follows:

$$
k = \alpha_k p_2 + \beta_k p_1 + k_\perp, l = \alpha_l p_2 + \beta_l p_1 + l_\perp, q = p_2 - x p_1 \tag{4.3}
$$

To make sure that the quark propagator are on-shell particles the following equation should be true

$$
\begin{aligned}
\beta_k &= 1 + \frac{\bar{k}^2}{W^2\alpha_k} \\
\beta_l - \beta_k &= \frac{[l \bar{-} k]^2 + m_q^2}{W^2(\alpha_l - \alpha_k)} \\
\beta_l &= -x + \frac{\bar{l}^2 + m_q^2}{W^2(1-\alpha_l)}
\end{aligned}
\tag{4.4}
$$

Appendix E

Amplitude of The CEDP Process

In this appendix we compute the amplitude of left and right side of the CEDP process in the parton level, required for computing the cross-section. Figure 6.1, shows the Feynman diagrams for the process.

By utilizing QED and QCD Feynman rules that mentioned in the previous chapter, the amplitude of the left and right side of the CEDP process could be expressed as below:

$$\mathcal{M}_1\mathcal{M}_2 = \sum \epsilon_\alpha \epsilon^*_\beta \sum \bar{u}(l)(-ig_s\gamma^\mu t^B)u(p)\big(\frac{-ig_{\sigma}\mu}{k^2}\big)(-ig_s\gamma^\sigma t^C)A^{\alpha\beta\sigma\lambda}\big(\frac{-i\delta^{AD}g_{\lambda_1\lambda}}{k^2}\big)$$
$$(-ig_s\gamma^\lambda t^A)V^{ab}_{\lambda_1\lambda_2}\big(\frac{-i\delta^{DB}g_{\lambda_2\nu}}{r^2}\big)\sum \bar{u}(p')(-ig_s\gamma^\nu t^B)\bar{u}(l) \tag{5.1}$$

Where $A^{\alpha\beta\sigma\lambda}$ is the amplitude of the quark loop shown in figure 5.1and $V^{ab}_{\lambda_1\lambda_2}$ is the well-known gluon fusion vertex in the Standard Model. $\sum \epsilon_\alpha \epsilon^*_\beta$ is the sum of all the polarization of the incoming and outgoing photons. $u(x)$ and $\bar{u}(x)$ are respectively corresponding to the incoming and outgoing quarks. Term that include g_s correspond to gluon vertices and the rest are representing gluon propagators.

Because the momentum of gluon is sufficiently small compare to the incoming protons, we can use Eikeonal approximation, $\bar{u}(p+q)\gamma^\mu u(p) \simeq 2p^\mu$ in this calculation. Therefor, the above equation can be simplified to :

$$\mathcal{M}_1\mathcal{M}_2 = \frac{N_c^2-1}{4N_c^2}\frac{1}{r^2k^4}p_\sigma p^\nu V^{ab}_{\lambda\nu}\sum \epsilon_\alpha\epsilon^*_\beta A^{\alpha\beta\sigma\lambda} \tag{5.2}$$

By substituting the well-known gluon fusion vertex in the Standard Model [112] $V^{ab}_{\lambda\nu} = \frac{2}{3}\frac{M_H^2\alpha_s}{4\pi v}\left(g_{\lambda\nu} - \frac{r_\mu k_\lambda}{r.k}\right)$ into the above equation, it will be simplified to:

$$\mathcal{M}_1\mathcal{M}_2 = \frac{N_c^2-1}{4N_c^2}\frac{M_H^2\alpha_s}{6\pi v}\frac{1}{r^2k^4}p_\sigma p_\lambda\sum \epsilon_\alpha\epsilon^*_\beta A^{\alpha\beta\sigma\lambda} \tag{5.3}$$

Also, due to the fact that the gluons only have transverse component ($k^2 \approx -k_\perp^2 = k_T^2$), the second term in $V_{\mu\lambda}$ vanishes upon contraction with p_1^λ, yielding $V_{\mu\lambda}p_1^\lambda = \frac{2}{3}\frac{M_H^2\alpha_s}{4\pi v}p_1^\mu$.

Figure 5.1, shows two of the four diagrams which are needed to compute the virtual photon impact factor $A^{\alpha\beta\sigma\lambda}$(the other two are obtained by reversing the direction of the quark line). To obtain $\sum\epsilon_\alpha\epsilon^*_\beta A^{\alpha\beta\sigma\lambda}$ we start with the

Feynman rules to compute the amplitude as follows:

$$\sum \epsilon_\alpha \epsilon_\beta^* A^{\alpha\beta\sigma\lambda} = -(4\pi)^2 \alpha\alpha_s \sum_q e_q^2 \sum \epsilon_\alpha \epsilon_\beta^* \Big(\frac{Tr(\Gamma_1^{\alpha\beta\sigma\lambda})}{(l^2 - m_q^2)^2} - \frac{Tr(\Gamma_2^{\alpha\beta\sigma\lambda})}{(l^2 - mq^2)((q-l-k)^2 - mq^2)} \Big)$$
$$\Gamma_1^{\alpha\beta\sigma\lambda} = [\gamma^\alpha(\not{l} + m_q)\gamma^\lambda(\not{l} + \not{k})\gamma^\sigma(\not{l} + m_q)\gamma^\beta(\not{q} - \not{l})]$$
$$\Gamma_2^{\alpha\beta\sigma\lambda} = [\gamma^\alpha(\not{l} + m_q)\gamma^\lambda(\not{l} + \not{k})\gamma^\beta(\not{q} - \not{l} - \not{k} + m_q)\gamma^\sigma(\not{q} - \not{l})] \tag{5.4}$$

Therefore, the multiplication of the left and right side of the amplitude can be expressed as:

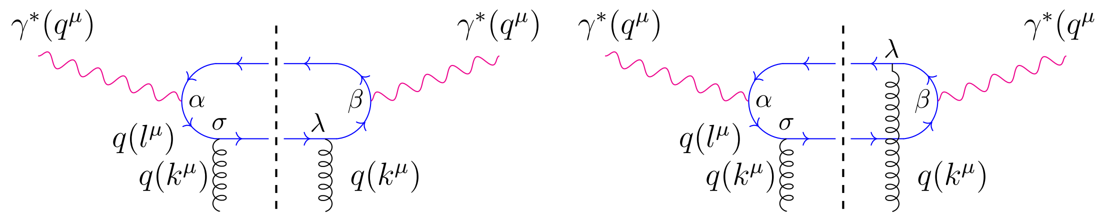

Figure 5.1: We make use of the Cutkosky cutting rules to calculate the imaginary part of the amplitude. The dotted line indicates the cut which separated the left and right side of the process. By applying the optical theorem, the imaginary part of the amplitude is the convolution of the amplitude of the right process and the left process in a three body phase space.

$$\mathcal{M}_1\mathcal{M}_2 = A\frac{1}{r^2k^4}\Big(\frac{Tr(\Xi_1)}{(l^2 - m_q^2)^2} - \frac{Tr(\Xi_2)}{(l^2 - mq^2)((q-l-k)^2 - mq^2)}\Big)$$
$$A = -\frac{\alpha\alpha_s^2}{4\pi^2}\frac{M_H^2\alpha_s}{6\pi v}\sum_q e_q^2 \frac{N_c^2 - 1}{4N_c^2} \tag{5.5}$$
$$\Xi_1 = \Sigma\epsilon_\nu\epsilon_\sigma^*[\gamma^\nu(\not{l} + m_q)\not{p}(\not{l} + \not{k})\not{p}(\not{l} + m_q)\gamma^\sigma(\not{q} - \not{l})]$$
$$\Xi_2 = \Sigma\epsilon_\nu\epsilon_\sigma^*[\gamma^\nu(\not{l} + m_q)\not{p}(\not{l} + \not{k})\gamma^\sigma(\not{q} - \not{l} - \not{k} + m_q)\not{p}(\not{q} - \not{l})]$$

where

$$
\begin{aligned}
\Sigma\epsilon_\nu\epsilon^*_\sigma &= -g_{\nu\sigma} + 4\frac{Q^2}{W^4}p_\nu p_\sigma \\
\Xi_1 &= g_{\nu\sigma}\Gamma_1^{\nu\sigma} + 4\frac{Q^2}{W^4}p_\nu p_\sigma \Gamma_1 \\
\Xi_2 &= g_{\nu\sigma}\Gamma_2^{\nu\sigma} + 4\frac{Q^2}{W^4}p_\nu p_\sigma \Gamma_2
\end{aligned}
\tag{5.6}
$$

Appendix F

MATLAB Computational Results

We computed Γ_1, $\Gamma_1^{\nu\sigma}$, Γ_2, $\Gamma_2^{\nu\sigma}$, using MATLAB program. The result shows in the following equations:

$$
\begin{aligned}
g_{\nu\sigma}\Gamma_1^{\nu\sigma} &= -4\alpha_l s^2[\frac{-D_1 - m_q^2 + (1-\alpha_l)^2 m_q^2 - \alpha_l(1-\alpha_l)Q^2}{1-\alpha_l}] \\
\Gamma_1 &= -2\alpha_l^3(\alpha_l - 1)s^4 \\
g_{\nu\sigma}\Gamma_2^{\nu\sigma} &= -4s^2[\frac{1}{2}(D_1 + D_2) + \alpha - l(1-\alpha_l)Q^2 + (\alpha_l(1-\alpha_l) - \frac{1}{2})k_\perp + (-\alpha_l(1-\alpha_l) + 1)m_q^2] \\
\Gamma_2 &= 2\alpha_l^2(\alpha_l - 1)^2 s^4
\end{aligned}
\tag{6.1}
$$

where

$$
\begin{aligned}
D_1 &= -\alpha_l(1-\alpha_l)Q^2 - l_\perp^2 - m_q^2 \\
D_2 &= -\alpha_l(1-\alpha_l)Q^2 - (l+k)_\perp^2 - m_q^2
\end{aligned}
\tag{6.2}
$$

Therefore, the amplitude is given by:

$$\begin{aligned}
\mathcal{M} =&\frac{4}{3\pi^2}\frac{C_F^2}{N_c^2-1}\frac{\alpha W^2 M_H^2}{v}\int d^2\bar{k}\int_0^1 d\alpha_l\int_0^1 d\tau\alpha_s^3(\bar{k}^2)\sum_q(F_1+F_2)\\
F_1 =& \frac{e_q^2}{\bar{k}^4}\frac{[\alpha_l^2+(1-\alpha_l)^2][\tau^2+(1-\tau^2)]}{\alpha_l(1-\alpha_l)Q^2+\tau(1-\tau)\bar{k}^2+m_q^2}\\
F_2 =& \frac{e_q^2 m_q^2}{\bar{k}^6(\alpha_l(1-\alpha_l)Q^2+\tau(1-\tau)\bar{k}^2+m_q^2)}\big(4(1-\alpha_1+\alpha_l^2)+\frac{2e_q^2\bar{k}^2\tau(1-\tau)(6\alpha_l^2-6\alpha_l+1)}{\alpha_l(1-\alpha_l)Q^2+m_q^2}\big)
\end{aligned}\tag{6.3}$$

Appendix G

“Photoproduction” package

The “Photoproduction” directory consists of two sub-directories: Main, and Plot. The Main subdirectory includes all the files needed to compute the cross-section and Plot subdirectory consists of the programs needed to plot the PDF vs x and Q^2, α_s and Cross-section vs mass of the Higgs boson.

Main directory

The Main directory includes nine other sub-dirctories listed as follows: Common, obj, Main, Integrand, Sudakov, LHAPDF, PDF , Alpha and bin.

Common:

Includes all the General variables that have been used through out the program.

obj:

Includes the object files produced by the compiler from the Fortran files.

Main:

The Fortran source files in various subdirectories.

Integrand:

Include the integrand for the VEGAS file.

Sudakov:

Includes all the files that take to determine sudakov factor at the given x and Q^2.

1-Sudakov: calculates Sudakov factor using equation 6.12.

2-initsud: writes out Sudakov factor in a grid of x and Q^2 to “sud.dat” file located in bin subdirectory.

3-calcsud: read Sudakov form factor from “sud.dat”.

4-sudint: interpolator for Sudakov form factor to calculate xg for a given x and Q^2.

5-sPDF: calculates exclusive skewed pdf $\frac{d}{dlnQ^2}(Txg)$ where T is Sudakov form factor and $xg =$ is skewed pdf.

LHAPDF:

LHAPDF is a general purpose C++ interpolator, used for evaluating PDFs from discretized data files.

PDF:

Includes all the files that take the conventional PDFs from MSTW08NLO PDF set and calculate the General PDFs and finally interpolate the GPDs with Sudakov form factor. Files from 1 to 5 get the xg (gluon PDF) from the grid files in LHAPDF and calculate skewed pdf and save it in the file called 'hg.dat' in 4 columns related to Q^2, lnx, tg (skewed pdf), dtg (integrated skewed pdf) respectively.

1-inpdf: call LHAPDF and the PDFset , LHAPDF function.

2-PDFlha: after 'inpdf' calls LHAPDF, it evaluates the value of gluon PDF for PDFINPUT , LHAPDF function.

3-PDF: use the PDFINPUT to calculate single PDF xg and $\frac{dxg}{dQ^2}$.

4-hg: Calculates skewed unintegrated PDF.

5-inithg: writes out skewed PDF to "hg.dat".

6-calchg: read in skewed pdf from "hg.dat".

7-hpdfint: interpolator for skewed pdf.

Alpha:

Only include one file that extract the α_s from MSTW08NLO PDF set.

alpha.f: calculate strong coupling constant, α_s used by the current PDF, using the following formula

$$\alpha_{an}^{(2,approx.)}(k^2) = \frac{4\pi}{b_0(N_f=3)}\Big(\frac{1}{l(ln\frac{k^2}{\Lambda_{21}^2}, c_{21}^{fit})} + \frac{1}{1-exp(l(ln\frac{k^2}{\Lambda_{21}^2}, c_{21}^{fit}))}\Big) \quad (7.1)$$

$$l(L_Q, c) = L_Q + c\ ln\sqrt{L_Q^2 + 4\pi^2} \quad (7.2)$$

$$b_0 = \frac{11}{3} - \frac{2}{3}N_f \quad (7.3)$$

bin:

It includes the executable files: superchic and init. Also the input data file. The PDF set MSTW08NLO is also in this directory.

1-init and intg: Includes the two executable folders.

2-inputs: input.DAT file includes all the initial condition For energy, quantum numbers and etc.

3-PDFsets :Consists of the PDF set that we are using in this calculation. Here we are using MSTW08NLO, which returns the momentum density (that is x times the number density). The values of α_S obtained from the fits are stored in the grid files. For consistency, the same values should be used in all calculations involving the PDFs.

Plotting and controlling

Plot:

Includes file to choose different sets of α_s and to plot α_s, $PDFs$ and the changes of cross-section with respect to higgs mass M_H.

1-ir.dat: It contains various analytic couplings to compare different α_s in the infrared regime.(see https://.arxiv.org/pdf/hep-ph/0405062.pdf for details).

2-alpha.p: make α_s plot.

3-IntPlot: contains Main.f and Integrand.f set up for plotting the integrand.

4-MassPlot: contains Main.f for plotting how the cross-section changes with the higgs mass